POLITECNICO DI MILANO

Scuola di Ingegneria Industriale e dell'Informazione

Corso di Laurea Magistrale in Ingegneria Aeronautica

Numerical parametric analysis and experimental investigation of MFC-actuated trailing edges

Relatore: Prof. Franco AUTERI
Correlatore: Prof. Paolo BETTINI

Tesi di laurea di:
Nicholas Fabio BONFANTI
Matr. 836468

Anno Accademico 2016 - 2017

Abstract

This study describes the steady effects on the lift and moment coefficients of a plate mounted on the airfoil trailing edge and actuated with MFC piezoelectric devices. The problem is analysed with both numerical calculations and experiments. The structural model is developed with both linear and nonlinear 2D beam models; the nonlinearities take into account large beam rotations. A finite-difference scheme is developed for the linear beam model, and a shooting scheme for the nonlinear one. XFoil is employed to solve the aerodynamic problem for its fast computation times, accuracy, and widespread use. The definition of the lift coefficient derivative with respect to the actuation force allows us to describe the actuation efficacy by means of a scalar value. The behaviour of this scalar value as function of both structural and aerodynamic parameters is modelled with approximate, closed form scaling laws when possible. A rather simple but accurate scaling law can be envisaged for the inviscid, uncoupled results. The viscous ones can be described as functions of the boundary layer properties over the actuation system. The coupled formulation suggests that the aeroelastic coupling decreases the actuation efficacy and its effect can be modelled as a power law of both flight velocity and actuator length. The parameter space analysis is followed by two simplified real case applications, in order to give a quantitative insight of the actuation system potentialities to the reader. The construction of three actuation systems with composite materials is described, highlighting the chosen lamination process. The three actuation systems are tested in a wind tunnel, and the results are compared with the numerical simulations.

Keywords: Morphing wing, Deformable trailing edge, Piezo-actuation, Micro Fiber Composites.

Sommario

Questo studio descrive gli effetti stazionari sul coefficiente di portanza e momento di una piastra montata sul bordo di uscita di profili alari, attuata con MFC. Il problema è analizzato sia tramite simulazioni numeriche che esperimenti. Il modello strutturale è sviluppato tramite modelli lineari e non lineari di travi 2D; la non linearità tiene in conto le grandi rotazioni. È sviluppato un metodo alle differenze finite per la trave lineare, e un metodo di shooting per quella non lineare. XFoil viene utilizzato come solutore aerodinamico per i brevi tempi di calcolo, l'accuratezza, e l'ampio utilizzo. La definizione della derivata del coefficiente di portanza rispetto alla forza di attuazione permette di descrivere l'efficacia dell'attuazione con un valore scalare. Il comportamento di questo scalare al variare dei parametri strutturali ed aerodinamici è modellato con leggi di scalatura approssimate e in forma chiusa quando possibile. Il modello inviscido a spostamento imposto mostra una descrizione come legge di scalatura abbastanza semplice ma accurata. Il modello viscoso può essere descritto come funzione delle proprietà dello strato limite sull'attuatore. La formulazione aeroelastica suggerisce che l'accoppiamento aeroelastico diminuisca l'efficacia dell'attuazione, e possa esser modellato con una legge di potenza, rispetto sia alla velocità di volo che alla lunghezza del sistema di attuazione. L'analisi dello spazio dei parametri è seguita da due applicazioni semplificate a casi reali, allo scopo di dare al lettore una caratterizzazione quantitativa delle potenzialità del sistema di attuazione. Viene successivamente descritta la produzione di tre sistemi di attuazione con materiali compositi, sottolineando i processi di laminazione adottati. I tre sistemi di attuazione sono successivamente testati in una galleria del vento, e i risultati sperimentali sono paragonati a simulazioni numeriche.

Keywords: Ala deformabile, Bordi di uscita deformabili, Piezo-attuazione, Micro Fiber Composites.

This is for you, ______________.

I would like to thank Prof. F. Auteri for his constant support, dedication, and patience in the production of this work, and Prof. P. Bettini for his valuable help, especially in this first approach of mine in the experimentation world.

I owe a lot to my family for supporting me during my studies, from my first grade to this master's thesis.

A special thanks to everyone who helped me in the laboratories, I wish I had more experience to help you back.

I owe a lot to my friends and colleagues too, for bearing with me for all this years.

Finally, a last thanks to whoever is reading this: I hope this work will result worthy of your time.

This project has received funding from the European Union's H2020 program for research, technological development and demonstration under grant agreement no 723402.

Contents

List of Figures

List of Tables

Chapter one

Introduction

1.1 Shape morphing overview

In the incessant search for optimal aerodynamic shapes that has driven the aerospace research since its early beginnings, the advent of shape morphing technologies is one of the latest innovations. Here, in agreement with the general opinion, the word *morphing* will refer to continuous geometry modifications and not traditional discrete ones, e.g. flaps, despite they are still technically *morphing* the wing.
Despite having attracted the interest of hundreds of research groups over the past decades, most of the research stopped at a design or prototype stage, with strong limitations on both small scale (MAVs and drones) and full scale vehicles; this left the field with plenty of open questions and issues [34].

Literature examples of continuous deflection of aerodynamic surfaces can be meaningfully and conveniently categorized. One way is by type of actuation:

1. *hydraulic actuators*, having the highest specific work output ($\sim 35\,000\,\mathrm{J\,kg^{-1}}$), but with the big disadvantage of operating with heavy fluids at very high pressure; they require in fact particular care in the tubing. A reasonable maximum strain for this kind of actuation is $\varepsilon = 1$, or $\varepsilon \sim 3 \div 4$ assuming a telescopic system; the maximum stress is limited by the fluid pressure and may vary largely in different applications. Lengths under $\sim 10\,\mathrm{cm}$ and deployment speeds over $\sim 0.5\,\mathrm{m\,s^{-1}}$ may result unpractical because of both the complexity of miniaturizing heavy duty mechanisms and the problems arising in seal design [17],

2. *pneumatic actuators*, in particular pneumatic artificial muscles (PAMs), characterized by a high specific work output ($\sim 4000\,\mathrm{J\,kg^{-1}}$). They are naturally compliant and therefore tolerant to misalignments. Since they use air as working fluid, there is no need for a return circuit. Their functioning is rather simple: inflating an elastomeric bladder with air forces an external helically braided sleeve to extend radially. Since the sleeve fibers are very stiff they generate a contraction on the longitudinal direction, along with an actuation force [37]. Non-PAM pneumatic actuation systems are similar to the hydraulic ones but with smaller maximum stresses,

3. *electric actuators*, [22]. Literature shows a limited use of these actuators for wing shape morphing, probably because of their weight, which comprises also the weight of lead and screw mechanisms. With exception of linear motors, almost all electric motors can be considered to have infinite dis-

placement since they use a rotor-stator system. This advantage is not so significant in morphing, since very large displacements are often not required,

4. *piezoelectric actuators*, in particular macro fiber composites (MFCs). Despite the low specific work ($\sim 5\,\mathrm{J\,kg^{-1}}$ [21]) they are widely used for adaptive flexible wing mechanisms; their rather high frequency response, up to 10 times superior to a servo flap with comparable rotation [24], could be a significant advantage compared to other actuation systems. However, particular care should be taken using many MFCs in parallel: the large capacitance obtained could introduce a lag in the input-output, resulting in degradation of both frequency response and dynamic stability [5]. MFC effects can be easily modelled in FEA software as thermal stresses, since they have similar governing equations. Piezoelectric stack actuators also fall in this category; they are characterized by higher loads (up to 10kN), similar strains, and a completely different shape compared to MFCs [12], being in fact cylinders with a typical size going from $\sim 1\,\mathrm{mm}$ to $\sim 2\,\mathrm{cm}$,

5. *shape-memory-alloy actuators*, or SMA. This particular actuation uses the capability of some metallic alloys to return to a defined shape when heated due to a change in their crystalline structure. This allows their use as actuators, with a typical specific work of $\sim 4500\,\mathrm{J\,kg^{-1}}$ [37]. Despite the complex behaviour under cyclic conditions [4], they can be effectively used for a quite wide range of deformations, from wing twisting [16] to trailing edge control [36] and camber morphing [31]. A return mechanism is needed when their use is not single-stroke: this can be a spring or counterweight, or another SMA actuation in the opposite direction. Temperature changes of $15 \div 30\,\mathrm{K}$ are sufficient to activate SMAs, but higher temperatures ($\sim 100\,\mathrm{K}$) are required to achieve high actuation stresses. This results in difficulties assuring high bandwidth, requiring a high heat transfer coefficient between the heating mechanism and the alloy. Thermal inertia is also an issue [17],

6. *electro-active-polymer actuators*, or EAP. The employed material exhibits a radical change from a rigid state to a flexible one undergoing electrical or thermal inputs, recovering the “memory” form if unrestrained. This behaviour is different from SMA one, that do not change in elasticity. Their main use in aerospace is for deployable structures and smart hinges [20]. They have the capacity to expand and retract up to 200% easily and without degradation. This makes their use possible for planform transformations, like chord-length change [25],

7. *passive flexible structures*: while these are not actually actuators, a suitably designed partially flexible wing can assume particular motions when immersed in specific flow fields. An appropriate design could reduce drag. This approach is more interesting in submerged near free-surface hydrofoils, since low-frequency high-amplitude waves at the surface could “actuate” the flexible part of the wing [6]. On the other hand, it can be harder to obtain a predictable and useful “actuation” from the environment in high-Re, steady boundary conditions.

The graph proposed by Huber et al. [17] (figure 1.1) is useful to estimate the operative range of each technology. It is not up-to-date (1997) and then it underestimates the more modern technologies. The figure shows the potential and limits of the different actuations: piezoelectric ones for example are characterized by both low strain and low stress, although they increased substantially in the last 20 years. Low stresses and strains may lead to difficulties in the design phase.

The obtained deformation is a second way to categorize wing shape morphing [34]. We can have:

1. *planform deformation*, which can be divided in
    i. *span length change*, that can be used to maintain a higher efficiency in a wide range of lift coefficients. The use of pneumatic actuation could be convenient, since high displacement and low bandwidth is required [23],

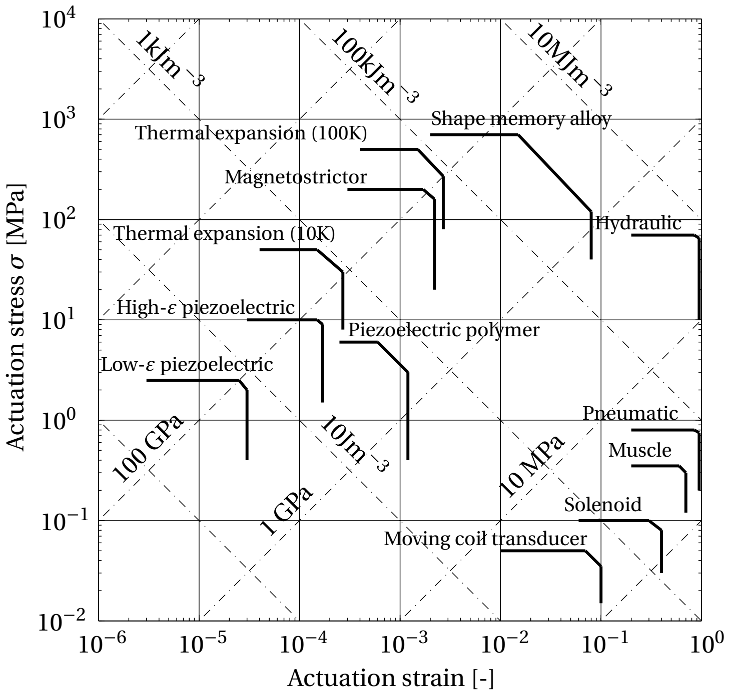

Figure 1.1: Visual representation of the strain-stress of different actuation techniques.

   ii. *chord length change*, that has similar effects to the previous one, since the parasitic and induced drag depend heavily on the aspect ratio (SPAN LENGTH/CHORD LENGTH): the former increases with it, the latter decreases. Many chord length changing systems are operational on full scale aircraft, but they mainly use movable leading and trailing edges (slats and flaps). Mechanisms closer to the shape morphing concept are rarely used in practice,

   iii. *sweep angle change*, whose effects are well known and used in aerospace industry, see the Grumman F-14 Tomcat. An application of above-cited actuations can be seen in Yu et al.'s work [38], with a SMP actuated continuous sweep change,

2. *out-of-plane deformation*, divided in

   i. *spanwise bending*, which is typical of flapping mechanisms [15]. It has become a feasible way to propel flying machines just in recent times. This is a consequence of the big steps toward the use of smart, flexible, and extremely light materials,

   ii. *chordwise bending*, fundamental type of deformation since the aerodynamic of a slender body is extremely sensitive to the camber of its sections. The extensive use of hinged structures changing locally the wing camber in the aeronautical industry, e.g. flaps, is its direct consequence,

   iii. *wing twisting*, useful for increasing lift and roll control [16],

3. *airfoil shape adjustment*, that is basically a modification in the thickness of the airfoil, without camber change, that would fall in the *chordwise bending* category.

Among all these choices, the aim of this work is to analyse piezo-actuated chordwise bending of airfoil and wing trailing edges; the main difference from most of the work done in the field will be the limited amount of chord that is capable of actively warp.

1.2 Piezoelectric effect and actuation

Some materials exhibit electrical charge when subjected to mechanical stresses, and deform when electrically charged. The electric displacement field **D** depends linearly on the applied stress **T**, while in the reverse case the deformation **S** depends linearly on the electric field vector **E**. These materials obey a linear law both mechanically and electrically, with compliance $\boldsymbol{s}$ and permittivity $\boldsymbol{\epsilon}$ respectively [30]:

$$\left.\begin{array}{lll} \text{direct piezo.} & (E_j = 0)\,, & D_i = \mathcal{d}_{ijk} T_{jk} \\ \text{reverse piezo.} & (T_{ij} = 0)\,, & S_{ij} = \mathcal{d}_{kij} E_k \\ \text{Hooke's lawp} & (E_j = 0)\,, & S_{ij} = s_{ijkl} T_{kl} \\ \text{electric displ.} & (T_{ij} = 0)\,, & D_i = \epsilon_{ij} E_j \end{array}\right\} \Rightarrow \begin{cases} S_{ij} = s^{(E=0)}_{ijkl} T_{kl} + \mathcal{d}_{kij} E_k\,, \\ D_i = \mathcal{d}_{ijk} T_{jk} + \epsilon^{(T=0)}_{ij} E_j\,, \end{cases} \tag{1.1}$$

where $\mathcal{d}$ is the piezoelectric-effect matrix, and its dimensions are CN^{-1} or mV^{-1}. Both the stress an strain tensors present symmetries, so it is possible to rearrange them in lower-order vectors and matrices without loosing information:

$$\varepsilon = \begin{pmatrix} S_{11} \\ S_{22} \\ S_{33} \\ S_{23} \\ S_{31} \\ S_{12} \end{pmatrix} = \begin{pmatrix} \varepsilon_1 \\ \varepsilon_2 \\ \varepsilon_3 \\ \gamma_{23} \\ \gamma_{31} \\ \gamma_{12} \end{pmatrix}, \quad \sigma = \begin{pmatrix} T_{11} \\ T_{22} \\ T_{33} \\ T_{23} \\ T_{31} \\ T_{12} \end{pmatrix} = \begin{pmatrix} \sigma_1 \\ \sigma_2 \\ \sigma_3 \\ \tau_{23} \\ \tau_{31} \\ \tau_{12} \end{pmatrix}, \quad \mathbf{s} = \begin{bmatrix} s_{1111} & s_{1122} & s_{1133} & s_{1123} & s_{1131} & s_{1112} \\ s_{2211} & s_{2222} & s_{2233} & s_{2223} & s_{2231} & s_{2212} \\ s_{3311} & s_{3322} & s_{3333} & s_{3323} & s_{3331} & s_{3312} \\ s_{2311} & s_{2322} & s_{2333} & s_{2323} & s_{2331} & s_{2312} \\ s_{3111} & s_{3122} & s_{3133} & s_{3123} & s_{3131} & s_{3112} \\ s_{1211} & s_{1222} & s_{1233} & s_{1223} & s_{1231} & s_{1212} \end{bmatrix}. \tag{1.2}$$

The $\mathcal{d}$ tensor is also symmetric and it is replaced by **d** accordingly:

$$\mathbf{d} = \begin{bmatrix} \mathcal{d}_{111} & \mathcal{d}_{122} & \mathcal{d}_{133} & \mathcal{d}_{123} & \mathcal{d}_{131} & \mathcal{d}_{112} \\ \mathcal{d}_{211} & \mathcal{d}_{222} & \mathcal{d}_{233} & \mathcal{d}_{223} & \mathcal{d}_{231} & \mathcal{d}_{212} \\ \mathcal{d}_{311} & \mathcal{d}_{322} & \mathcal{d}_{333} & \mathcal{d}_{323} & \mathcal{d}_{331} & \mathcal{d}_{312} \end{bmatrix}. \tag{1.3}$$

The equations (1.1) read now as

$$\begin{cases} \varepsilon_i = s^{(E=0)}_{ij} \sigma_j + d_{ji} E_j\,, \\ D_i = d_{ij} \sigma_j + \epsilon^{(E=0)}_{ij} E_j\,, \end{cases} \Rightarrow \begin{pmatrix} \boldsymbol{\varepsilon} \\ \mathbf{D} \end{pmatrix} = \begin{bmatrix} \mathbf{s}^{(E=0)} & \mathbf{d}^T \\ \mathbf{d} & \boldsymbol{\epsilon}^{(E=0)} \end{bmatrix} \begin{pmatrix} \boldsymbol{\sigma} \\ \mathbf{E} \end{pmatrix}. \tag{1.4}$$

The general agreement sets the 3rd axis as the polarization one in the **d** tensor. The two subscripts i and j indicate the direction of the deformation and the direction of the electric field inducing it. The nomenclature "d_{xy} *effect*" of the piezoelectric actuators indicates the coefficient that generates its main effect (generally d_{33}).

Among all the possible piezo-actuation systems, two appear to be more feasible to induce continuous surface deflection: piezo-stack and micro fiber composites. Both have a maximum strain of $\sim 0.1 \div 0.2\%$, corresponding to maximum strokes of $\sim 70\,\mu\mathrm{m}$ for the piezo-stacks and $\sim 150\,\mu\mathrm{m}$ for the MFCs. Other than that they have quite different properties.

Piezo-stacks are high-stiffness cylinders with typical dimensions of one centimeter and a blocking force up to 10kN. A possible use is as columns inside thick but compliant trailing edges, see for instance the last example of section 1.3. Actuators are made by stacking PZT (lead-zirconium-titanium) ceramic layers, all electrically contacted individually in a single capacitor structure; the application of an electric field induces a mechanical strain in the whole stack; a figure of merit for this configuration is the magnitude of the d_{33} coefficient. The position resolution of piezo-stacks is around the

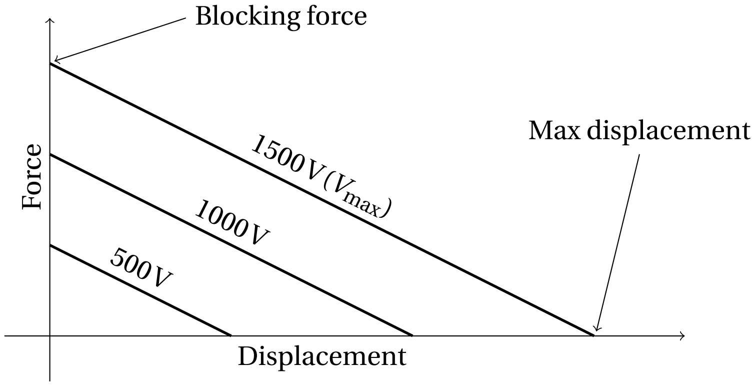

Figure 1.2: Example of displacement-force behaviour of a piezoelectric material at different voltages.

picometer [12]; this is an important parameter since the induced displacement needs to be amplified by several orders of magnitude. Their electromechanical coupling coefficient is ~ 0.5 ÷ 0.7.

Micro-fiber composites offer a very different behaviour: they are characterized by a parallel set of ceramic fibers with rectangular section in an epoxy matrix, with interdigitated electrodes. Their energy density is higher than monolithic PZT ceramic, since the electric field is in the actuation plane.
The big advantage of the fiber-matrix setup is the flexibility of the actuator, that can be glued to a compliant trailing edge.
The biggest downside is the limited blocking force employed, up to 1 kN, one tenth of the piezo-stack actuation.

MFCs have a very low specific work output due to the extremely low deformation they induce, at least compared with the feasible alternatives.
These actuators have a linear decreasing displacement-force dynamic. The blocking force is available at null displacement, while maximum displacement implies null force, as shown in figure 1.2. Using mean MCF areal density ($\mathcal{A} = 0.16\,\mathrm{g/cm^2}$), overall tabulated sizes (l_o and w_o), active tabulated sizes (l_a and w_a), and nondimensional free strain (fs) we get the following specific work (w) range,

$$w \overset{\text{def}}{=} \frac{W}{M} = \frac{\int_{s_0}^{s_f} \mathbf{F}\cdot \mathrm{d}\mathbf{s}}{\mathcal{A}\, l_o\, w_o} \overset{\text{1D}}{=} \frac{\int_{s_0}^{s_f} F\, \mathrm{d}s}{\mathcal{A}\, l_o\, w_o} = \frac{\bar{F}(s_f - s_0)}{2\mathcal{A}\, l_o\, w_o} = \frac{\bar{F}\, l_a fs}{2\mathcal{A}\, l_o\, w_o} = 0.496 \div 6.7\,\mathrm{J\,kg^{-1}}\,, \tag{1.5}$$

where W is the MFC's work, computed as the area under the graph in figure 1.2, and M the mass; the data come from models M-2503-P1 and M-8557-P1 in the Smart Material Corp. catalogue. The work term in (1.5) ($W = \bar{F}\, l_a fs/2$) is itself an interesting parameter and assumes values in between $367\,\mu\mathrm{J} \div 70.5\,\mathrm{mJ}$.

1.3 Chordwise piezoelectric actuation overview

Piezo-actuated wing morphing (macro-fiber composites and stack actuators) is mainly considered as a substitution for traditional primary control surfaces. All the considered researches using MFC had Smart Material Corp.'s hardware [21], for this reason their datasheets are used as reference in this work.

MFCs are used as actuation system mostly on micro air vehicles (MAVs). This is linked to different reasons:

1. MAVs are becoming more and more important [24],
2. there are practical limitations in experimental setups for high-Re conditions, e.g. the high cost,
3. discrete slope variations create a high risk of flow separation at low-Re conditions [5],
4. MAVs require smaller control surfaces deflection compared to full size aircrafts,

Dwarakanathan et al. [11] show a possible use of MFCs in MAVs.
The authors installed two MFC patches on the elevons in order to control them. The MAV specifications are reported in table 1.1.

component	parameter	value	component	parameter	value
MAV	weight	0.292 kg	fuselage	length	250 mm
	oper. altitude	100 m		panels thick.	0.66 mm
	range	2 km	wings	span	300 mm
	endurance	30 min		root chord	250 mm
	planform area	0.064 396 m^2		MAC	213 mm
	aspect ratio	1.45		MAC position	76.5%
elevon	length	65 mm		panels thick.	0.45 mm
	panels thick.	0.16 mm		stiffener thick.	0.66 mm
	deflection	$-3 \div 7.8$ mm	actuator	model	M-8528-P1
				spanw. position	25%

Table 1.1: MAV data from Dwarakanathan et al. research.

In the paper they validate the piezo-thermal analogy with their hardware [7]:

$$\mathbf{d}^T \mathbf{E} = \boldsymbol{\alpha}\Theta\,, \tag{1.6}$$

d is the piezoelectric strain-charge coupling matrix, **E** the electric field vector, $\boldsymbol{\alpha}$ a thermal expansion coefficient vector, and Θ a temperature (relative to a reference Θ_0). Equation (1.6) is obtained combining the thermo-elastic constitutive law and the piezoelectric one. This analogy is required to model the piezo-actuation as thermal stresses in the FE model.
Then, they investigate the real deformation of the MFC-actuated MAV elevon: it is a cambered plate made of bi-directional glass fabric (GFRP). The GFRP has a Young modulus (E) of 13 GPa, and the elevon thickness is 0.16 mm, resulting in a rather flexible structure: a length of just 65 mm allows a tip deflection of $-3 \div 7.8$ mm.

The deformation data are used in simulations at velocity 15 m s^{-1} and standard sea level conditions with MSC NASTRAN® and ANSYS FLUENT®. The first one evaluates the control derivatives with a static aeroelastic simulation, the second one runs a 2D CFD simulation of the airfoils to calculate force coefficients.

As shown in table 1.2, the results in NASTRAN® show improvements for both elevator and aileron modes, with a significant increase in roll performances:

		values [rad^{-1}]		
category	parameter	traditional	morphed	improvement [%]
derivatives	$C_{L,\delta e}$	0.387	0.485	20
	$C_{M,\delta e}$	-0.15	-0.165	9
	$C_{L,\delta a}$	0.103	0.144	28
roll performances	roll rate	192.2	268.7	28
	bank angle	20.16	30.8	34
	turn radius	62.47	38.47	38
	turn rate	13.75	22.0	38

Table 1.2: Aeroelastic simulation results from Dwarakanathan et al. research.

CFD simulations give positive results too (table 1.3):

	mean increase [%]	
parameter	upward	downward
$C_{L\max}$	3.3	6.4
E	12 (25 at 4°)	$\sim 2^*$
C_M	$\sim -10^*$	$\sim 7^*$

Table 1.3: CFD simulation results from Dwarakanathan et al. research.

The terms followed by an asterisk (*) are estimated from raster graphs and not written explicitly in Dwarakanathan et al.'s paper. Note that positive values imply an increase; this means a decrease in absolute value for negative terms, i.e. the C_M.

The conclusion of this paper shows an optimistic view on MFC-actuated primary control surfaces. This optimism can be shared with caution: a few details are reported about the simulations, and there is a lack of both aerodynamic experimental testing and setup system response to typical UAV inputs.

A more complete description of MFC-actuated aerodynamic surfaces can be found in Bilgen et al.'s work [5].
The paper provides an analysis of the piezo-actuator electrical circuitry, showing the complete electrical schematic.

Moreover MFC hysteresis is analysed. The induced camber of the wing in the transient between minimum and maximum voltage is shown to depend strongly on the sign of the voltage rate of change ($\pm 1500\,\text{V} \rightarrow \mp 1500\,\text{V}$). This effect is clearly shown in figure 1.3.

Figure 1.4 displays the airfoil setup. Note that the flexible trail and the thick airfoil have almost the same length. The wing is composed by a standard airfoil and a thin plate extending the trailing edge. The plate accounts for almost half of the wing chord and provides the compliant actuation surface. The airfoil provides the necessary bending and torsional stiffness to the wing.

A preliminary numeric study is done with XFoil [9] at Re = 310 000 and M = 0.174. It shows results for non-actuated and completely deformed trailing edge for 5 airfoils: NACA 0004, 0008, 0012, 0015, 63-

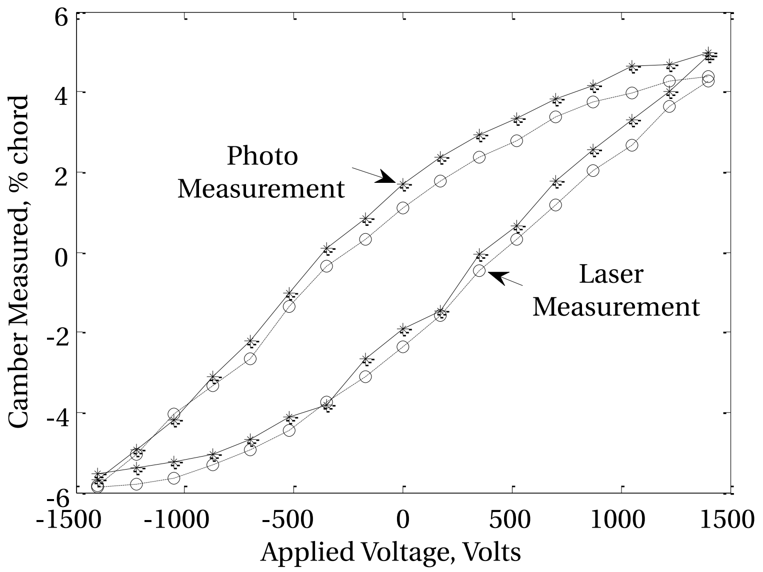

Figure 1.3: Measured effects of hysteresis in MFC actuators in Bilgen et al. research.

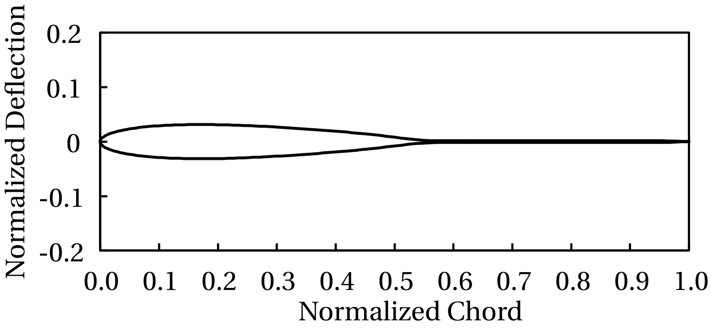

Figure 1.4: Chosen airfoil with MFC-equipped rear plate in Bilgen et al. research.

009. The chosen NACA 0015 is characterized by higher efficiency and postponed stall with both non-deflected and fully actuated trailing edge. Simulations are then processed in the complete trailing-edge-deflection range, for both root and tip airfoil. Note that the rigid part of the wing becomes smaller along the span, while the flexible one has fixed chord; this changes the compliance spanwise. The morphing airfoil and the traditional baseline show comparable performances. The actual deflection of the trailing edge in flight will probably be inferior since the simulation assumed an imposed shift. In the real case the deflection is a result of an equilibrium between internal structural stresses and external aerodynamic loads.

Then the authors evaluate the effectiveness of the control surfaces by simulating wing, stabilizer, elevator, and rudder with AVL [8]. The behaviour with null deflection is unchanged. The morphing elevator shows instead slightly inferior control authority compared to the traditional one.
Roll performances present no significant differences between traditional and morphing surfaces; it is important to notice that AVL does not calculate viscous effects or separation.

The authors tested the actual model in the wind tunnel after the simulations, and the traditional configuration showed higher roll performances compared to the morphing one (figure 1.5).
Steady-state roll-rates asymmetries are accountable to poor construction quality; the lower control autorithy is problably due to MFCs deflecting less than in the windless cases, as expected.

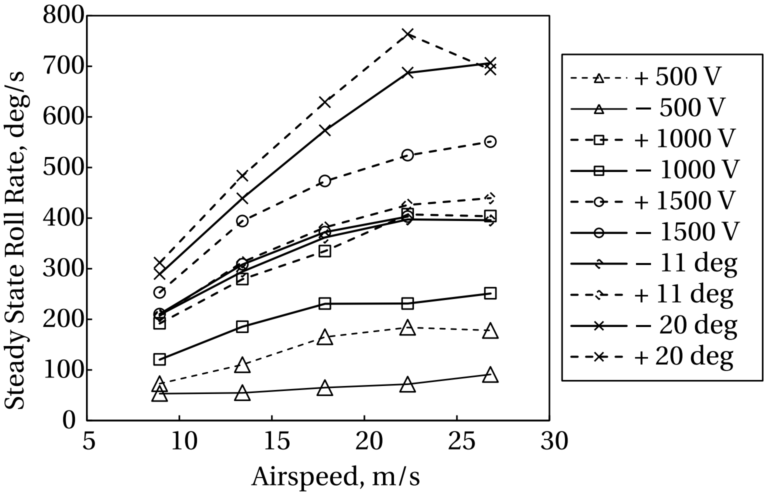

Figure 1.5: Wind tunnel results for roll performances of original and morphing vehicle.

Flight tests showed reduced handling qualities with concerns regarding the dynamic stability of the aircraft. This is probably due to the lag introduced by the high electrical capacity and MFC intrinsic hysteresis.
The results of this work can be summarised as:

1. a control with only morphing surfaces is feasible at least for small RC aircrafts,
2. MFCs can cover the whole flight envelope even at an early prototype stage,
3. the capacitance-induced lag should not be a problem in full-size aircrafts since the available electrical power is not a strong constraint, differently from RC models.

Flexible trailing edges can also be piezo-actuated without MFCs: an example (stack actuators) is in Wang et al.'s work [36]. The authors analyse various technologies in order to actively morph a wing trailing edge; among all the proposed techniques, the piezo-stack actuation (PSA) concept will be briefly overviewed here. This design uses two multiple-PSAs columns placed above and below the trailing edge neutral axis (figure 1.6) in order to generate distributed moments in the structure and bend it. A first analysis shows that the deflection achieved with this system is too small; this implies the need for hydraulic displacement amplifiers; mechanical ones would cause very strong flexural stresses at the levers.

The system was judged to be infeasible after both actuator and pump sizing: the high number of piezo-pumps needed means in fact a too high constructional complexity. The use of relaxor ferroelectric polymers (PZN-8.0%PT [27] single crystal and PVDF-TRFE [30]) instead of piezoceramics was judged more promising, but it was not available for testing.

These few chosen works represent a good example of what has already been done with piezoelectric technologies in order to deflect a wing trailing edge. It's a challenging field, mixing aerodynamics and smart structures, but with great potential.

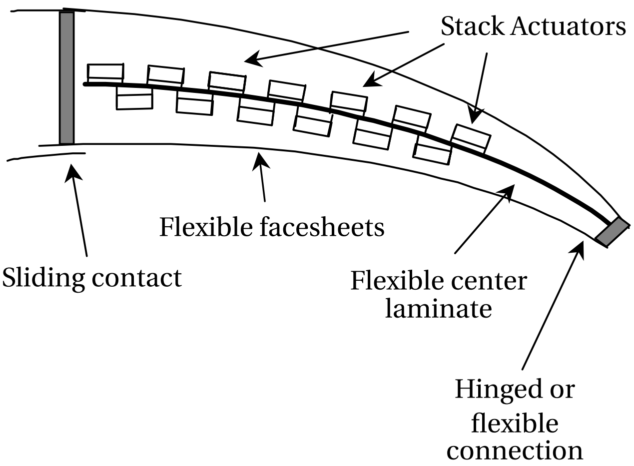

Figure 1.6: Distributed piezo-stacks with center laminate for structural stiffness at the trailing edge.

1.4 Aim of this work

The goal of this thesis is to investigate the feasibility of deformable-trailing-edge piezo-actuation, with actuating plates significantly smaller than the airfoil, up to the 20%. This is consistent with the idea of using the existing MFC actuation techniques on full scale aircraft.

Piezo-actuators on full scale aircraft will encounter higher aerodynamic loads compared to the MAV cases analysed in the previous section, but since the piezo-actuation will work only on a very small chordwise portion of the wing at the trailing edge, the Kutta condition could act in our favour reducing the work needed to deflect the wing. It can be stated as [2]:

> *A body with a sharp trailing edge in motion through a fluid creates about itself a circulation of sufficient strength to hold the rear stagnation point at the trailing edge of finite angle to make the flow along the trailing edge bisector angle smooth. For a body with a cusped trailing edge where the upper and lower surfaces meet tangentially, a smooth flow at the trailing edge requires equal velocities on both sides of the edge in the tangential direction.*

The position of the stagnation point at the trailing edge means a low pressure difference between upper and lower surface near it. This suggests that the stresses induced by the actuation system could be relatively low in order to obtain a finite tip displacement, since the forces normal to the surface are the integral of the pressure difference between top and bottom.

An encouraging clue on the importance and non-locality of small-scale and high-bandwidth actuation effects on the trailing edge can be found in Solovitz et al.'s technical notes [35]. They have chosen a controlled miniaturized Gurney flaps actuation, inducing strong non-local effects and significant lift and pitching moment variations. This hints that requiring notable effects on the airflow does not limit the designer to large actuation systems.

Chapter two

Adopted models

2.1 Introduction

In this work the performance of a trailing-edge compliant plate with MFC actuators attached on the surfaces will be explored. The plate length is significantly smaller than the airfoil chord, with a maximum (in the numerical simulations) of 20% of the chord.

The investigation will be carried out by numerical modelling, and by experiments. In this work both approaches will be pursued, experiments will be used to validate the numerical models, while numerics will be used to explore the properties of this morphing system and its performance in a few interesting applications.

The next section will explore the structural problem from a theoretical framework, adding sequentially different hypothesis in order to understand each one appropriateness. The purpose is to reach a formulation simple enough to be cycled in a fluid-structure static calculation without excessive computation time, but also without a too rough approximation of the results.

The section after will treat the aerodynamic problem. Differently from the structural one, the aerodynamic solver is not developed by the author, so the section will have a descriptive nature rather than a prescriptive one.

After the both structural and aerodynamic formulation are defined, the discussion will focus on the strictly numerical and algorithmic point of view.

2.2 Structural modelling

2.2.1 Model simplification

TThe structural problem is three-dimensional, as shown in figure2.1.
$E_{B3\mathrm{D}}$ and $E_{P3\mathrm{D}}$ are the Young moduli of the plate and piezo-actuators, respectively, while L_{ref} and L_{act} are the plate and MFC spans. We define N_{act} as the number of MFCs per L_{ref}.
The goal is to model the actuated plate as a 2D system; this will be accurate if the following assump-

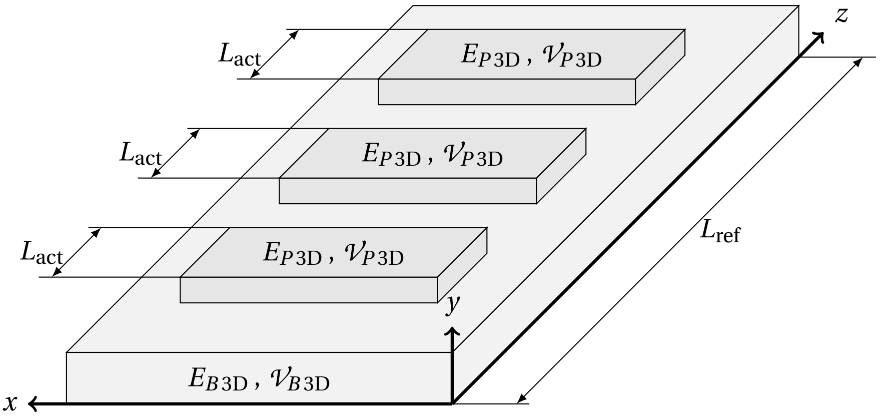

Figure 2.1: 3D plate-MFC configuration.

tions are satisfied:

1. the boundary conditions do not vary along the z dimension,
2. the loads and material properties vary slowly along the z dimension,
3. the plate compliance in the z direction is negligible compared to that along x.

The first assumption reflects an actual configuration and does not introduce any simplification in the model. The second is instead critical, since real three-dimensional wings do not have load translational symmetry along the span; in addition, the very MFC application is not spanwise continuous, and thus both forces and stiffness vary spanwise. The third consideration is not automatically satisfied like the first, but is easy to achieve by choosing appropriate orthotropic material or using spanwise stiffening systems. Notice that it is strictly necessary only to assume one between the second and third hypothesis, and since the second is difficult to achieve given the very nature of the model, the focus will be on the third.

The aforementioned hypotheses permit a substantial system simplification. The high spanwise stiffness, together with the boundary conditions, allows us to consider the strain not varying along z, i.e. $\varepsilon(x,y,z) \approx \varepsilon(x,y)$. The next formula lowers the problem dimensions:

$$\begin{aligned}\frac{1}{L_{\text{ref}}}\int_{\mathcal{V}} \varepsilon_x(x,y)E(x,y,z)\bar{\varepsilon}_x(x,y)\,\mathrm{d}\mathcal{V} &= \frac{1}{L_{\text{ref}}}\int_x\int_y\int_z \bar{\varepsilon}_x(x,y)E(x,y,z)\varepsilon_x(x,y)\,\mathrm{d}z\,\mathrm{d}y\,\mathrm{d}x \\ = \int_x\int_y \bar{\varepsilon}_x(x,y)\frac{1}{L_{\text{ref}}}\int_z E(x,y,z)\,\mathrm{d}z\,\varepsilon_x(x,y)\,\mathrm{d}y\,\mathrm{d}x &= \int_x\int_y \bar{\varepsilon}_x(x,y)E_M(x,y)\,\varepsilon_x(x,y)\,\mathrm{d}y\,\mathrm{d}x\,.\end{aligned} \tag{2.1}$$

E_M is the spanwise mean Young modulus:

$$E_M(x,y) = \frac{1}{L_{\text{ref}}}\int_z E(x,y,z)\,\mathrm{d}z\,. \tag{2.2}$$

$\mathcal{V}_P$ and $\mathcal{V}_B$ are the “2D volumes” of the system, see figure 2.2.
Considering a spanwise uniform Young modulus for both the plate and the actuator, the equivalent

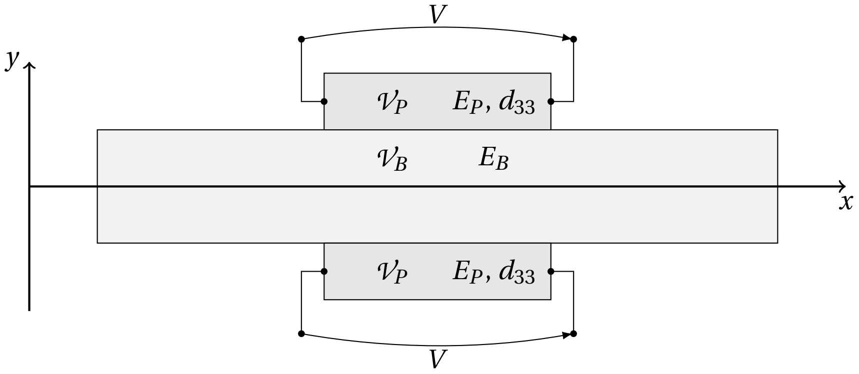

Figure 2.2: Visual representation of a beam ($\mathcal{V}_B$) with the installed piezo-actuators ($\mathcal{V}_P$). Not in scale.

Young modulus ($L_{\text{ref}}E_M$) results:

$$\begin{aligned} E(x,y) &= \begin{cases} E_B & (x,y) \in \mathcal{V}_B \,, \\ E_P & (x,y) \in \mathcal{V}_P \,, \end{cases} \\ E_B &= E_{B\,\text{3D}} \,, \\ E_P &= N_{\text{act}} \frac{L_{\text{act}}}{L_{\text{ref}}} E_{P\,\text{3D}} \,, \end{aligned} \tag{2.3}$$

Equation (2.3) is due to the mean of a uniform value being trivially the value itself, and the mean of a piecewise uniform one being the average of its values weighted on the length of the pieces.
All the structural properties are now referred to the x–y plane: it is thus possible to work with a 2D beam model.

The position of the actuators (one-sided, as in figure 2.1, or two-sided, as in figure 2.2) does not change the mathematical formulation: it is sufficient to assume the correct $\mathcal{V}_P$ depending on the case.

The virtual work principle (VWP) is a valuable tool to obtain the needed governing equations; this is a less general and mathematically sound method w.r.t. the weak formulation of the problem, but it is still widely used in engineering.
The structure is composed of the just derived 2D beam volume, with the two active MFC volumes on the top and bottom side, as shown in figure 2.2. The VWP states that, given a structure, there are three special conditions, and if two of them are satisfied, the remaining one is also valid. This conditions are:

1. «the displacements are consistent with the constraints»,
2. «all the forces are at equilibrium» (in a D'Alembertian sense, considering the inertia as a force),
3. «the total work of the aforementioned displacements and forces is null».

Notice that the displacement can be finite and not caused by the forces in the second point (that is the reason they are called "virtual").

Using the virtual displacement principle (VDP), a particular application of the generic VWP, means that an arbitrary set of virtual displacement is chosen ($virtual(x) = \overline{x}$), and the total work is imposed as null. This will lead to the set of natural boundary conditions (as opposed to the kinematic ones) and to the governing equations, that integrated will return the displacements of the structure. Searching for a static solution, the 2D work is:

$$\int_{\mathcal{V}} \overline{\boldsymbol{\varepsilon}} \cdot \boldsymbol{\sigma} \, \mathrm{d}\mathcal{V} = \int_{\mathcal{V}} \begin{pmatrix} \overline{\varepsilon}_x & \overline{\varepsilon}_y & \overline{\gamma}_{xy} \end{pmatrix} \begin{pmatrix} \sigma_x \\ \sigma_y \\ \tau_{xy} \end{pmatrix} \mathrm{d}\mathcal{V} = 0\,, \tag{2.4}$$

with $\boldsymbol{\varepsilon}(x,y)$ and $\boldsymbol{\sigma}(x,y)$ being the strain and stress vector, respectively. In this setup σ_y is tipically negligible; notice that the strain ε_y is not null neither negligible, but it works for the aforementioned negligible stresses. This results in the typical virtual work equation for a generic 2D beam:

$$\int_{\mathcal{V}} \begin{pmatrix} \overline{\varepsilon}_x & \overline{\gamma}_{xy} \end{pmatrix} \begin{pmatrix} \sigma_x \\ \tau_{xy} \end{pmatrix} \mathrm{d}\mathcal{V} = \int_{\mathcal{V}} \left(\overline{\varepsilon}_x \sigma_x + \overline{\gamma}_{xy} \tau_{xy} \right) \mathrm{d}\mathcal{V} = 0\,. \tag{2.5}$$

Since the overall structure, and all the considered portions, is quite slender, it is safe to use the Euler-Bernoulli beam model as a first approximation. This implies a null beam shear energy, and as a consequence

$$\int_{\mathcal{V}} \left(\overline{\varepsilon}_x \sigma_x + \overline{\gamma}_{xy} \tau_{xy} \right) \mathrm{d}\mathcal{V} = \int_{\mathcal{V}} \overline{\varepsilon}_x \sigma_x \, \mathrm{d}\mathcal{V} = 0\,. \tag{2.6}$$

The integral in equation (2.6) can be divided in two different domains: the beam one ($\mathcal{V}_B$) and the piezo-actuator one ($\mathcal{V}_P$):

$$\int_{\mathcal{V}} \overline{\varepsilon}_x \sigma_x \, \mathrm{d}\mathcal{V} = \int_{\mathcal{V}_B} \overline{\varepsilon}_x \sigma_x \, \mathrm{d}\mathcal{V}_B + \int_{\mathcal{V}_P} \overline{\varepsilon}_x \sigma_x \, \mathrm{d}\mathcal{V}_P\,. \tag{2.7}$$

The two subdomains are treated differently. The piezo-actuator is manipulated with linear tools in order to model it as a set of self-equilibrated external forces and modifications to the local beam stiffness. The beam is treated both non-linearly and linearly subject to such forces.

The application of a linearly-obtained set of forces (the piezo-actuator ones) in a nonlinear system (the beam model) is not a formal step, and particular care should be taken.

2.2.2 Piezoelectric model

By virtue of the superposition principle, it is possible to consider - in case of MFCs both above and below the beam - the effect of the upper and the lower separately.
A substitution of the piezoelectric characteristic equation in the single piezo-actuator work results in:

$$\left.\begin{array}{l} \sigma_x = E_P \varepsilon_x - d_{33} \frac{V}{d_e} E_P \\ W_P = \int_{\mathcal{V}_P} \overline{\varepsilon}_x \sigma_x \, \mathrm{d}\mathcal{V}_P \end{array}\right\} \Rightarrow W_P = \int_{\mathcal{V}_P} \overline{\varepsilon}_x \left(E_P \varepsilon_x - d_{33} \frac{V}{d_e} E_P \right) \mathrm{d}\mathcal{V}_P\,, \tag{2.8}$$

where d_{33} is the piezoelectric effect coefficient, E_P the Young modulus of the piezo-actuator, d_e the distance between electrodes, and V the imposed voltage.
We can assume a linear strain, i.e.

$$\varepsilon_x = \frac{\mathrm{d}u_0}{\mathrm{d}x} - y \frac{\mathrm{d}\theta_z}{\mathrm{d}x} = \frac{\mathrm{d}u_0}{\mathrm{d}x} - y \frac{\mathrm{d}^2 v_0}{\mathrm{d}x^2}\,. \tag{2.9}$$

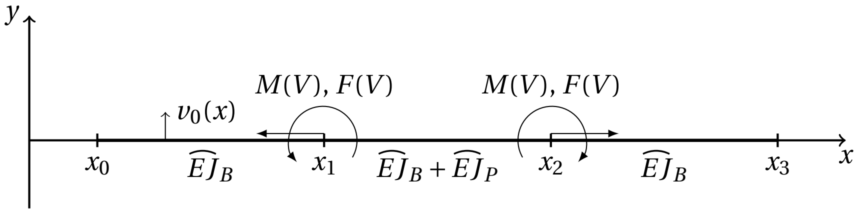

Figure 2.3: Piezo-actuated beam after the model simplification.

Applying this definition to equation (2.8) and integrating over the beam section,

$$\begin{aligned} W_P &= \int_{x_P}\int_{\mathcal{A}_P}\left(\frac{\mathrm{d}\overline{u}_0}{\mathrm{d}x} - y\frac{\mathrm{d}^2\overline{v}_0}{\mathrm{d}x^2}\right) E_P \left(\frac{\mathrm{d}u_0}{\mathrm{d}x} - y\frac{\mathrm{d}^2 v_0}{\mathrm{d}x^2}\right) \mathrm{d}\mathcal{A}_P\,\mathrm{d}x_P - \int_{x_P}\int_{\mathcal{A}_P}\left(\frac{\mathrm{d}\overline{u}_0}{\mathrm{d}x} - y\frac{\mathrm{d}^2\overline{v}_0}{\mathrm{d}x^2}\right) d_{33}\frac{V}{d_e}E_P\,\mathrm{d}\mathcal{A}_P\,\mathrm{d}x_P \\ &= \int_{x_P}\frac{\mathrm{d}\overline{u}_0}{\mathrm{d}x}\widehat{EA}_P\frac{\mathrm{d}u_0}{\mathrm{d}x}\,\mathrm{d}x_P + \int_{x_P}\frac{\mathrm{d}^2\overline{v}_0}{\mathrm{d}x^2}\widehat{EJ}_P\frac{\mathrm{d}^2 v_0}{\mathrm{d}x^2}\,\mathrm{d}x_P - \int_{x_P}\frac{\mathrm{d}^2\overline{v}_0}{\mathrm{d}x^2}\widehat{ES}_P\frac{\mathrm{d}u_0}{\mathrm{d}x}\,\mathrm{d}x_P - \int_{x_P}\frac{\mathrm{d}\overline{u}_0}{\mathrm{d}x}\widehat{ES}_P\frac{\mathrm{d}^2 v_0}{\mathrm{d}x^2}\,\mathrm{d}x_P \\ &- d_{33}\frac{V}{d_e}\widehat{EA}_P\int_{x_P}\frac{\mathrm{d}\overline{u}_0}{\mathrm{d}x}\,\mathrm{d}x_P + d_{33}\frac{V}{d_e}\widehat{ES}_P\int_{x_P}\frac{\mathrm{d}^2\overline{v}_0}{\mathrm{d}x^2}\,\mathrm{d}x_P\,, \end{aligned} \tag{2.10}$$

where S_P and J_P are respectively the section first and second order moments, and the $\widehat{EJ}$ notation means that the stiffness is not necessarily the product of E and J, but rather the result of the area integration of the product:

$$\widehat{EJ}(x) = \int_y E(x,y)J(x,y)\,\mathrm{d}y\,. \tag{2.11}$$

Applying the Torricelli-Barrow (1D Ostrogradskij) theorem to the integral of the derivative in the last term of equation (2.10) we get:

$$W_{P,\mathrm{act}} = -d_{33}\frac{V}{d_e}\widehat{EA}_P\left(\overline{u}_0\Big|_{x_{Pf}} - \overline{u}_0\Big|_{x_{Pi}}\right) + d_{33}\frac{V}{d_e}\widehat{ES}_P\left(\frac{\mathrm{d}\overline{v}_0}{\mathrm{d}x}\Big|_{x_{Pf}} - \frac{\mathrm{d}\overline{v}_0}{\mathrm{d}x}\Big|_{x_{Pi}}\right). \tag{2.12}$$

The two effects can be separated and rewritten:

$$\begin{cases} W_{1,\mathrm{act}} = -d_{33}\frac{V}{d_e}\widehat{EA}_P\left(\overline{u}_0\Big|_{x_{Pf}} - \overline{u}_0\Big|_{x_{Pi}}\right) = -F\left(\overline{u}_0(x_f) - \overline{u}_0(x_i)\right)\,, \\ W_{2,\mathrm{act}} = d_{33}\frac{V}{d_e}\widehat{ES}_P\left(\frac{\mathrm{d}\overline{v}_0}{\mathrm{d}x}\Big|_{x_{Pf}} - \frac{\mathrm{d}\overline{v}_0}{\mathrm{d}x}\Big|_{x_{Pi}}\right) = M\left(\overline{\theta}_z(x_f) - \overline{\theta}_z(x_i)\right)\,. \end{cases} \tag{2.13}$$

It is now clear how the effect of a slender piezo-actuator on the Euler-Bernoulli beam can be modelled as a couple of axial forces and bending moments with same intensity and opposite direction at the piezo-actuator extremities.

We can redefine the beam extremities as x_0 and x_3, and those of the piezo-actuator as x_1 and x_2. The simplified model is reported in figure 2.3. Modelling the forces as external causes them to change their sign. It is possible to easily find their blocking force from the piezo-actuator datasheets, and the force distance is obtainable by geometric considerations of the beam-actuator system. This means that the torque M is easier calculated using these two terms rather than $d_{33}V\widehat{ES}_P/d_e$. Since here a single piezo-actuator was considered. A two-MFCs configuration will have the sum of the two effects as force and torque. Figure 2.4 illustrates this simplification, with $F = F_{\mathrm{up}} + F_{\mathrm{low}}$ and $M = (H_B + H_P)(F_{\mathrm{up}} - F_{\mathrm{low}})/2$. The MFC linear dependence between applied force and induced displacement

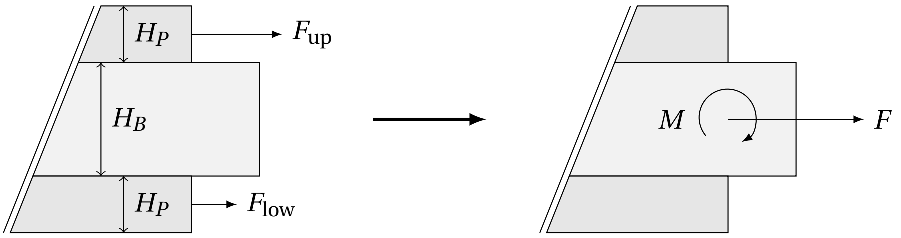

Figure 2.4: MFC actuation referred to the neutral axis.

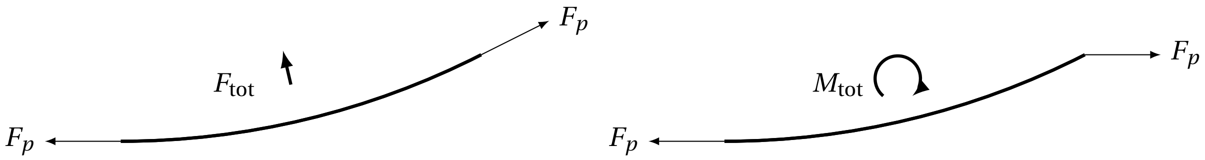

(a) Following forces case.

(b) Non-following forces case.

Figure 2.5: Endpoint forces on the beam; notice their lack of self-equilibrium.

shown in figure 1.2 is implicitly taken into account in the increased stiffness of the beam between x_2 and x_3. Notice that equation (2.10) contains terms depending on $\widehat{ES}_P$, but not V. These terms are only present when the actuators are asymmetrically mounted with respect to the beam axis, and have the equivalent effect of moving the beam neutral axis. In contrast, when they are symmetrically mounted on the upper and lower bottom their effects cancel out. This is not true for the $\widehat{ES}_P$ terms multiplied by the V, since the imposed voltage can be different on the upper and lower MFC.

2.2.3 Beam modelling

2.2.3.1 Nonlinear beam

The first approach is to adopt a nonlinear large-rotation small-strain following-forces beam model. This guarantees that the model will hold true with large displacements. The direction of the pressure forces follows the displacement of the beam, consistently with the physical nature of this load.
Modelling the MFC actuators is not straightforward: while it is reasonable to model the MFC axial force as a following one, since the piezo-actuator curves along the surface, this model is not self-equilibrating (figure 2.5a). Modelling the axial forces as as aligned with the axis of the undeformed beam suffers from this same problem (figure 2.5b). While the first part of this section will describe the difference between the models, the last part will analyse the problem with the purpose of choosing one.

In the following, the MFC is supposed to cover the whole beam, as a consequence the concentrated load will be applied to the beam endpoints. For the sake of generality a normal following force at the endpoint is also considered, despite the actuation only works with a parallel one. A representation of the system is shown in figure 2.6.

s is defined as the curvilinear coordinate of the beam, $s = L$ as the endpoint of the beam, x and y as the horizontal and vertical coordinate of a generic point, respectively. $\theta(s)$ is the local rotation of the beam, and thus $\mathrm{d}x = \mathrm{d}s \cos\theta$ and $\mathrm{d}y = \mathrm{d}s \sin\theta$. Considering the flexural equilibrium in s and the

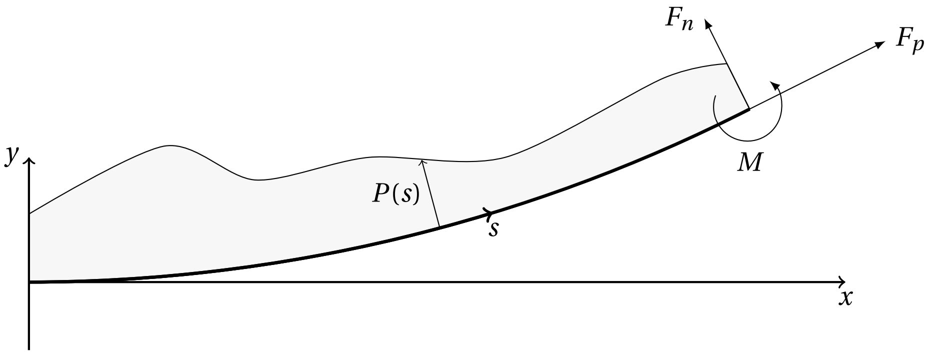

Figure 2.6: Representation of the beam model with following endpoint forces and distributed load.

geometric relation between s, x, and y, we have the following equations:

$$\begin{cases} \widehat{EJ}\dfrac{\mathrm{d}\theta}{\mathrm{d}s} = F_y\,(x(L)-x(s)) - F_x\,\big(y(L)-y(s)\big) + M + \displaystyle\int_s^L P_y(t)\,(x(t)-x(s))\,\mathrm{d}t + \int_s^L P_x(t)\,\big(y(t)-y(s)\big)\,\mathrm{d}t\,, \\ \dfrac{\mathrm{d}x}{\mathrm{d}s} = \cos\theta\,, \\ \dfrac{\mathrm{d}y}{\mathrm{d}s} = \sin\theta\,, \end{cases} \tag{2.14}$$

supplemented by the following boundary conditions:

$$\theta(0)=0\,, \qquad \widehat{EJ}\frac{\mathrm{d}\theta}{\mathrm{d}s}\bigg|_L = M\,, \qquad \widehat{EJ}\frac{\mathrm{d}^2\theta}{\mathrm{d}s^2}\bigg|_L = -F\,, \qquad x(0)=0\,, \qquad y(0)=0\,, \tag{2.15}$$

where F_x, F_y, P_x, and P_y are the projection of the forces and loads on x–y:

$$\begin{aligned} F_x &= F_p\cos\theta(L) - F_n\sin\theta(L)\,, \\ F_y &= F_n\cos\theta(L) + F_p\sin\theta(L)\,, \\ P_x(s) &= P(s)\sin\theta(s)\,, \\ P_y(s) &= P(s)\cos\theta(s)\,. \end{aligned} \tag{2.16}$$

Substituting these definitions in equation (2.14) it becomes

$$\begin{aligned} \widehat{EJ}\frac{\mathrm{d}\theta}{\mathrm{d}s} &= \big(F_n\cos\theta(L) + F_p\sin\theta(L)\big)\,(x(L)-x(s)) - \big(F_p\cos\theta(L) - F_n\sin\theta(L)\big)\,\big(y(L)-y(s)\big) + M \\ &\quad + \int_s^L P(t)\cos\theta(t)\,(x(t)-x(s))\,\mathrm{d}t + \int_s^L P(t)\sin\theta(t)\,\big(y(t)-y(s)\big)\,\mathrm{d}t\,. \end{aligned} \tag{2.17}$$

In order to compute the unknown it is useful to express the governing differential equation in the form of $\mathrm{d}^3\theta/\,\mathrm{d}s^3 = f(\theta)$, since the boundary conditions have the second derivative of the unknown. The flexural equilibrium is then derived with respect to s:

$$\begin{aligned} \widehat{EJ}\frac{\mathrm{d}^2\theta}{\mathrm{d}s^2} &= -\big(F_n\cos\theta(L) + F_p\sin\theta(L)\big)\frac{\mathrm{d}x}{\mathrm{d}s} + \big(F_p\cos\theta(L) - F_n\sin\theta(L)\big)\frac{\mathrm{d}y}{\mathrm{d}s} \\ &\quad + \frac{\mathrm{d}}{\mathrm{d}s}\left(\int_s^L P(t)\cos\theta(t)\,(x(t)-x(s))\,\mathrm{d}t\right) + \frac{\mathrm{d}}{\mathrm{d}s}\left(\int_s^L P(t)\sin\theta(t)\,\big(y(t)-y(s)\big)\,\mathrm{d}t\right). \end{aligned} \tag{2.18}$$

The third term on the RHS can be simplified applying Leibnitz's theorem [13] as follows:

$$\frac{\mathrm{d}}{\mathrm{d}s}\left(\int_s^L P(t)\cos\theta(t)\,(x(t)-x(s))\;\mathrm{d}t\right) = (P(t)\cos\theta(L)\,(x(L)-x(s)))\,\cancel{\frac{\mathrm{d}L}{\mathrm{d}s}} - (P(s)\cos\theta(s)\cancel{(x(s)-x(s))})\,\frac{\mathrm{d}s}{\mathrm{d}s}$$
$$+\int_s^L \frac{\partial}{\partial s}\,(P(t)\cos\theta(t)\,(x(t)-x(s)))\;\mathrm{d}t = \int_s^L -P(t)\cos\theta(t)\frac{\mathrm{d}x(s)}{\mathrm{d}s}\;\mathrm{d}t = -\frac{\mathrm{d}x}{\mathrm{d}s}\int_s^L P(t)\cos\theta(t)\,\mathrm{d}t\,. \tag{2.19}$$

The very same approach can be adopted, *mutatis mutandis*, for the fourth term on the right-hand side. Substituting these terms in the equilibrium gives:

$$\begin{aligned}\widehat{EJ}\frac{\mathrm{d}^2\theta}{\mathrm{d}s^2} &= -\left(F_n\cos\theta(L)+F_p\sin\theta(L)\right)\frac{\mathrm{d}x}{\mathrm{d}s}+\left(F_p\cos\theta(L)-F_n\sin\theta(L)\right)\frac{\mathrm{d}y}{\mathrm{d}s}\\ &\quad -\frac{\mathrm{d}x}{\mathrm{d}s}\int_s^L P(t)\cos\theta(t)\,\mathrm{d}t-\frac{\mathrm{d}y}{\mathrm{d}s}\int_s^L P(t)\sin\theta(t)\,\mathrm{d}t\,.\end{aligned} \tag{2.20}$$

It is possible to derive the previous equation again with respect to s:

$$\begin{aligned}\widehat{EJ}\frac{\mathrm{d}^3\theta}{\mathrm{d}s^3} &= -\left(F_n\cos\theta(L)+F_p\sin\theta(L)\right)\frac{\mathrm{d}^2x}{\mathrm{d}s^2}+\left(F_p\cos\theta(L)-F_n\sin\theta(L)\right)\frac{\mathrm{d}^2y}{\mathrm{d}s^2}\\ &\quad -\frac{\mathrm{d}^2x}{\mathrm{d}s^2}\int_s^L P(t)\cos\theta(t)\,\mathrm{d}t+\frac{\mathrm{d}x}{\mathrm{d}s}P(s)\cos\theta(s)\\ &\quad -\frac{\mathrm{d}^2y}{\mathrm{d}s^2}\int_s^L P(t)\sin\theta(t)\,\mathrm{d}t+\frac{\mathrm{d}y}{\mathrm{d}s}P(s)\sin\theta(s)\,,\end{aligned} \tag{2.21}$$

where the following relations have been used:

$$\begin{aligned}&\frac{\mathrm{d}}{\mathrm{d}s}\left(\int_s^L P(t)\cos\theta(t)\,\mathrm{d}t\right) = -P(s)\cos\theta(s)\,,\\ &\frac{\mathrm{d}}{\mathrm{d}s}\left(\int_s^L P(t)\sin\theta(t)\,\mathrm{d}t\right) = -P(s)\sin\theta(s)\,.\end{aligned} \tag{2.22}$$

Applying the chain rule we get

$$\begin{aligned}&\frac{\mathrm{d}^2x}{\mathrm{d}s^2} = \frac{\mathrm{d}\cos\theta}{\mathrm{d}s} = -\frac{\mathrm{d}\theta}{\mathrm{d}s}\sin\theta\,,\\ &\frac{\mathrm{d}^2y}{\mathrm{d}s^2} = \frac{\mathrm{d}\sin\theta}{\mathrm{d}s} = \frac{\mathrm{d}\theta}{\mathrm{d}s}\cos\theta\,;\end{aligned} \tag{2.23}$$

substituting these definitions and using the fundamental trigonometric relation $\sin^2\theta+\cos^2\theta=1$, we get the following equation:

$$\begin{aligned}\widehat{EJ}\frac{\mathrm{d}^3\theta}{\mathrm{d}s^3} &= \left(F_n\cos\theta(L)+F_p\sin\theta(L)\right)\frac{\mathrm{d}\theta}{\mathrm{d}s}\sin\theta+\left(F_p\cos\theta(L)-F_n\sin\theta(L)\right)\frac{\mathrm{d}\theta}{\mathrm{d}s}\cos\theta\\ &\quad +\int_s^L P(t)\cos\theta(t)\,\mathrm{d}t\frac{\mathrm{d}\theta}{\mathrm{d}s}\sin\theta-\int_s^L P(t)\sin\theta(t)\,\mathrm{d}t\frac{\mathrm{d}\theta}{\mathrm{d}s}\cos\theta+P(s)\,.\end{aligned} \tag{2.24}$$

This is an integro-differential equation in θ. It is possible to define appropriate functions in order to transform it in a system of ordinary differential equations. In particular, if we define the integrals as separate functions, we can rewrite them as ODEs with the integrand at the RHS, as follows:

$$\begin{aligned}&\Pi_x(s) = \int_s^L P(t)\sin\theta(t)\,\mathrm{d}t \quad\Rightarrow\quad \frac{\mathrm{d}\Pi_x}{\mathrm{d}s} = -P(s)\sin\theta(s)\,,\\ &\Pi_y(s) = \int_s^L P(t)\cos\theta(t)\,\mathrm{d}t \quad\Rightarrow\quad \frac{\mathrm{d}\Pi_y}{\mathrm{d}s} = -P(s)\cos\theta(s)\,.\end{aligned} \tag{2.25}$$

These equations need boundary condition as well, that we can obtain by observing that:

$$\Pi_x(L) = \int_L^L P(t)\sin\theta(t)\,\mathrm{d}t = 0 \qquad \text{and} \qquad \Pi_y(L) = \int_L^L P(t)\cos\theta(t)\,\mathrm{d}t = 0\,. \tag{2.26}$$

As common practice in solving ODEs, the derivative order can be decreased defining new auxiliary unknowns:

$$\begin{aligned} \frac{\mathrm{d}\theta}{\mathrm{d}s} &= \varphi \quad \Rightarrow \quad \left.\frac{\mathrm{d}\theta}{\mathrm{d}s}\right|_L = \varphi(L) = \frac{M}{EJ}\,, \\ \frac{\mathrm{d}\varphi}{\mathrm{d}s} &= \xi \quad \Rightarrow \quad \left.\frac{\mathrm{d}^2\theta}{\mathrm{d}s^2}\right|_L = \xi(L) = -\frac{F_y}{EJ}\,. \end{aligned} \tag{2.27}$$

One last step (not strictly necessary) is to remove the dependence from $\theta(L)$ in the equations, and move it in the boundary conditions. This is possible defining the following trivial equations:

$$\begin{aligned} \Gamma(s) &= \cos\theta(L) \quad \Rightarrow \quad \frac{\mathrm{d}\Gamma}{\mathrm{d}s} = 0\,, \quad \Gamma(L) = \cos\theta(L)\,, \\ \Sigma(s) &= \sin\theta(L) \quad \Rightarrow \quad \frac{\mathrm{d}\Sigma}{\mathrm{d}s} = 0\,, \quad \Sigma(L) = \sin\theta(L)\,. \end{aligned} \tag{2.28}$$

Now we have a nonlinear system of ODEs, with initial and final conditions:

$$\begin{cases} \dfrac{\mathrm{d}x}{\mathrm{d}s} = \cos\theta\,, & x(0) = 0\,, \\ \dfrac{\mathrm{d}y}{\mathrm{d}s} = \sin\theta\,, & y(0) = 0\,, \\ \dfrac{\mathrm{d}\theta}{\mathrm{d}s} = \varphi\,, & \theta(0) = 0\,, \\ \dfrac{\mathrm{d}\varphi}{\mathrm{d}s} = \xi\,, & \varphi(L) = \dfrac{M}{\widehat{EJ}}\,, \\ \dfrac{\mathrm{d}\xi}{\mathrm{d}s} = \dfrac{1}{\widehat{EJ}}\big(\big(F_p\Gamma - F_n\Sigma - \Pi_x\big)\varphi\cos\theta + \big(F_n\Gamma + F_p\Sigma + \Pi_y\big)\varphi\sin\theta + P(s)\big)\,, & \xi(L) = -\dfrac{F_n}{\widehat{EJ}}\,, \\ \dfrac{\mathrm{d}\Pi_x}{\mathrm{d}s} = -P(s)\sin\theta\,, & \Pi_x(L) = 0\,, \\ \dfrac{\mathrm{d}\Pi_y}{\mathrm{d}s} = -P(s)\cos\theta\,, & \Pi_y(L) = 0\,, \\ \dfrac{\mathrm{d}\Gamma}{\mathrm{d}s} = 0\,, & \Gamma(L) = \cos\theta(L)\,, \\ \dfrac{\mathrm{d}\Sigma}{\mathrm{d}s} = 0\,, & \Sigma(L) = \sin\theta(L)\,. \end{cases} \tag{2.29}$$

The results of this system are shown in figure 2.7. Owing to the deformation imposed by the normal load and to nonlinear effects, traction increases the deformation, as opposed to compression.

Now it is possible to simplify the model and compare the results with the general one in order to validate the simplifying assumptions.

2.2.3.2 Simplified nonlinear beam

We can simplify the model load-wise in two different ways: by neglecting the following behaviour of the distributed load, and of the concentrated forces. Figure 2.8 shows the two resulting load systems.

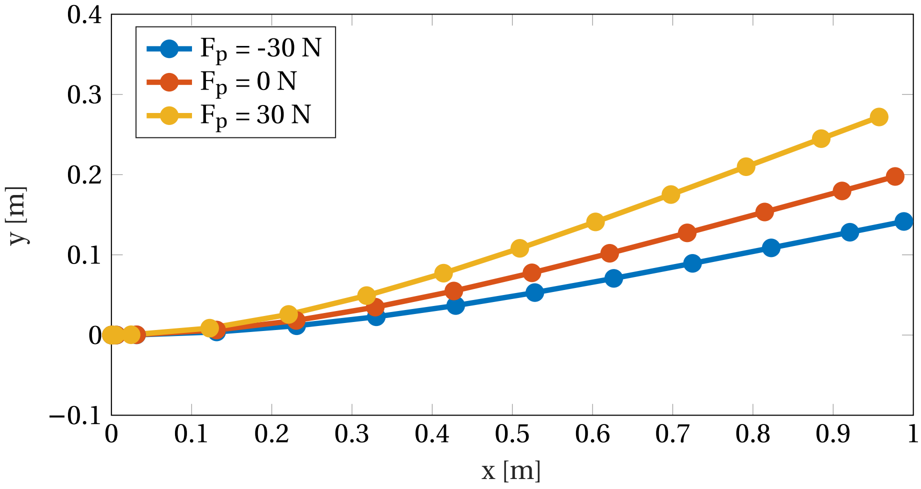

Figure 2.7: Results for a nonlinear beam with following uniform distributed load of $8\,\mathrm{N\,m^{-1}}$, flexural rigidity of $5\,\mathrm{Nm^2}$, and varying the following axial force F_p.

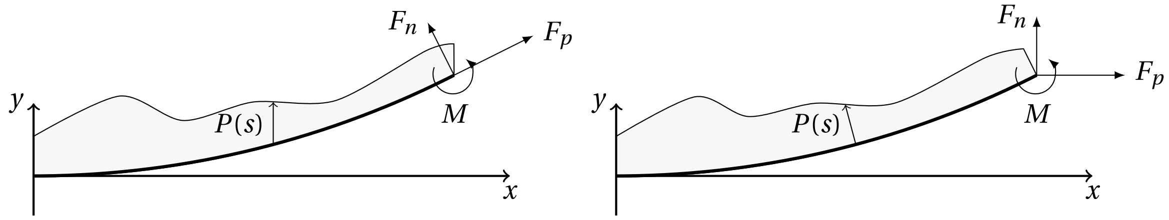

(a) Model without a following distributed load, and with following concentrated forces.

(b) Model without following concentrated forces, and with following distributed load.

Figure 2.8: Two different simplified nonlinear beam models.

This assumption roots in a 0-order approximation of θ in the load contributions. In the first case there is the following change in the equilibrium:

$$\begin{aligned}
\widehat{EJ}\frac{\mathrm{d}\theta}{\mathrm{d}s} &= \ldots + \int_s^L P(t)\cancelto{1}{\cos\theta(t)}(x(t)-x(s))\,\mathrm{d}t + \int_s^L P(t)\cancelto{0}{\sin\theta(t)}(y(t)-y(s))\,\mathrm{d}t \\
&= \ldots + \int_s^L P(t)\,(x(t)-x(s))\,\mathrm{d}t\,, \\
\widehat{EJ}\frac{\mathrm{d}^2\theta}{\mathrm{d}s^2} &= \ldots - \frac{\mathrm{d}x}{\mathrm{d}s}\int_s^L P(t)\,\mathrm{d}t\,.
\end{aligned} \tag{2.30}$$

This approximation may seem abrupt, but since the unknown is no longer present in the integral, a differential equation is obtained instead of an integro-differential one. In fact, the primitive of $P(s)$ is known, and it will be denoted with $\mathcal{P}(s)$. This results in an ODE system with two less variables (the ones defined to deal with the integrals), i.e.:

$$\begin{cases}
\dfrac{\mathrm{d}x}{\mathrm{d}s} = \cos\theta\,, & x(0) = 0\,, \\
\dfrac{\mathrm{d}y}{\mathrm{d}s} = \sin\theta\,, & y(0) = 0\,, \\
\dfrac{\mathrm{d}\theta}{\mathrm{d}s} = \varphi\,, & \theta(0) = 0\,, \\
\dfrac{\mathrm{d}\varphi}{\mathrm{d}s} = \xi\,, & \varphi(L) = \dfrac{M}{\widehat{EJ}}\,, \\
\dfrac{\mathrm{d}\xi}{\mathrm{d}s} = \dfrac{1}{\widehat{EJ}}\left(\left(F_p\Gamma - F_n\Sigma\right)\varphi\cos\theta + \left(F_n\Gamma + F_p\Sigma + \mathcal{P}(L) - \mathcal{P}(s)\right)\varphi\sin\theta\right)\,, & \xi(L) = -\dfrac{F_n}{\widehat{EJ}}\,, \\
\dfrac{\mathrm{d}\Gamma}{\mathrm{d}s} = 0\,, & \Gamma(L) = \cos\theta(L)\,, \\
\dfrac{\mathrm{d}\Sigma}{\mathrm{d}s} = 0\,, & \Sigma(L) = \sin\theta(L)\,.
\end{cases} \tag{2.31}$$

In figure 2.9 the fully nonlinear solution, eq. (2.29), is compared with that of the simplified equation (2.31). In figure 2.10 the endpoint deflection as function of the distributed load intensity (with different axial forces) is reported for the same models. The non-following model tends to approximate the following one as the load is decreased. A better understanding of their difference can be grasped by looking at figure 2.11, where the error (defined in the pseudo-equation (2.32)) is plotted as a function of the total endpoint deflection. It is possible to have errors inferior to the 5% with deflections as large as 30% of the beam length. The aforementioned error is defined as

$$\text{non-foll. model error} = \frac{\text{foll. model endpoint deflection} - \text{non-foll. model endpoint deflection}}{\text{foll. model endpoint deflection}}\,. \tag{2.32}$$

It is clear how this approximation is reasonable for small overall deformations, and the following and non-following behaviour converges when lowering the total load.

As anticipated, it is possible to model the axial forces as non-following, removing their dependence on the beam deformation:

$$\begin{aligned}
\widehat{EJ}\frac{\mathrm{d}\theta}{\mathrm{d}s} &= \left(F_n\cancelto{1}{\cos\theta(L)} + F_p\cancelto{0}{\sin\theta(L)}\right)\big(x(L)-x(s)\big) - \left(F_p\cancelto{1}{\cos\theta(L)} - F_n\cancelto{0}{\sin\theta(L)}\right)\big(y(L)-y(s)\big) + M + \ldots\,, \\
\widehat{EJ}\frac{\mathrm{d}\theta}{\mathrm{d}s} &= F_n\big(x(L)-x(s)\big) - F_p\,\big(y(L)-y(s)\big) + M + \ldots\,.
\end{aligned}$$

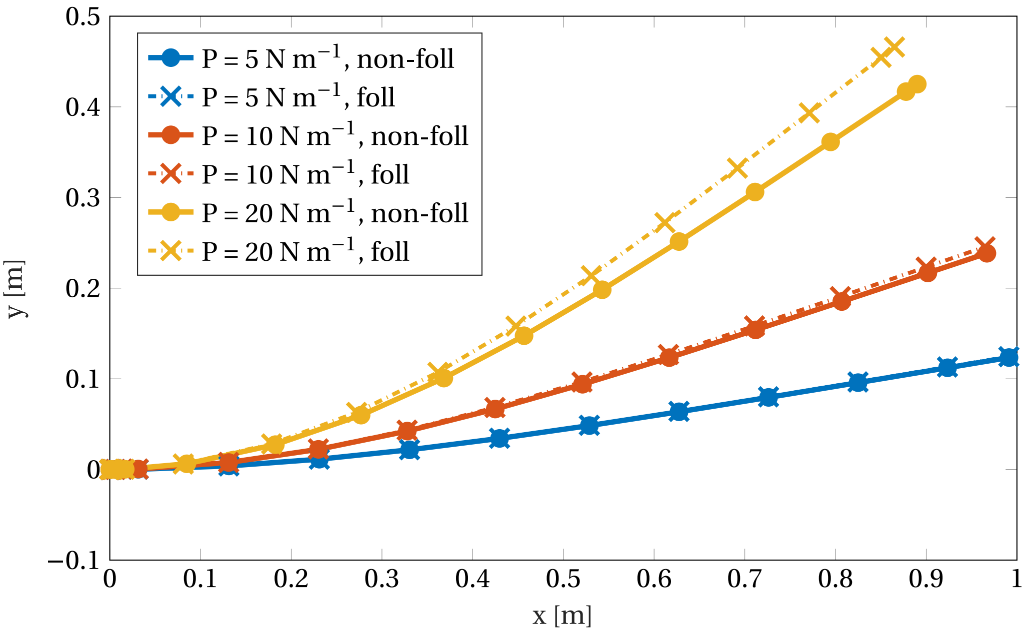

Figure 2.9: Results for a nonlinear beam with following and non-following uniform distributed P load, flexural rigidity of 5 Nm^2, and null axial force.

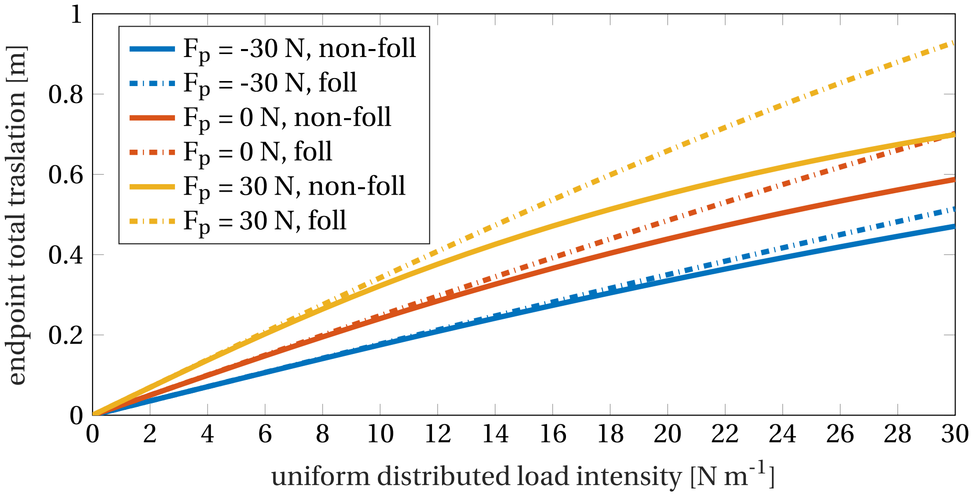

Figure 2.10: Displacement of the beam endpoint as a function of the load intensity, for the following and non-following distributed load.

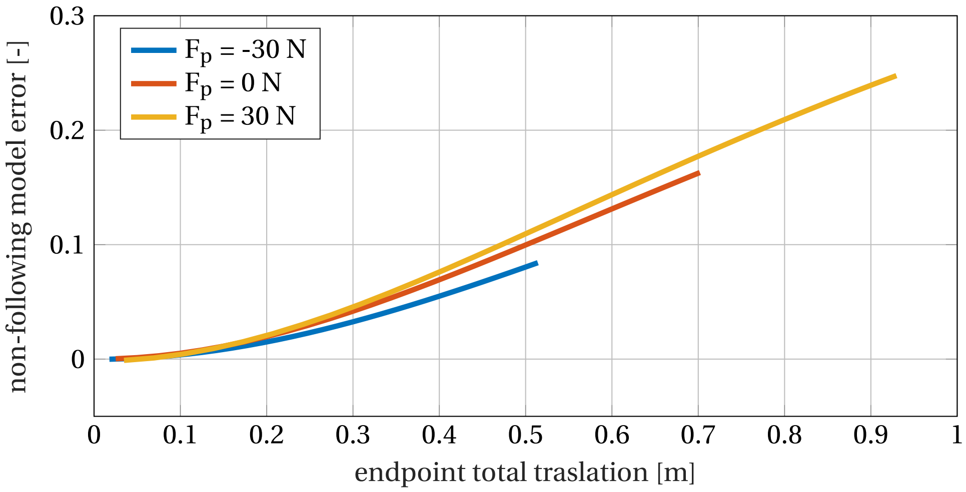

Figure 2.11: Error (defined as equation (2.32)) in modelling the pressure as non-following, as function of the total endpoint deflection.

(2.33)

Since the governing equations depend no more on $\theta(L)$, and we dealt with it in the form of two additional unknowns and equations, the system has two less equations now. It should be noticed that this simplification is applied to the original system (2.29), and not the latter one:

$$\begin{cases} \dfrac{\mathrm{d}x}{\mathrm{d}s} = \cos\theta\,, & x(0) = 0\,, \\ \dfrac{\mathrm{d}y}{\mathrm{d}s} = \sin\theta\,, & y(0) = 0\,, \\ \dfrac{\mathrm{d}\theta}{\mathrm{d}s} = \varphi\,, & \theta(0) = 0\,, \\ \dfrac{\mathrm{d}\varphi}{\mathrm{d}s} = \xi\,, & \varphi(L) = \dfrac{M}{\widehat{EJ}} \\ \dfrac{\mathrm{d}\xi}{\mathrm{d}s} = \dfrac{1}{\widehat{EJ}}\left(\left(F_p - \Pi_x\right)\varphi\cos\theta + \left(F_n + \Pi_y\right)\varphi\sin\theta + P(s)\right)\,, & \xi(L) = -\dfrac{1}{\widehat{EJ}}\left(F_n\cos\theta(L) - F_p\sin\theta(L)\right)\,, \\ \dfrac{\mathrm{d}\Pi_x}{\mathrm{d}s} = -P(s)\sin\theta\,, & \Pi_x(L) = 0\,, \\ \dfrac{\mathrm{d}\Pi_y}{\mathrm{d}s} = -P(s)\cos\theta\,, & \Pi_y(L) = 0\,. \end{cases} \tag{2.34}$$

There is a change in the boundary condition for ξ: this is due to the fact that the force is no longer aligned with the beam, and thus the boundary contribution changes with $\theta(L)$.

Figure 2.13 shows the differences between three couple of cases: the results are very different. Figure 2.12 shows the different behaviours, and the two phenomena have opposite effects.
While neglecting the following nature for the pressure give us reasonable result, the same approximation applied to the endpoint forces changes drastically the system behaviour.

With this results in mind, it is now possible to use a linear model, knowing that the pressure can be modelled as referred to the unlodead structure without changing drastically the results, but the nature of the endpoint force changes heavily the results.

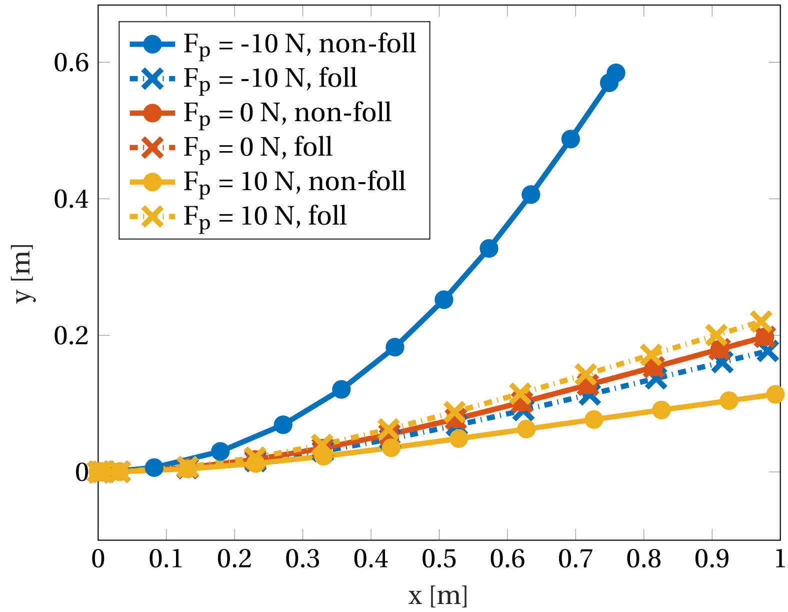

Figure 2.12: Results for a nonlinear beam with following uniform distributed load of $8\,\mathrm{N\,m^{-1}}$, flexural rigidity of $5\,\mathrm{Nm^2}$, and both following and non-following axial force F_p.

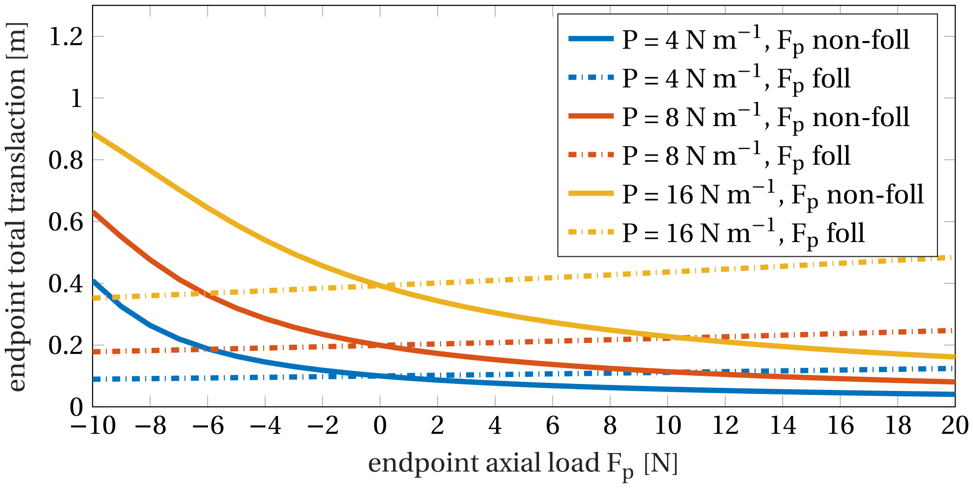

Figure 2.13: Displacement of the beam endpoint as a function of F_p (comparison between the following and non-following models).

2.2.3.3 Linear beam

Given a steady problem, the VWP states that

$$\int_{\mathcal{V}} \overline{\boldsymbol{\varepsilon}} \cdot \boldsymbol{\sigma} \, \mathrm{d}\mathcal{V} = \int_{\mathcal{V}} \overline{\mathbf{s}} \cdot \boldsymbol{\mathcal{F}} \, \mathrm{d}\mathcal{V} \,, \tag{2.35}$$

where $\mathbf{s}$ is the local displacement of the beam, and $\boldsymbol{\mathcal{F}}$ the applied forces and moments.
We consider now an Euler-Bernoulli approximations, since the beam is slender:

$$\int_{\mathcal{V}} \left(\overline{\varepsilon}_x \sigma_x + \cancel{\overline{\gamma}_{xy} \tau_{xy}} \right) \mathrm{d}\mathcal{V} = \int_{\mathcal{V}} \overline{\mathbf{s}} \cdot \boldsymbol{\mathcal{F}} \, \mathrm{d}\mathcal{V} \,. \tag{2.36}$$

For this configuration, the following boundary conditions are imposed:

$$\begin{cases} v_0(0) = 0 \,, \\ \theta(0) = \frac{\mathrm{d}v_0}{\mathrm{d}x}\Big|_0 = 0 \,, \\ u_0(0) = 0 \,. \end{cases} \tag{2.37}$$

The stresses are considered small enough to use the linear elastic constitutive equation $\sigma_x = E\varepsilon_x$:

$$\int_{\mathcal{V}} \overline{\varepsilon}_x E \varepsilon_x \, \mathrm{d}\mathcal{V} = \int_{\mathcal{V}} \overline{\mathbf{s}} \cdot \boldsymbol{\mathcal{F}} \, \mathrm{d}\mathcal{V} \,, \tag{2.38}$$

as already remarked, this assumption is valid if deformations are small.
It is possible to substitute a strain definition that takes into account the contribution of large rotations [29]. These are called the Von Karman strains.

$$\varepsilon_x = \frac{\mathrm{d}u_0}{\mathrm{d}x} - y \frac{\mathrm{d}^2 v_0}{\mathrm{d}x^2} + \frac{1}{2} \left(\frac{\mathrm{d}v_0}{\mathrm{d}x} \right)^2 \tag{2.39}$$

The nonlinearity associated with large rotations is taken into account, despite the aim is a linear formulation, since strain nonlinearities can (and in this case, will) manifest linearly in the final governing equation.
Keeping this in mind, we now substitute the strain expressed in equation (2.39). The external forces are limited to a distributed load Q, and the terms $\mathcal{F}_x$, $\mathcal{F}_y$, and $\mathcal{M}$, respectively two forces and a moment, which are distributed on area at $x = l$:

$$\begin{aligned} &\int_{\mathcal{V}} \left(\frac{\mathrm{d}\overline{u}_0}{\mathrm{d}x} - y \frac{\mathrm{d}^2 \overline{v}_0}{\mathrm{d}x^2} + \frac{1}{2} \overline{\left(\frac{\mathrm{d}v_0}{\mathrm{d}x} \right)^2} \right) E \left(\frac{\mathrm{d}u_0}{\mathrm{d}x} - y \frac{\mathrm{d}^2 v_0}{\mathrm{d}x^2} + \frac{1}{2} \left(\frac{\mathrm{d}v_0}{\mathrm{d}x} \right)^2 \right) \\ &= \int_{\mathcal{V}} \left(\overline{v}_0 Q + \overline{u}_0 \delta(x-l) \mathcal{F}_x + \overline{v}_0 \delta(x-l) \mathcal{F}_y + \frac{\mathrm{d}\overline{v}_0}{\mathrm{d}x} \delta(x-l) \mathcal{M} \right) \mathrm{d}\mathcal{V} \,. \end{aligned} \tag{2.40}$$

The $\delta(x - a)$ symbol indicates a Dirac delta distribution centered in a.

We now develop individually every part of the LHS of the last equation. Starting with $\overline{u}_0$, we can hypothesise symmetry, so that $\widehat{ES} = 0$, integrate on the beam section, and apply integration and the Torricelli-Barrow theorem to get:

$$\begin{aligned} \int_{\mathcal{V}} \frac{\mathrm{d}\overline{u}_0}{\mathrm{d}x} E \left(\frac{\mathrm{d}u_0}{\mathrm{d}x} - y \frac{\mathrm{d}^2 v_0}{\mathrm{d}x^2} + \frac{1}{2} \left(\frac{\mathrm{d}v_0}{\mathrm{d}x} \right)^2 \right) \mathrm{d}\mathcal{V} &= \int_l \frac{\mathrm{d}\overline{u}_0}{\mathrm{d}x} \left(\widehat{EA} \frac{\mathrm{d}u_0}{\mathrm{d}x} - \cancelto{0}{\widehat{ES}} \frac{\mathrm{d}^2 v_0}{\mathrm{d}x^2} + \frac{\widehat{EA}}{2} \left(\frac{\mathrm{d}v_0}{\mathrm{d}x} \right)^2 \right) \mathrm{d}x \\ &= \left[\overline{u}_0 \left(\widehat{EA} \frac{\mathrm{d}u_0}{\mathrm{d}x} + \frac{\widehat{EA}}{2} \left(\frac{\mathrm{d}v_0}{\mathrm{d}x} \right)^2 \right) \right]_0^l - \int_l \overline{u}_0 \left(\widehat{EA} \frac{\mathrm{d}^2 u_0}{\mathrm{d}x^2} + \widehat{EA} \frac{\mathrm{d}v_0}{\mathrm{d}x} \frac{\mathrm{d}^2 v_0}{\mathrm{d}x^2} \right) \mathrm{d}x \,. \end{aligned} \tag{2.41}$$

The same procedure can be replicated for the terms multiplied to $\mathrm{d}^2(\overline{v}_0)/\mathrm{d}x^2$

$$\begin{aligned}\int_{\mathcal{V}} -y\frac{\mathrm{d}^2\overline{v}_0}{\mathrm{d}x^2}E\left(\frac{\mathrm{d}u_0}{\mathrm{d}x}-y\frac{\mathrm{d}^2v_0}{\mathrm{d}x^2}+\frac{1}{2}\left(\frac{\mathrm{d}v_0}{\mathrm{d}x}\right)^2\right)\mathrm{d}\mathcal{V} &= \int_l -\frac{\mathrm{d}^2\overline{v}_0}{\mathrm{d}x^2}\left(\cancelto{0}{\widehat{ES}}\frac{\mathrm{d}u_0}{\mathrm{d}x}-\widehat{EJ}\frac{\mathrm{d}^2v_0}{\mathrm{d}x^2}+\frac{\cancelto{0}{\widehat{ES}}}{2}\left(\frac{\mathrm{d}v_0}{\mathrm{d}x}\right)^2\right)\mathrm{d}x \\ = \left[\frac{\mathrm{d}\overline{v}_0}{\mathrm{d}x}\left(\widehat{EJ}\frac{\mathrm{d}^2v_0}{\mathrm{d}x^2}\right)\right]_0^l-\int_l\frac{\mathrm{d}\overline{v}_0}{\mathrm{d}x}\widehat{EJ}\frac{\mathrm{d}^3v_0}{\mathrm{d}x^3} &= \left[\frac{\mathrm{d}\overline{v}_0}{\mathrm{d}x}\left(\widehat{EJ}\frac{\mathrm{d}^2v_0}{\mathrm{d}x^2}\right)\right]_0^l-\left[\overline{v}_0\left(\widehat{EJ}\frac{\mathrm{d}^3v_0}{\mathrm{d}x^3}\right)\right]_0^l+\int_l\overline{v}_0\widehat{EJ}\frac{\mathrm{d}^4v_0}{\mathrm{d}x^4}\,.\end{aligned} \tag{2.42}$$

Before manipulating the terms multiplied containing the term $1/2(\mathrm{d}(\overline{v}_0)/\mathrm{d}x)^2$, it is necessary to apply the general *virtual* definition

$$\overline{f(z)}=\frac{\mathrm{d}f(z)}{\mathrm{d}z}\overline{z} \tag{2.43}$$

to the nonlinear virtual term:

$$\overline{\frac{1}{2}\left(\frac{\mathrm{d}v_0}{\mathrm{d}x}\right)^2}=\frac{1}{2}\frac{\mathrm{d}\left(\frac{\mathrm{d}v_0}{\mathrm{d}x}\right)^2}{\mathrm{d}x}\overline{x}=2\frac{1}{2}\frac{\mathrm{d}v_0}{\mathrm{d}x}\frac{\mathrm{d}\frac{\mathrm{d}v_0}{\mathrm{d}x}}{\mathrm{d}x}\overline{x}=\frac{\mathrm{d}v_0}{\mathrm{d}x}\overline{\frac{\mathrm{d}v_0}{\mathrm{d}x}}\,. \tag{2.44}$$

Manipulating the part of equation (2.40) multiplied by the nonlinear virtual term yields:

$$\begin{aligned}\int_{\mathcal{V}}\frac{\mathrm{d}\overline{v}_0}{\mathrm{d}x}\frac{\mathrm{d}v_0}{\mathrm{d}x}E\left(\frac{\mathrm{d}u_0}{\mathrm{d}x}-y\frac{\mathrm{d}^2v_0}{\mathrm{d}x^2}+\frac{1}{2}\left(\frac{\mathrm{d}v_0}{\mathrm{d}x}\right)^2\right)\mathrm{d}\mathcal{V} &= \int_l\frac{\mathrm{d}\overline{v}_0}{\mathrm{d}x}\left(\widehat{EA}\frac{\mathrm{d}u_0}{\mathrm{d}x}\frac{\mathrm{d}v_0}{\mathrm{d}x}-\cancelto{0}{\widehat{ES}}\frac{\mathrm{d}^2v_0}{\mathrm{d}x^2}\frac{\mathrm{d}u_0}{\mathrm{d}x}+\frac{\widehat{EA}}{2}\left(\frac{\mathrm{d}v_0}{\mathrm{d}x}\right)^3\right)\mathrm{d}x \\ = \left[\overline{v}_0\left(\widehat{EA}\frac{\mathrm{d}u_0}{\mathrm{d}x}\frac{\mathrm{d}v_0}{\mathrm{d}x}+\frac{\widehat{EA}}{2}\left(\frac{\mathrm{d}v_0}{\mathrm{d}x}\right)^3\right)\right]_0^l &- \int_l\overline{v}_0\widehat{EA}\left(\frac{\mathrm{d}^2u_0}{\mathrm{d}x^2}\frac{\mathrm{d}v_0}{\mathrm{d}x}+\frac{\mathrm{d}u_0}{\mathrm{d}x}\frac{\mathrm{d}^2v_0}{\mathrm{d}x^2}+\frac{3}{2}\left(\frac{\mathrm{d}v_0}{\mathrm{d}x}\right)^2\frac{\mathrm{d}^2v_0}{\mathrm{d}x^2}\right)\mathrm{d}x\,.\end{aligned} \tag{2.45}$$

At the RHS of equation (2.40) we can exploit the properties of the Dirac delta, and consider the external forces as only depending on the x position:

$$\int_{\mathcal{V}}\left(\overline{v}_0Q+\overline{u}_0\delta(x-l)\mathcal{F}_x+\overline{v}_0\delta(x-l)\mathcal{F}_y+\frac{\mathrm{d}\overline{v}_0}{\mathrm{d}x}\delta(x-l)\mathcal{M}\right)\mathrm{d}\mathcal{V}=\int_l\overline{v}_0q\,\mathrm{d}x+\overline{u}_0(l)F_x+\overline{v}_0(l)F_y+\left.\frac{\mathrm{d}\overline{v}_0}{\mathrm{d}x}\right|_l M\,, \tag{2.46}$$

where

$$\begin{aligned}q(x)&=\int_y\int_z Q(x,y,z)\,\mathrm{d}z\,\mathrm{d}y\,,\\ F_x(x)&=\int_y\int_z\mathcal{F}_x(x,y,z)\,\mathrm{d}z\,\mathrm{d}y\,,\\ F_y(x)&=\int_y\int_z\mathcal{F}_y(x,y,z)\,\mathrm{d}z\,\mathrm{d}y\,.\end{aligned} \tag{2.47}$$

We can now regroup all the terms together dropping the ones working for a constrained displacement and get

$$
\begin{aligned}
&\int_l \overline{v}_0 \left[\widehat{EJ}\frac{\mathrm{d}^4 v_0}{\mathrm{d}x^4} - \frac{3}{2}\widehat{EA}\left(\frac{\mathrm{d}v_0}{\mathrm{d}x}\right)^2 \frac{\mathrm{d}^2 v_0}{\mathrm{d}x^2} - \widehat{EA}\frac{\mathrm{d}\frac{\mathrm{d}u_0}{\mathrm{d}x}\frac{\mathrm{d}v_0}{\mathrm{d}x}}{\mathrm{d}x} - q \right] \mathrm{d}x \\
&+ \int_l \overline{u}_0 \left[\widehat{EA}\frac{\mathrm{d}^2 u_0}{\mathrm{d}x^2} + \widehat{EA}\frac{\mathrm{d}v_0}{\mathrm{d}x}\frac{\mathrm{d}^2 v_0}{\mathrm{d}x^2} \right] \mathrm{d}x \\
&+ \overline{v}_0(l) \left[-\widehat{EJ}\frac{\mathrm{d}^3 v_0}{\mathrm{d}x^3}\bigg|_l + \widehat{EA}\frac{\mathrm{d}u_0}{\mathrm{d}x}\bigg|_l \frac{\mathrm{d}v_0}{\mathrm{d}x}\bigg|_l + \frac{\widehat{EA}}{2}\left(\frac{\mathrm{d}v_0}{\mathrm{d}x}\bigg|_l\right)^3 - F_y \right] \\
&+ \frac{\mathrm{d}\overline{v}_0}{\mathrm{d}x}\bigg|_l \left[\widehat{EJ}\frac{\mathrm{d}^2 v_0}{\mathrm{d}x^2}\bigg|_l - M \right] \\
&+ \overline{u}_0(l) \left[\widehat{EA}\frac{\mathrm{d}u_0}{\mathrm{d}x}\bigg|_l + \frac{\widehat{EA}}{2}\left(\frac{\mathrm{d}v_0}{\mathrm{d}x}\bigg|_l\right)^2 - F_x \right] = 0\,.
\end{aligned}
\tag{2.48}
$$

The independence of the virtual displacements from the actual ones allows us to consider individually every part of the equation and get two governing equations and three natural boundary conditions; adding these to the kinematic ones, we obtain the following system:

$$
\begin{cases}
\widehat{EJ}\dfrac{\mathrm{d}^4 v_0}{\mathrm{d}x^4} - \dfrac{3}{2}\widehat{EA}\left(\dfrac{\mathrm{d}v_0}{\mathrm{d}x}\right)^2 \dfrac{\mathrm{d}^2 v_0}{\mathrm{d}x^2} - \widehat{EA}\dfrac{\mathrm{d}^2 u_0}{\mathrm{d}x^2}\dfrac{\mathrm{d}v_0}{\mathrm{d}x} - \widehat{EA}\dfrac{\mathrm{d}u_0}{\mathrm{d}x}\dfrac{\mathrm{d}^2 v_0}{\mathrm{d}x^2} = q\,, \\
\widehat{EA}\dfrac{\mathrm{d}^2 u_0}{\mathrm{d}x^2} + \widehat{EA}\dfrac{\mathrm{d}v_0}{\mathrm{d}x}\dfrac{\mathrm{d}^2 v_0}{\mathrm{d}x^2} = 0\,,
\end{cases}
\tag{2.49}
$$

supplemented with the boundary conditions:

$$
\begin{cases}
\widehat{EJ}\frac{\mathrm{d}^2 v_0}{\mathrm{d}x^2}\Big|_l = M\,, \\
\widehat{EJ}\frac{\mathrm{d}^3 v_0}{\mathrm{d}x^3}\Big|_l - \widehat{EA}\frac{\mathrm{d}u_0}{\mathrm{d}x}\Big|_l \frac{\mathrm{d}v_0}{\mathrm{d}x}\Big|_l - \frac{\widehat{EA}}{2}\left(\frac{\mathrm{d}v_0}{\mathrm{d}x}\Big|_l\right)^3 = -F_y\,, \\
\widehat{EA}\frac{\mathrm{d}u_0}{\mathrm{d}x}\Big|_l + \frac{\widehat{EA}}{2}\left(\frac{\mathrm{d}v_0}{\mathrm{d}x}\Big|_l\right)^2 = F_x\,.
\end{cases}
\tag{2.50}
$$

Manipulating the axial equilibrium term in equation (2.49) and integrating it (applying the corresponding boundary condition as integration constant) it becomes:

$$
\begin{aligned}
\widehat{EA}\frac{\mathrm{d}^2 u_0}{\mathrm{d}x^2} &= -\widehat{EA}\frac{\mathrm{d}v_0}{\mathrm{d}x}\frac{\mathrm{d}^2 v_0}{\mathrm{d}x^2}\,, \\
\widehat{EA}\frac{\mathrm{d}u_0}{\mathrm{d}x} &= -\frac{\widehat{EA}}{2}\left(\frac{\mathrm{d}v_0}{\mathrm{d}x}\right)^2 + \widehat{EA}\frac{\mathrm{d}u_0}{\mathrm{d}x}\bigg|_L + \frac{\widehat{EA}}{2}\left(\frac{\mathrm{d}v_0}{\mathrm{d}x}\bigg|_L\right)^2 \overset{\text{B.C.}}{=} -\frac{\widehat{EA}}{2}\left(\frac{\mathrm{d}v_0}{\mathrm{d}x}\right)^2 + F_x\,.
\end{aligned}
\tag{2.51}
$$

These terms substituted in the flexural equilibrium in equation (2.49) yield:

$$
\widehat{EJ}\frac{\mathrm{d}^4 v_0}{\mathrm{d}x^4} - \frac{3}{2}\widehat{EA}\left(\frac{\mathrm{d}v_0}{\mathrm{d}x}\right)^2 \frac{\mathrm{d}^2 v_0}{\mathrm{d}x^2} + \widehat{EA}\left(\frac{\mathrm{d}v_0}{\mathrm{d}x}\right)^2 \frac{\mathrm{d}^2 v_0}{\mathrm{d}x^2} + \frac{\widehat{EA}}{2}\left(\frac{\mathrm{d}v_0}{\mathrm{d}x}\right)^2 \frac{\mathrm{d}^2 v_0}{\mathrm{d}x^2} - F_p\frac{\mathrm{d}^2 v_0}{\mathrm{d}x^2} = q\,.
\tag{2.52}
$$

The application of the boundary conditions (equation (2.50)) in equation (2.52) yelds to:

$$
\widehat{EJ}\frac{\mathrm{d}^3 v_0}{\mathrm{d}x^3}\bigg|_l - F_p\frac{\mathrm{d}v_0}{\mathrm{d}x}\bigg|_l + \frac{\widehat{EA}}{2}\left(\frac{\mathrm{d}v_0}{\mathrm{d}x}\bigg|_l\right)^3 - \frac{\widehat{EA}}{2}\left(\frac{\mathrm{d}v_0}{\mathrm{d}x}\bigg|_l\right)^3 = -F_y\,.
\tag{2.53}
$$

The model does not consider the nature of the axial forces since this point.
It is possible now to hypothesize them as following, non-following, or neglectable.

Given that the forces have a following nature, the overall horizontal and vertical forces can be defined as a function of the parallel (F_p) and normal (F_n) component as:

$$\begin{aligned} F_x &= F_p \cos\theta(L) - F_n \sin\theta(L)\,, \\ F_y &= F_n \cos\theta(L) + F_p \sin\theta(L)\,. \end{aligned} \tag{2.54}$$

Plugging these relation in equation (2.53) leads to:

$$\widehat{EJ}\frac{\mathrm{d}^3 v_0}{\mathrm{d}x^3}\bigg|_l - \big(F_p\cos\theta(L) - F_n\sin\theta(L)\big)\frac{\mathrm{d}v_0}{\mathrm{d}x}\bigg|_l = -\big(F_n\cos\theta(L) + F_p\sin\theta(L)\big)\,. \tag{2.55}$$

Some manipulations and the definition of θ in an Euler-Bernoulli beam yields:

$$\widehat{EJ}\frac{\mathrm{d}^3 v_0}{\mathrm{d}x^3}\bigg|_l + F_p\big(\sin\theta_L - \theta_L\cos\theta_L\big) + F_n\big(\theta_L\sin\theta_L - \cos\theta_L\big) = 0\,, \tag{2.56}$$

where $\theta(L) = \theta_L$
The terms depending on θ_L can be expanded in Taylor series as follows:

$$\begin{aligned} &\sin\theta_L - \theta_L\cos\theta_L \overset{\mathrm{T}}{=} 0 + O\big(\theta_L^3\big)\,, \\ &\theta_L\sin\theta_L + \cos\theta_L \overset{\mathrm{T}}{=} 1 + O\big(\theta_L^2\big)\,. \end{aligned} \tag{2.57}$$

Substituting back the relation between θ and v_0 and the linearized terms of equation (2.57) the governing equation becomes:

$$\widehat{EJ}\frac{\mathrm{d}^4 v_0}{\mathrm{d}x^4} - F_p\frac{\mathrm{d}^2 v_0}{\mathrm{d}x^2} = q\,, \tag{2.58}$$

and the boundary conditions:

$$v_0(0) = 0 \quad , \quad \frac{\mathrm{d}v_0}{\mathrm{d}x}\bigg|_0 = 0 \quad , \quad \widehat{EJ}\,\frac{\mathrm{d}^2 v_0}{\mathrm{d}x^2}\bigg|_l = M \quad , \quad \widehat{EJ}\,\frac{\mathrm{d}^3 v_0}{\mathrm{d}x^3}\bigg|_l = -F_n\,. \tag{2.59}$$

Figure 2.14 illustrates exemplificative beam deformations in with both nonlinear and linear solver; it is evident how at a given x values the two methods output very similar y. This is due to the method considering the nonlinear large rotation in its linear governing equation. The most noticeable difference is in the total beam length. The linear method has the endpoint always as $x = L$, resulting in a longer beam w.r.t. the nonlinear and the real case when deflected. This effect is particularly evident with large rotation.

Figure 2.15 shows the endpoint vertical position as a distributed load intensity function, at different F_p, while figure 2.16 shows the distance between linear and nonlinear endpoints at the same condition, defined as “linear model error”, which is also a reasonable esteem of the length added by the linear model.
An important note is the computation time for linear and nonlinear formulations. The computational time for the linear solution is not function of the structure parameters, while figure 2.17 shows how high tractions on the beam can influence of the load level on the computation time.

Neglecting the following nature of the forces results in simply considering the equation (2.60) instead of (2.54).

$$\begin{aligned} F_x &= F_p\,, \\ F_y &= F_n\,. \end{aligned} \tag{2.60}$$

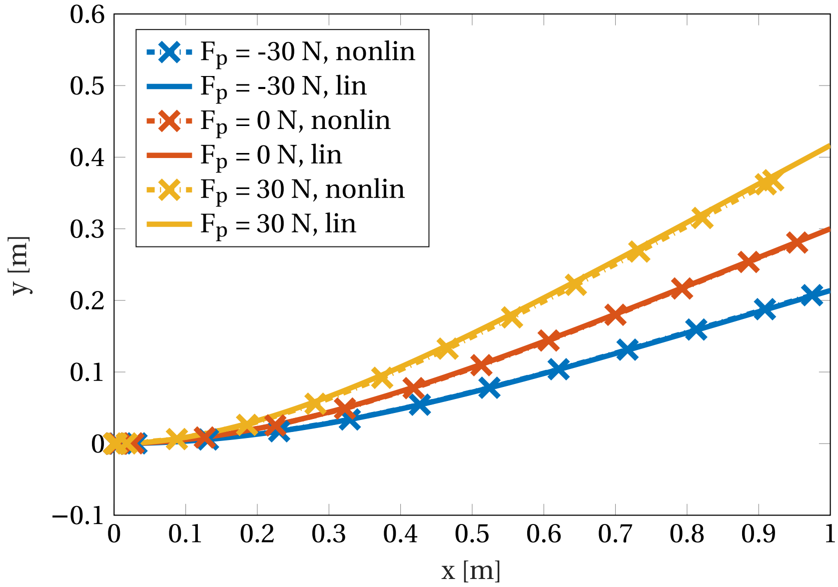

Figure 2.14: Example of beam deformations with different F_p and a uniform distributed load of $12\,\mathrm{N\,m^{-1}}$, with both linear and nonlinear solver.

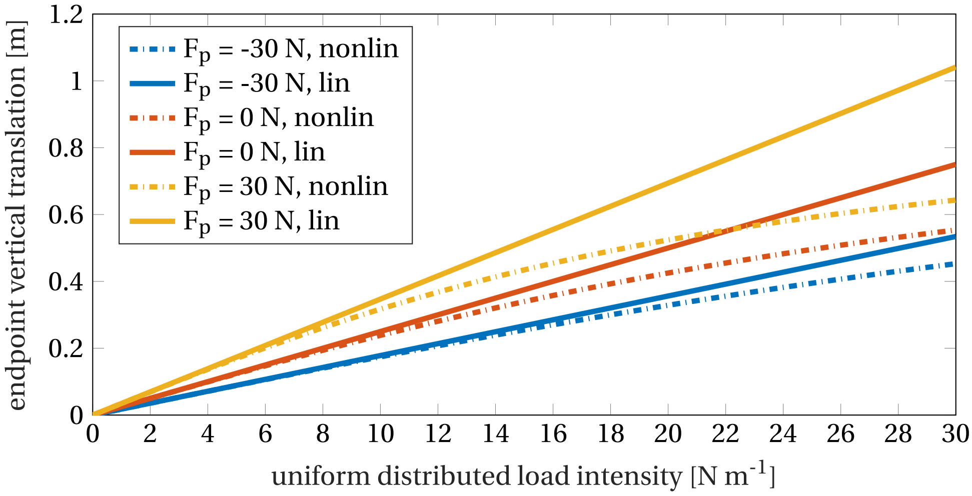

Figure 2.15: Differences between the linear and nonlinear model with following endpoint forces, as function of the uniform distributed load intensity.

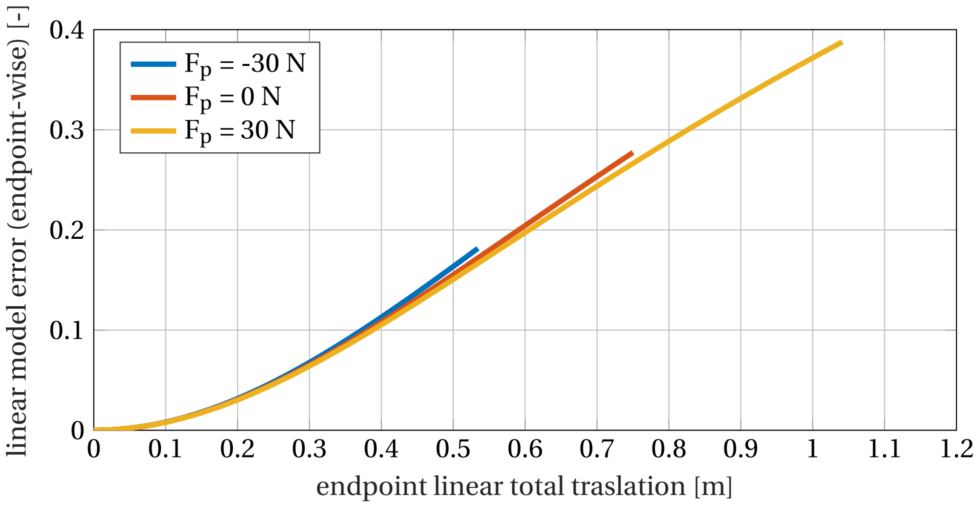

Figure 2.16: Error of the linear following-forces model w.r.t. the nonlinear one, as function of the endpoint deflection, at various axial forces.

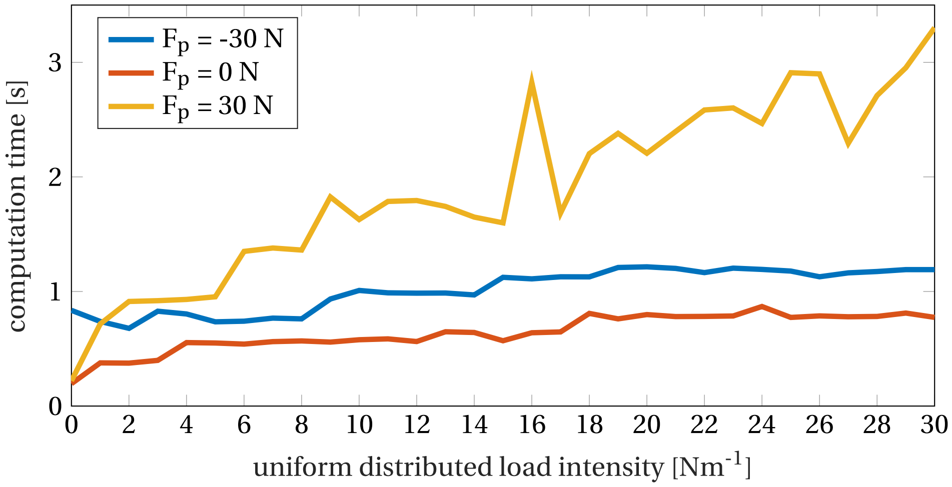

Figure 2.17: Computation time for the nonlinear model; for comparison the average linear calculation on the same computer takes just 0.0013 s.

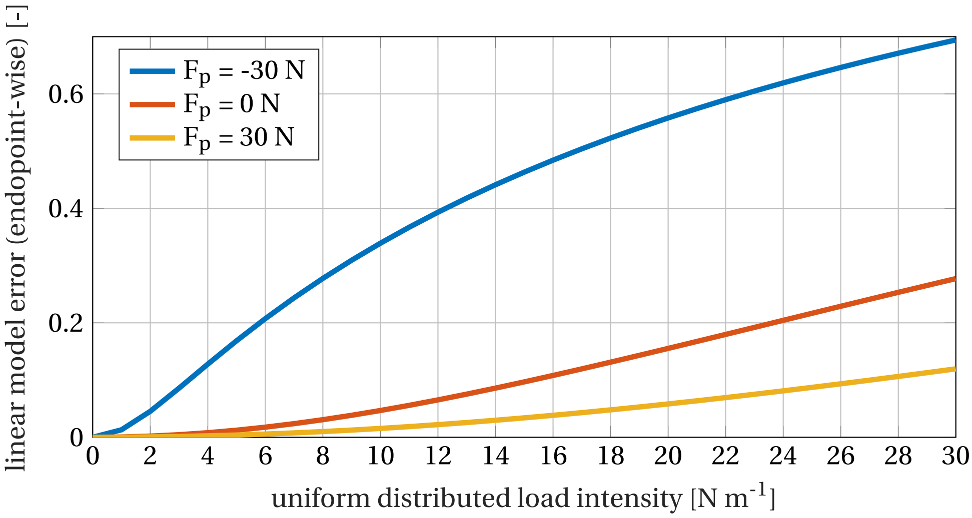

Figure 2.18: Linear model error w.r.t. the nonlinear one, as function of the uniform distributed load intensity.

This choice of variable names is chosen in order to have a straightforward comparison with the previous case.
Substituting these relation in equation (2.53) result and developing the terms it results the following equation

$$\widehat{EJ}\frac{\mathrm{d}^4 v_0}{\mathrm{d}x^4} - F_p\frac{\mathrm{d}^2 v_0}{\mathrm{d}x^2} = q\,, \tag{2.61}$$

and the boundary conditions

$$v_0(0) = 0 \quad , \quad \left.\frac{\mathrm{d}\,v_0}{\mathrm{d}x}\right|_0 = 0 \quad , \quad \widehat{EJ}\left.\frac{\mathrm{d}^2 v_0}{\mathrm{d}x^2}\right|_l = M \quad , \quad \widehat{EJ}\left.\frac{\mathrm{d}^3 v_0}{\mathrm{d}x^3}\right|_l - F_p\left.\frac{\mathrm{d}\,v_0}{\mathrm{d}x}\right|_l = -F_n\,. \tag{2.62}$$

The governing equation is equal to the one with following forces. The difference lies in the boundary conditions.
There is an important detail to notice: equation (2.61) results linear, but there is no linearization in the process w.r.t. the nonlinear strains. This means that the result takes fully into account the nonlinearity deriving from the large rotation of the system; there are still other nonlinearity not taken into account, but they derive from the hypotheses, and not the process.
The differences between the linear and nonlinear case (both without following forces) are shown in figure 2.18. This linear approximation behaves in analogy with the one of the following-force cases. The linear solution seem to diverge faster from the nonlinear one when the axial force is negative.

The case in which the endpoint forces are not taken into account can be simply derived imposing F_x and F_y null.
The governing equation results as

$$\widehat{EJ}\frac{\mathrm{d}^4 v_0}{\mathrm{d}x^4} = q\,, \tag{2.63}$$

and the boundary conditions as

$$v_0(0) = 0 \quad , \quad \left.\frac{\mathrm{d}\,v_0}{\mathrm{d}x}\right|_0 = 0 \quad , \quad \widehat{EJ}\left.\frac{\mathrm{d}^2 v_0}{\mathrm{d}x^2}\right|_l = M \quad , \quad \widehat{EJ}\left.\frac{\mathrm{d}^3 v_0}{\mathrm{d}x^3}\right|_l = 0\,. \tag{2.64}$$

In this case the following and non-following model coincide.
The comparison between linear and nonlinear formulations can be found simply in the $F_p = 0\,\mathrm{N}$ curves in the previous figure, e.g. 2.7, 2.9, 2.10.

2.2.4 Considerations on the MFC actuation

In all the previous linear and nonlinear calculations the MFC effect was considered equivalent to couples of bending moments and axial forces at the ends of the actuator.
This consideration derives from the VWP done in section 2.2.2. The main flaw of this process is the linearity assumption made in the MFC modelling, which caused an incongruence in the self-equilibrating nature of the problem when used on a nonlinear beam, as previously shown in figure 2.5.

In order to understand which assumption should be taken about the nature of the endpoint forces, a simple experimental setup is used.
A compliant structure made by unidirectional carbon fiber was equipped with an MFC. By measuring its endpoint deflection as function of the input voltage, a reference curve for the model choice can be obtained.

The measurements were done by actuating the MFC near a graph paper sheet, and marking the endpoint positions. Three sets of measures were done, and the average for each voltage was taken.
Table 2.1 contains the data used for the modelling.

characteristics	values
MFC type	M-8528-P1
plate material	unidirection carbon fiber
plate length	0.085 m
plate width	0.028 m
plate Young Modulus	3.4 GPa
plate height	$0.2718 \cdot 10^{-3}$m

Table 2.1: Experimental setup properties.

Figure 2.19 shows the results. It is evident how both the equations including the axial forces do not effectively model the actual system.
There is a reasonable similarity between the real case and the model not taking axial forces into account. The fact that this model resulted the most consistent with the experiment is consistent with its being the only self-equilibrated one.

The numerical simulations will be executed with these results in mind.

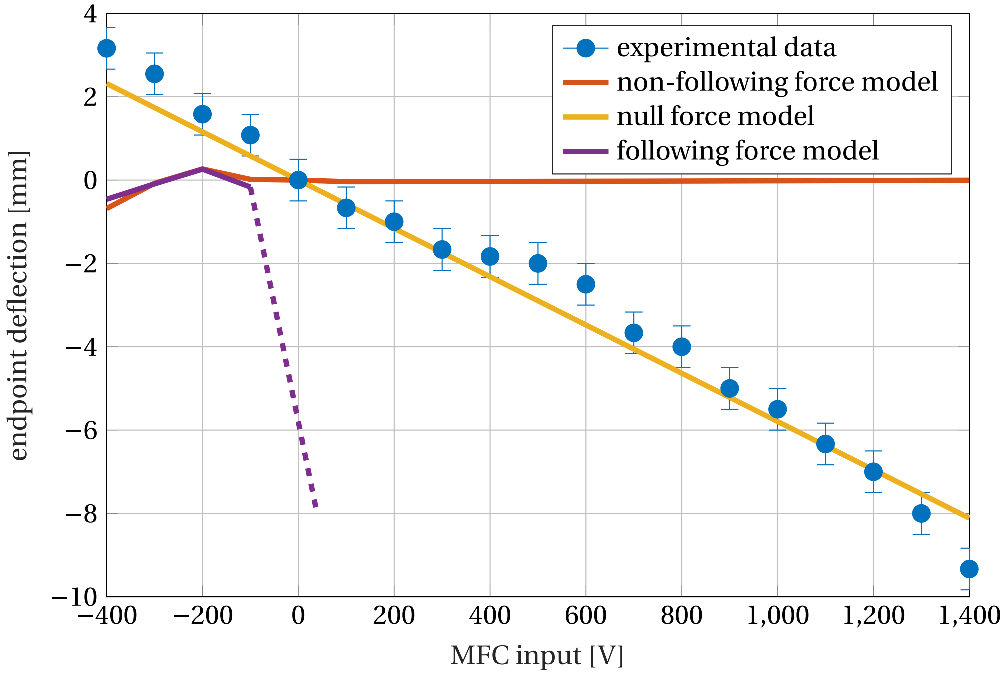

Figure 2.19: Comparison between the three possible axial force actuation models and the experimental values; the dashed line means lack of result convergence (values: $\sim 10^7$ mm).

2.3 Aerodynamic modelling

2.3.1 Overview

The aerodynamic model is a rather critical point, in which a particular care should be taken in order to judge which hypothesis holds and which not.
The most general model for a fluid dense enough to assume a continuum formulation rather than the collisional one are the compressible Navier-Stokes equations, i.e.

$$\begin{cases} \dfrac{\partial \rho}{\partial t} + \nabla \cdot \rho \mathbf{u} = 0\,, & \textbf{continuity}\,, \\ \dfrac{\partial \rho \mathbf{u}}{\partial t} + \nabla \cdot \left(\rho \mathbf{u} \otimes \mathbf{u} + P\mathbb{I} \right) - \nabla \cdot \mathbf{\Pi} = \mathbf{f}\,, & \textbf{momentum}\,, \\ \dfrac{\partial \rho e_t}{\partial t} + \nabla \cdot \left(\mathbf{u} \rho e_t + \mathbf{u} P \right) - \nabla \cdot (\mathbf{u} \cdot \mathbf{\Pi}) = \nabla \cdot \mathbf{q}\,, & \textbf{energy}\,. \end{cases} \tag{2.65}$$

The term $\mathbf{\Pi}$ is associated with the viscous stresses. If we assume that the fluid is Newtonian, which is well-justified for air, we can define it as:

$$\mathbf{\Pi} = \mu \left(\nabla \otimes \mathbf{u} + (\nabla \otimes \mathbf{u})^T \right) + \lambda \left(\nabla \cdot \mathbf{u} \right) \mathbb{I}\,. \tag{2.66}$$

For slow enough flows it is possible to assume their incompressibility. Notice that this passage is far from trivial: imposing divergence-free flow changes completely the meaning of the pressure term, making it thermodynamically meaningless, as well as energy equation. A thorough discussion of this assumption can be found in the book Fluidodinamica Comprimibile [28].

The incompressibility constraint results in the following equations:

$$\begin{cases} \dfrac{\partial \mathbf{u}}{\partial t} + \mathbf{u} \cdot \nabla \mathbf{u} + \dfrac{\nabla P}{\rho} - \nu \nabla^2 \mathbf{u} = \mathbf{f}\,, & \textbf{momentum}\,, \\ \nabla \cdot \mathbf{u} = 0\,, & \textbf{incompressibility}\,. \end{cases} \tag{2.67}$$

These are the well known incompressible Navier-Stokes equations.
The next hypothesis is a 2D domain. This implies that the velocity vector is always parallel to a plane and does not depend on the variable normal to that plane, coherently with the structural structural formulation used in the previous section.

For a slender aerodynamic body it is possible to hypothesise that all the viscous effect confined in the boundary layer of the body and in the wake. This means that the flow can be considered inviscid outside the region including the boundary layer and the wake.
Exploiting this hypothesis, along with the absence of volume forces **f** and steadyness (since the goal is to search for steady solutions), to simplify the incompressible Navier-Stokes system, the equations become:

$$\begin{cases} \mathbf{u} \cdot \nabla \mathbf{u} + \dfrac{\nabla P}{\rho} = \mathbf{0}\,, & \textbf{momentum}\,, \\ \nabla \cdot \mathbf{u} = 0\,, & \textbf{incompressibility}\,. \end{cases} \tag{2.68}$$

It is possible to take the curl of the momentum equation, and obtain

$$\nabla \times \left(\mathbf{u} \cdot \nabla \mathbf{u} + \frac{\nabla P}{\rho} = \mathbf{0} \right) \quad \Rightarrow \quad \nabla \times (\mathbf{u} \cdot \nabla \mathbf{u}) + \nabla \times \frac{\nabla P}{\rho} = \mathbf{0} \quad \Rightarrow \quad \nabla \times (\mathbf{u} \cdot \nabla \mathbf{u}) = \mathbf{0}\,. \tag{2.69}$$

The pressure term disappears since the curl of the gradient is null for every scalar field. This equation contains information only on the $\hat{z}$ axis (normal to the plane), thanks to the curl properties.

With some manipulations and the incompressibily hypothesis it is possible to obtain

$$\begin{cases} \mathbf{u} \cdot \nabla \, (\nabla \times \mathbf{u}) = 0\,, \\ \nabla \cdot \mathbf{u} = 0\,. \end{cases} \tag{2.70}$$

This last equation reveals that the momentum equation can be seen as a transport of vorticity ($\nabla \times \mathbf{u}$) along the streamlines. Assuming null vorticity at the boundary, the vorticity is null in the flow field:

$$\begin{cases} \nabla \times \mathbf{u} = 0\,, \\ \nabla \cdot \mathbf{u} = 0\,. \end{cases} \tag{2.71}$$

The 2D stream function is now defined:

$$\mathbf{u} = \begin{pmatrix} +\Psi,_y \\ -\Psi,_x \end{pmatrix} = \begin{pmatrix} 0 & 1 \\ -1 & 0 \end{pmatrix} \nabla \Psi = \nabla \Psi \times \hat{\mathbf{z}}\,, \tag{2.72}$$

The existence of a stream function implies the character of the flow field, compressibility of the flow prevents the existence of such a function, since

$$\nabla \cdot \mathbf{u} = \nabla \cdot \left(\begin{pmatrix} 0 & 1 \\ -1 & 0 \end{pmatrix} \nabla \Psi \right) = \frac{\partial^2 \Psi}{\partial x \partial y} - \frac{\partial^2 \Psi}{\partial y \partial x} \equiv 0\,. \tag{2.73}$$

The stream function is defined such that its isolines are aligned with the flow stream. This is easily shown by taking a streamline $y = Y(x)$ and a stream function definition such that it is evaluated along a specific streamline, i.e. $\tilde{\Psi}(x; Y(x)) = \Psi(x, Y(x))$. Its derivative is zero, when $Y(x)$ is an isoline:

$$\frac{\mathrm{d}\tilde{\Psi}}{\mathrm{d}x} = \frac{\partial \Psi}{\partial x} + \frac{\partial \Psi}{\partial y} \frac{\mathrm{d}Y}{\mathrm{d}x} = -v + u \frac{v}{u} = 0\,, \tag{2.74}$$

where $\mathbf{u} = (u,\ v)$ and the relation between the x-derivative of Y and the flow field components hold for a streamline.

This new definition makes the incompressibility constraint in the system (2.71) redundant, while the irrotationality becomes

$$\nabla \times \mathbf{u} = \nabla \times \left(\begin{pmatrix} 0 & 1 \\ -1 & 0 \end{pmatrix} \nabla \Psi \right) = -\frac{\partial^2 \Psi}{\partial x^2} - \frac{\partial^2 \Psi}{\partial y^2} = -\nabla^2 \Psi = 0\,, \tag{2.75}$$

leaving us with a system with the definition of the stream function and its harmonicity as governing equations for the flow field:

$$\begin{cases} \mathbf{u} = \begin{pmatrix} 0 & 1 \\ -1 & 0 \end{pmatrix} \nabla \Psi\,, \\ \nabla^2 \Psi = 0\,. \end{cases} \tag{2.76}$$

The key point is the linearity of the Laplace operator, thus the linearity of the governing equation. This ensures the validity of the superposition principle, and allows to decompose the complete solution in the sum of different elementary solutions. A complete treaty of the elementary solutions method can be found in Katz's and Plotkin's Low-Speed Aerodynamics book [18].

This method does not take into account the air viscosity, whose effect is confined in the airfoil boundary and along the wake.
There are different methods acting as correction to potential-flow solutions; a common correction is changing the apparent airfoil thickness to count the finite-thickness boundary layer. For a detail account of the boundary-layer theory, the reader is referred to the books by H. Schlichting and M. Van Dyke (e.g. [33]).

2.3.2 Chosen aerodynamic solver

XFoil was chosen as solver to compute the airflow around the airfoil. It is a very well known and tested steady panel method solver with integrated viscous and Mach corrections.

It computes the value of the inviscid stream function in the domain by placing a singularity sheet along the airfoil contour satisfying the no-penetration boundary conditions, superposed with the freestream function. A further source sheet is placed on both the airfoil contour and the wake. This is needed to compute the viscous quantities.
Denoting the airfoil surface by S_a, the wake by S_w and their union by S_t, such that $S_t = S_a \cup S_w$, the stream function has the following form in the domain:

$$\Psi(x, y) = \underbrace{u_\infty y - v_\infty x}_{\text{freestream}} + \underbrace{\frac{1}{2\pi}\int_{S_a} \gamma(s) \ln r(s; x, y)\, \mathrm{d}s}_{\text{vortex sheet}} + \underbrace{\frac{1}{2\pi}\int_{S_t} \sigma(s)\theta(s; x, y)\, \mathrm{d}s}_{\text{source sheet}}\,. \tag{2.77}$$

The singularity intensities are unknown, and finding them corresponds to solving the aerodynamic problem. The airfoil contour and the wake are discretised in panels. The vortex distribution varies linearly in each panel, while the source distribution is constant.

The discretised problem can be expressed in matrix form:

$$\begin{pmatrix} a_{11} & \cdots & a_{1N_a} \\ \vdots & \ddots & \vdots \\ a_{N_a 1} & \cdots & a_{N_a N_a} \end{pmatrix} \begin{pmatrix} \gamma_1 \\ \vdots \\ \gamma_{N_a} \end{pmatrix} = \Psi_0 - u_\infty \begin{pmatrix} y_1 \\ \vdots \\ y_{N_a} \end{pmatrix} + v_\infty \begin{pmatrix} x_1 \\ \vdots \\ x_{N_a} \end{pmatrix} - \begin{pmatrix} a_{11} & \cdots & \cdots & a_{1N_t} \\ \vdots & \ddots & \ddots & \vdots \\ a_{N_a 1} & \cdots & \cdots & a_{N_a N_t} \end{pmatrix} \begin{pmatrix} \sigma_1 \\ \vdots \\ \vdots \\ \sigma_{N_t} \end{pmatrix}, \quad (2.78)$$

where N_a is the number of panels on the airfoil, and N_t the number of points comprehending the wake.
More concisely we can write:

$$\mathbf{A}\bar{\boldsymbol{\gamma}} = \Psi_0 - u_\infty \bar{\mathbf{y}} + v_\infty \bar{\mathbf{x}} - \mathbf{B}\bar{\boldsymbol{\sigma}} \, , \quad (2.79)$$

where the overbar $\bar{a}$ indicates a discretised variable.
A and **B** are the influence coefficient matrices. They represent how the stream function at the i-th panel is influenced by the effect of the j-th one. The sources influence matrix is rectangular since the value is computed on the airfoil, but the sources appear also on the wake.

The Ψ_0 value is a constant. It appears since the airfoil contour is a streamline itself, and imposing a constant value to the stream function evaluated on it corresponds to imposing the no-penetration boundary condition. The simplicity in imposing the boundary conditions is the main reason the stream function is preferred over the potential in the XFoil code.

In a fully inviscid description the source sheet has no effect, and equation (2.78) - along with the Kutta condition - is enough to compute the whole field. To simulate a viscous behaviour, there is an implementation of the integral momentum and kinetic energy shape parameter equation. To compute the transition it is used a model for most-amplified Tollmien-Schlichting wave, known as e^n method.

A much more detailed description of XFoil routines and algorithms can be found at Drela's original XFoil publication [10].

2.4 Implementation

2.4.1 Code structure

In this section there will be a brief overview of the actual implementation of the aforementioned formulations. All the functions used to solve the problems formulated in the previous sections were written in MATLAB, except XFoil.

The code relies on the use of particular classes, as shown in table 2.2.

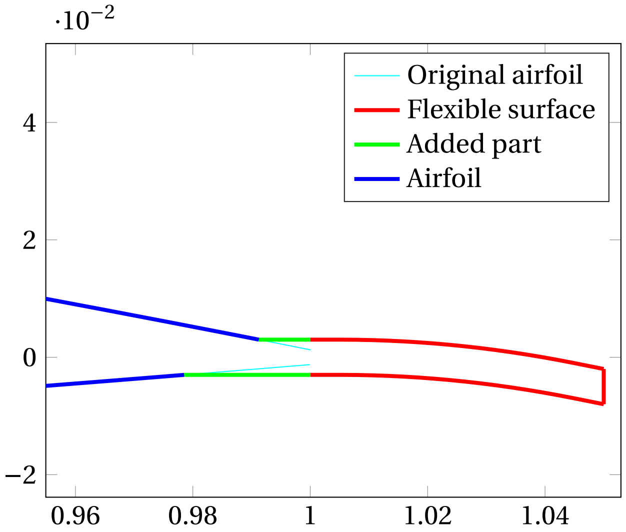

Figure 2.20: Zoom on the trailing edge of an airfoil with flexible plate thicker than the trailing edge. Notice the green part, necessary to avoid a sudden and unrealistic change of thickness.

class	stored information
airfoil	airfoil name and geometry in Selig format
airfoilmfckinematic	an airfoil-class variable, and six other fields with the geometric properties of the actuation surface
xfoilconditions	flight conditions parameters and running option for XFoil
mfcforces	mechanical properties of the actuator (e.g. $\widehat{EJ}$s and $\widehat{EA}$s) and forces applied by MFCs
airfoilmfcstatic	the objects of three classes, plus velocity and density, and a vector with the actuator deformation

Table 2.2: Classes defined and used in the MATLAB code.

Objects of class *airfoilmfckinematic* and *airfoilmfcstatic* store the properties of the complete airfoil and actuator configuration. The function *airfoil2num(•)* generates a $n \times 2$ matrix with x and y pairs when a Selig-format set of points is needed.

The user has no real control over the total number of points: while it is possible to decide the airfoil and actuator number of points separately, the generating function will add points if needed to avoid eventual panel length disuniformity in the intersection between the wing and the rear surface. This is clearly shown in figure 2.20.

The function *mfcstaticdefl* is particularly noteworthy, since it receives an object of class *airfoilmfcstatic* and the appropriate solving options, and it returns the actuator deformation and aerodynamic properties. It works by iteratively calculating XFoil solutions and deforming the trailing edge plate until a converged solution is reached. The plate deformation is under-relaxed to improve the iteration convergence. A more detailed pseudocode is shown in algorithm 2.1.

```
input  : ActAirfoil, toll, relax, rescale, iMax, method
output: ActAirfoil, deformation, pol, distr

initialization;
special treatment for $i = 1$;
while res < toll and $i$ <iMax do
    $i$++;
    relax ←setrelax($i$);
    Δcp ←computedeltacp(distr[$i$]);
    deformation[$i$] ← computedeformation(ActAirfoil, moment, axial, Δcp, method);
    ActAirfoil.deformation ←ActAirfoil.deformation · relax + deformation[$i$]· (1-relax);
    foilMat ← airfoil2num(ActAirfoil);
    pol[$i$], distr[$i$] ← xfoil(foilMat);
    initialization inner cycle;
    while xfoil does not converge do
        $j$++;
        redo the computation with relax rescaled by rescale;
    end
    res ← standard deviation of the last computed values of $c_L$;
    plot if requested;
end
```

Algorithm 2.1: Pseudocode of the convergence cycle for the actuator deformation.

Figure 2.21 shows a logical tree of the code hierarchy in the computation of the static deflection. All the elements are self explanatory, except for *kill time*: this is a parameter expressing how many seconds MATLAB should run XFoil before terminating it; this is necessary to avoid a dead lock in case of an XFoil crash, quite frequent unfortunately. The use of dedicated classes and such a system to compute the final result may be not the best choice as performance is concerned, but it makes the simulation setup and other numerical activities, such as exploring the parameter space, easier to the final user.

This choice is due to the fact that most of the computation time is taken by XFoil (and - in case of non-linear deflection with high forces - by the beam solver), making the overall impact of this architecture not particularly severe.

2.4.2 Implemented numerical methods

The actual implementation of the structural formulations presented in this chapter will be discussed here. The user must choose a formulation for the structural part when solving the coupled structural-aerodynamic problem. The linear beam model is implemented with a finite difference method and the nonlinear ones with a shooting method.
The finite difference scheme works as follows: the starting equation is the prestressed linear Euler-Bernoulli flexural equilibrium obtained in section 2.2.3.3, that for a Cantilever beam of length l with a distributed load and an endpoint moment M results as:

$$\widehat{EJ}\frac{\mathrm{d}^4 v_0}{\mathrm{d}x^4} - F_p\frac{\mathrm{d}^2 v_0}{\mathrm{d}x^2} = q\,, \tag{2.80}$$

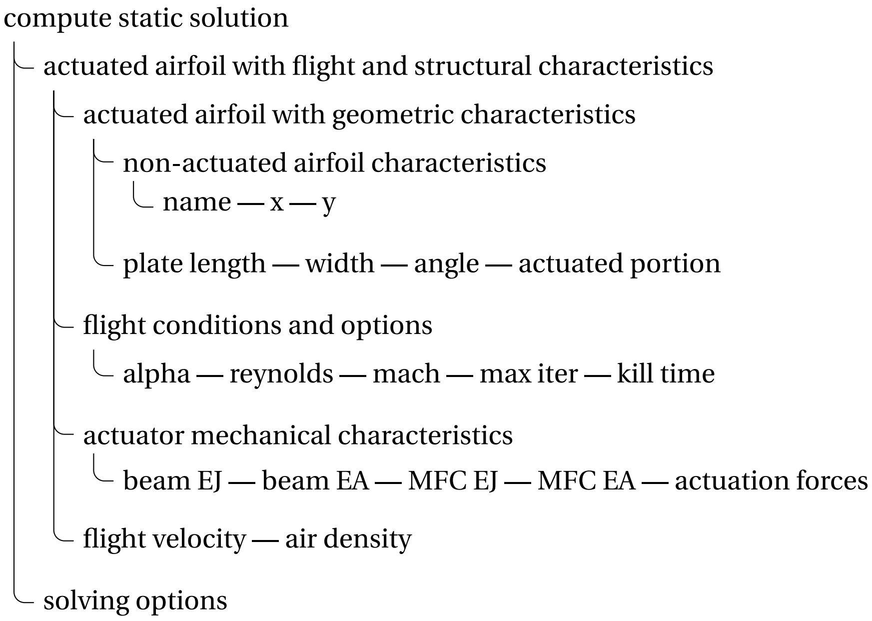

Figure 2.21: Scheme of the classes and functions hierarchy.

endowed with the following boundary conditions:

$$v_0(0) = 0 \quad , \qquad \left.\frac{\mathrm{d}v_0}{\mathrm{d}x}\right|_0 = 0 \quad , \qquad \widehat{EJ}\left.\frac{\mathrm{d}^2 v_0}{\mathrm{d}x^2}\right|_l = M \quad , \qquad \widehat{EJ}\left.\frac{\mathrm{d}^3 v_0}{\mathrm{d}x^3}\right|_l = 0\,. \tag{2.81}$$

It is interesting to notice that the implementation still has the axial force term, despite it was shown in section 2.2.4 that its effect is negligible. This is due the implementations generality. F_p should be . We can discretize v_0 along x evaluating it on N equally spaced points:

$$v_0 \xrightarrow{\mathrm{D}} \bar{\mathbf{v}}_0\,, \tag{2.82}$$

with the usual notation of the overline $\bar{\mathbf{a}}$ over a vector indicating the result of a discretisation, and the $\xrightarrow{\mathrm{D}}$ indicating the discretisation operator.
It is now possible to take a second-order central finite difference to compute an approximation of the needed derivatives:

$$\begin{aligned}
\left.\frac{\mathrm{d}^2 v_0}{\mathrm{d}x^2}\right|_{h\cdot n} &\xrightarrow{\mathrm{D}} \frac{\bar{\mathbf{v}}_{0,n-1} - 2\bar{\mathbf{v}}_{0,n} + \bar{\mathbf{v}}_{0,n+1}}{h^2}\,,\\
\left.\frac{\mathrm{d}^4 v_0}{\mathrm{d}x^4}\right|_{h\cdot n} &\xrightarrow{\mathrm{D}} \frac{\bar{\mathbf{v}}_{0,n-2} - 4\bar{\mathbf{v}}_{0,n-1} + 6\bar{\mathbf{v}}_{0,n} - 4\bar{\mathbf{v}}_{0,n+1} + \bar{\mathbf{v}}_{0,n+2}}{h^4}\,.
\end{aligned} \tag{2.83}$$

The boundary conditions can be discretised using backward and forward finite differences respectively for $x = 0$ and $x = L$:

$$\begin{aligned}
v_0(0) &\xrightarrow{\mathrm{D}} \bar{\mathbf{v}}_{0,1} = 0\,,\\
\left.\frac{\mathrm{d}v_0}{\mathrm{d}x}\right|_0 &\xrightarrow{\mathrm{D}} \frac{-\frac{3}{2}\bar{\mathbf{v}}_{0,1} + 2\bar{\mathbf{v}}_{0,2} - \frac{1}{2}\bar{\mathbf{v}}_{0,3}}{h} = 0\,,\\
\widehat{EJ}\left.\frac{\mathrm{d}^2 v_0}{\mathrm{d}x^2}\right|_L &\xrightarrow{\mathrm{D}} \frac{2\bar{\mathbf{v}}_{0,N} - 5\bar{\mathbf{v}}_{0,N-1} + 4\bar{\mathbf{v}}_{0,N-2} - \bar{\mathbf{v}}_{0,N-3}}{h^2} = M\,,\\
\widehat{EJ}\left.\frac{\mathrm{d}^3 v_0}{\mathrm{d}x^3}\right|_L &\xrightarrow{\mathrm{D}} \frac{\frac{5}{2}\bar{\mathbf{v}}_{0,N} - 9\bar{\mathbf{v}}_{0,N-1} + 12\bar{\mathbf{v}}_{0,N-2} - 7\bar{\mathbf{v}}_{0,N-3} + \frac{3}{2}\bar{\mathbf{v}}_{0,N-4}}{h^3} = 0\,.
\end{aligned} \tag{2.84}$$

The result is that the problem is now an easily solvable sparse linear system.
The finite difference coefficient can be arranged in matrix form as follows:

$$\mathbf{A} = \frac{\widehat{EJ}}{h^4}\begin{pmatrix} 1 & & & & & & & & \\ -\frac{3}{2} & 2 & -\frac{1}{2} & & & & & & \\ 1 & -4 & 6 & -4 & 1 & & & & \\ & 1 & -4 & 6 & -4 & 1 & & & \\ & & & & \ddots & & & & \\ & & & 1 & -4 & 6 & -4 & 1 & \\ & & & & 1 & -4 & 6 & -4 & 1 \\ & & & & & -1 & 4 & -5 & 2 \\ & & & & \frac{3}{2} & -7 & 12 & -9 & \frac{5}{2} \end{pmatrix} - \frac{\widehat{EA}}{h^2}\begin{pmatrix} & & & & & & \\ & & & & & & \\ 1 & -2 & 1 & & & & \\ & 1 & -2 & 1 & & & \\ & & & \ddots & & & \\ & & & 1 & -2 & 1 & \\ & & & & 1 & -2 & 1 \\ & & & & & & \\ & & & & & & \end{pmatrix}, \tag{2.85}$$

and the RHS term becomes

$$\bar{\mathbf{q}} = \begin{pmatrix} 0 \\ 0 \\ \bar{q}_3 \\ \bar{q}_4 \\ \vdots \\ \bar{q}_{N-3} \\ \bar{q}_{N-2} \\ M/h^2 \\ 0 \end{pmatrix}, \tag{2.86}$$

where the torque term is divided by h^2 because in $\mathbf{A}$ the corresponding row is itself divided by h^2.
The deformation is obtained by solving the linear system

$$\bar{\mathbf{v}}_0 = \mathbf{A}^{-1}\bar{\mathbf{q}} \tag{2.87}$$

by MATLAB linear equations solver.

If the MFC does not cover the whole surface, the system becomes more involved. The transition zones between the MFC-equipped part and the non-actuated one can be modelled by interface conditions similar to the boundary conditions in the first and last rows of the former linear system.

The representation of the problem in equation (2.29) allows us to solve it with the shooting method. This means that the problem is treated as an initial-value problem by guessing the initial conditions, namely the missing conditions in the first end of the beam, so that the solution matches the actual boundary conditions in the second extreme of the beam. An iteration is set up to correct the guessed initial values and converge to the solution of the boundary value problem.

We can define two vectors: $\boldsymbol{\Upsilon}$, containing the variables satisfying conditions in the first extreme, and $\boldsymbol{\Psi}$, containing the one with final boundary conditions:

$$\begin{aligned} \boldsymbol{\Upsilon} &= \begin{pmatrix} x & y & \theta \end{pmatrix}, \\ \boldsymbol{\Psi} &= \begin{pmatrix} \varphi & \xi & \Pi_x & \Pi_y & \Gamma & \Sigma \end{pmatrix}, \end{aligned} \tag{2.88}$$

and represent the RHS of the system in equation (2.29) with the vector functions $\mathbf{F}(s, \boldsymbol{\Upsilon}, \boldsymbol{\Psi})$ and $\mathbf{G}(s, \boldsymbol{\Upsilon}, \boldsymbol{\Psi})$. Our problem becomes:

$$\begin{cases} \dfrac{\mathrm{d}\boldsymbol{\Upsilon}(s)}{\mathrm{d}s} = \mathbf{F}(s, \boldsymbol{\Upsilon}, \boldsymbol{\Psi}), \\ \dfrac{\mathrm{d}\boldsymbol{\Psi}(s)}{\mathrm{d}s} = \mathbf{G}(s, \boldsymbol{\Upsilon}, \boldsymbol{\Psi}), \\ \boldsymbol{\Upsilon}(0) = \overline{\boldsymbol{\Upsilon}}, \\ \boldsymbol{\Psi}(L) = \overline{\boldsymbol{\Psi}}\left(\boldsymbol{\Upsilon}(L)\right), \end{cases} \tag{2.89}$$

where in our case $\overline{\boldsymbol{\Upsilon}}$ is a vector of zeros, and $\overline{\boldsymbol{\Psi}}$ has two elements depending on $\theta(L)$, thus being function of $\boldsymbol{\Upsilon}(L)$.
It is possible to define a particular function such that:

$$\mathbf{H}\left(\mathbf{X};\overline{\boldsymbol{\Upsilon}},\overline{\boldsymbol{\Psi}}\right) = \quad \boldsymbol{\Psi}(L) - \overline{\boldsymbol{\Psi}}\left(\boldsymbol{\Upsilon}(L)\right) \quad s.t. \begin{cases} \frac{\mathrm{d}\boldsymbol{\Upsilon}(s)}{\mathrm{d}s} = \mathbf{F}(s,\boldsymbol{\Upsilon},\boldsymbol{\Psi})\,, \\ \frac{\mathrm{d}\boldsymbol{\Psi}(s)}{\mathrm{d}s} = \mathbf{G}(s,\boldsymbol{\Upsilon},\boldsymbol{\Psi})\,, \\ \boldsymbol{\Upsilon}(0) = \overline{\boldsymbol{\Upsilon}}\,, \\ \boldsymbol{\Psi}(0) = \mathbf{X}\,. \end{cases} \tag{2.90}$$

The solving method can now be described more formally as:

$$\begin{cases} \mathbf{H}\left(\mathbf{X};\overline{\boldsymbol{\Upsilon}},\overline{\boldsymbol{\Psi}}\right) = 0\,, \\ \dfrac{\mathrm{d}\boldsymbol{\Upsilon}(s)}{\mathrm{d}s} = \mathbf{F}(s,\boldsymbol{\Upsilon},\boldsymbol{\Psi})\,, \\ \dfrac{\mathrm{d}\boldsymbol{\Psi}(s)}{\mathrm{d}s} = \mathbf{G}(s,\boldsymbol{\Upsilon},\boldsymbol{\Psi})\,, \\ \boldsymbol{\Upsilon}(0) = \overline{\boldsymbol{\Upsilon}}\,, \\ \boldsymbol{\Psi}(0) = \mathbf{X}\,. \end{cases} \tag{2.91}$$

This is now an initial value problem, coupled with an additional equation.
The MATLAB implementation uses the integrated function `ode45` (or other ODE solver if needed) and `fsolve` as shown in algorithm 2.2.

```
input  : $M$, $F$, $N$, $\widehat{EJ}$, $L$, $P$
output: trueSol
initialization;
guessBC ← $[M/\widehat{EJ} + FL/\widehat{EJ} + WL^2/(2\widehat{EJ}),\ -F/\widehat{EJ} - WL/\widehat{EJ},\ 0,\ WL,\ 1,\ 0]$;
trueBC ← fsolve(@(BC)funtomin(BC, $M$, $F$, $N$, $\widehat{EJ}$, $L$, $P$), guessBC, options);
trueSol ← ode45(@(s,y) funtoint($s$, $y$, $F$, $N$, $\widehat{EJ}$, $P$), [0, $L$], [0,0,0, trueBC ]);
function out = funtomin(BC, $M$, $F$, $N$, $\widehat{EJ}$, $L$, $P$)
    sol ← ode45(@(s,y) funtoint($s$, $y$, $F$, $N$, $\widehat{EJ}$, $P$), [0, $L$], [0,0,0, BC ]);
    /* sol is a structure, field y contains the integration results, with
       the different variables ar rows                                  */
    out[1] ← sol.y (4, end) - $M/EJ$;
    out[2] ← sol.y (5, end) + $F/EJ$;
    out[3] ← sol.y (6, end);
    out[4] ← sol.y (7, end);
    out[5] ← sol.y (8, end) - cos(sol.y (3, end));
    out[6] ← sol.y (9, end) - sin(sol.y (3, end));
end
function out = funtoint($s$, $y$, $F$, $N$, $\widehat{EJ}$, $P$)
    mathematical description of the integrand functions;
end
```

Algorithm 2.2: Nonlinear deformation solver pseudocode.

The values for the starting guess are defined as

$$\begin{cases} \varphi(0) = \dfrac{M}{\widehat{EJ}} + \dfrac{F_y\, l}{\widehat{EJ}} + \dfrac{\mathbb{P}_1}{\widehat{EJ}}\,, \\ \xi(0) = -\dfrac{F_y}{\widehat{EJ}} - \dfrac{\mathbb{P}_0}{\widehat{EJ}}\,, \\ \Pi_x(0) = 0\,, \\ \Pi_y(0) = \mathbb{P}_0\,, \\ \Gamma(0) = 1\,, \\ \Sigma(0) = 0\,, \end{cases} \tag{2.92}$$

where F_y is the endpoint normal force, M the endpoint moment, $P(x)$ the distributed load, and

$$\mathbb{P}_0 = \int_0^l P(x)\,\mathrm{d}x \quad , \qquad \mathbb{P}_1 = \int_0^l P(x)\,x\,\mathrm{d}x\,. \tag{2.93}$$

This method is significantly slower than the linear one, especially when subjected to a high tractions.

Chapter three

Numerical results

3.1 Uncoupled formulation

3.1.1 Introduction and general behaviour

The first computations are characterized by the lack of aeroelastic static coupling: in other words the shape of the deformed plate was assumed irrespective of the aerodynamic loads. The aim is to isolate the effects of MFC actuation from the aeroelastic effects. This allows one to understand more deeply the overall actuation behaviour and provide an optimistic reference for the static aeroelastic calculations. The developed code allows one to ignore the two-way coupling by simply setting the maximum number of iterations in the coupling cycle to one. Figure 3.1 provides a very simple scheme showing the procedure. Table 3.1 shows the default configuration. All the computations have been done varying one or two parameters, and leaving unchanged the other ones.

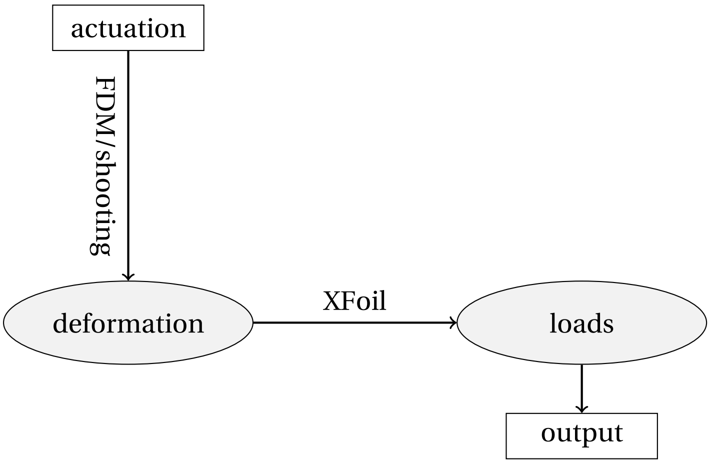

Figure 3.1: Simple scheme of the uncoupled computations.

parameter	value	parameter	value
airfoil	NACA 0012	**MFC plate coverage**	100%
airfoil points	100	**MFC Young modulus**	30 GPa
plate thickness	$0.3 \cdot 10^{-3}$ m	**MFCs per spanwise meter**	5
plate length	$0.1 \cdot 10^{0}$ m	**MFC forces range**	$-308 \div 308$ N
plate angle	0	**angle of attack**	0
plate Young modulus	20 GPa	**Reynolds number**	inviscid
plate points	30	**Mach number**	0
MFC thickness	$0.3 \cdot 10^{-3}$ m	**max XFoil iterations**	150
MFC width	$0.64 \cdot 10^{-1}$ m	**XFoil kill time**	3 s

Table 3.1: System properties used in the simulation.

As previously stated, the solved problem is 2D. The parameters intrinsically related to the problem three-dimensionality (e.g. the number of MFCs per spanwise unit length) are used in the homogeneisation procedure explained in section 2.2.1. The MFC properties are given by Smart Material Corp.'s datasheet, the employed values of the forces are those provided by the M-8557-P1 model, when symmetrically operating the upper and lower side, i.e. in a $-500 \div 500$ V range.

A first aim is to investigate if a linear beam deformation produces a linear change of the C_L. The linearity can be appreciated by considering the magnitude of the ratio between the second order and first order terms in a quadratic fit of the C_L variation. This value will give an insight of the effect that a higher order approximation would have with respect to a linear one. Exploring part of the parameter space as specified in table 3.2 reveals that the magnitude of such ratio is always less than 10^{-5}. Excluding computations for a low plate length, i.e. less than 0.04 m, the ratio decreases by an additional order of magnitude.
Figure 3.2 shows the ratio values enveloped with respect to the plate thickness, varying the length.

parameter	minimum value	maximum value	steps
MFC force	-308 N	308 N	11
plate thickness	$6 \cdot 10^{-5}$ m	$4 \cdot 10^{-4}$ m	5
plate length	$1 \cdot 10^{-2}$ m	$2 \cdot 10^{-1}$ m	10

Table 3.2: Values of the parameters used in the validation of the linear beam model; table 3.1 provides the values of all the other parameters.

The linear behaviour of the C_L with respect to the actuation force allows us to describe the actuation effectiveness by the following parameter:

$$C_{L,F} \overset{\text{def}}{=} \frac{\partial C_L(\dots, F)}{\partial F}, \tag{3.1}$$

where F is the mean actuation force applied by the upper and lower actuators, having the opposite positive direction (the upper actuator force is considered positive when extending, the lower one when compressing). The force has been preferred to the voltage to avoid any dependence on the MFC model, and to the torque to avoid dependence on the thickness, which is part of the parameter space.

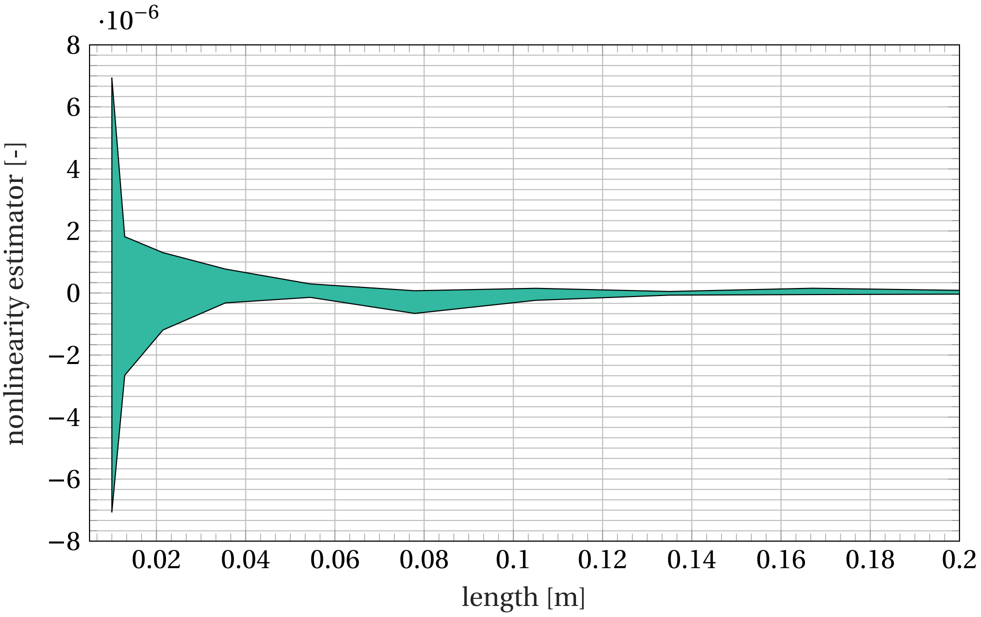

Figure 3.2: Envelope of the values of the nonlinearity estimator for different thicknesses as a function of the length; it is defined as the ratio between the second and the first order term in a second order polynomial data fit.

The second step is to compare linear and nonlinear results. The linear model appears to be a good approximation of the nonlinear one. Figure 3.3 visually shows the result similarities, while figure 3.4 reveals the error varying the length, for different thicknesses.

The $C_{L,F}$ definition allows us to describe the actuation effectiveness by a scalar value. This value is influenced by both the structural and the aerodynamic properties of the system.
The next step is to compute the $C_{L,F}$ by exploring the parameter space.
Notice that the computed C_L and the other nondimensional parameters are normalized with respect to the airfoil chord, not considering the rear plate. This allows one to refer to the same airfoil chord when varying the actuator length.

3.1.2 Effect of the structure parameters

The first analysis is the dependence of $C_{L,F}$ on the geometry of the rear plate (i.e. its length and thickness). The simulation parameters are specified in table 3.1, except for the two parameters that are varied as specified in table 3.3.

parameter	minimum value	maximum value	steps
plate thickness	$6 \cdot 10^{-5}$ m	$4 \cdot 10^{-4}$ m	20
plate length	$1 \cdot 10^{-2}$ m	$2 \cdot 10^{-1}$ m	20

Table 3.3: Parameters varied for in first analysis; this data will allow to model the $C_{L,F}$ as function of l and t.

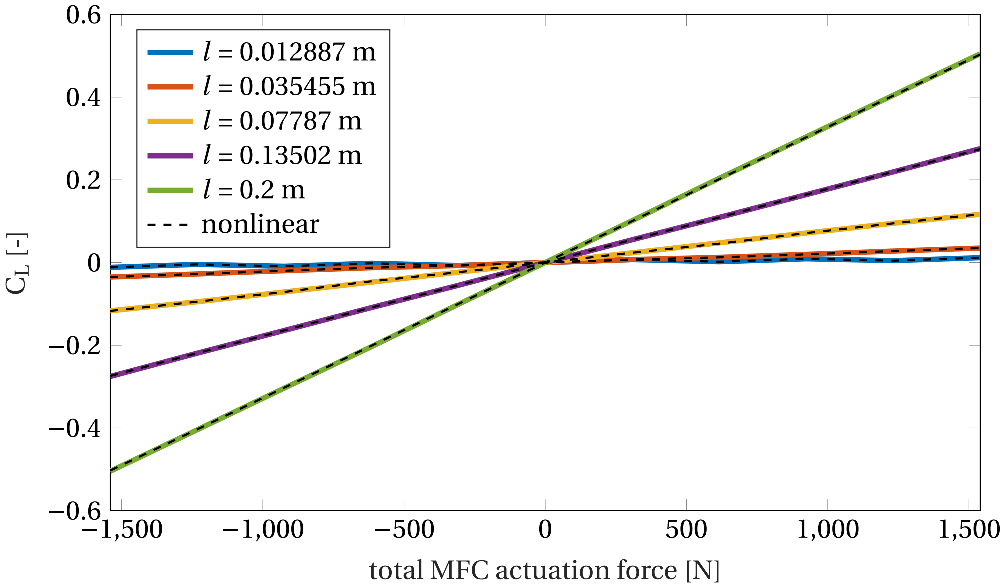

Figure 3.3: Lift coefficient as a function of the actuation force for several actuator lengths computed by both the linear and the nonlinear model; the key in the figure does not show the length for each nonlinear result since they are almost overlapped to the corresponding linear results.

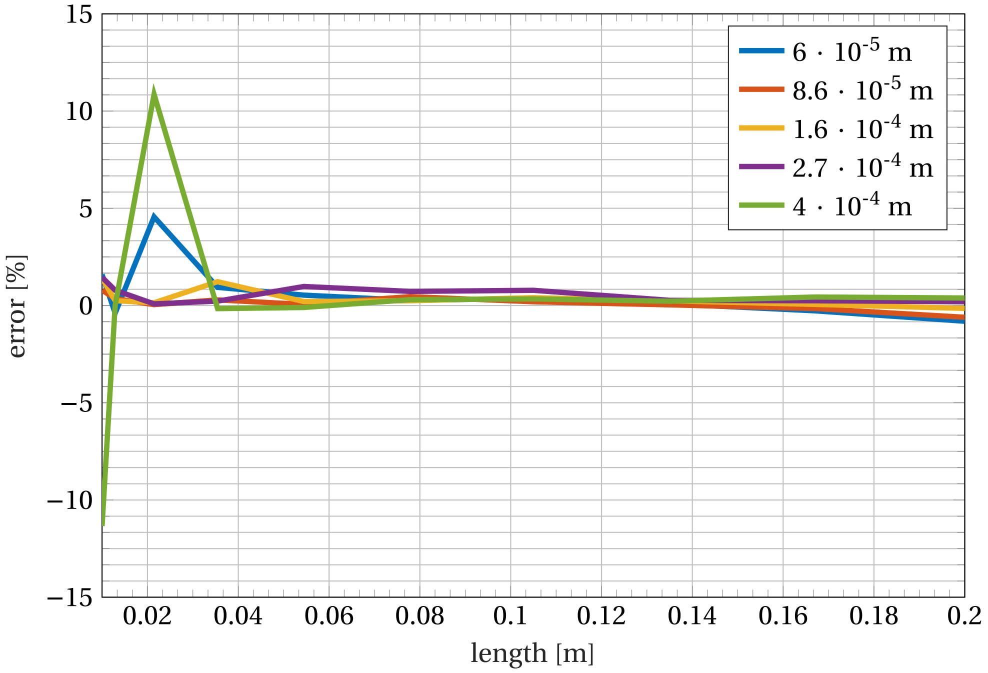

Figure 3.4: Nondimensional difference between the linear and nonlinear results as a function of the actuator length for several plate thicknesses. From $l = 0.04\,\text{m}$ up to $l = 0.2\,\text{m}$ the difference is less than 3%.

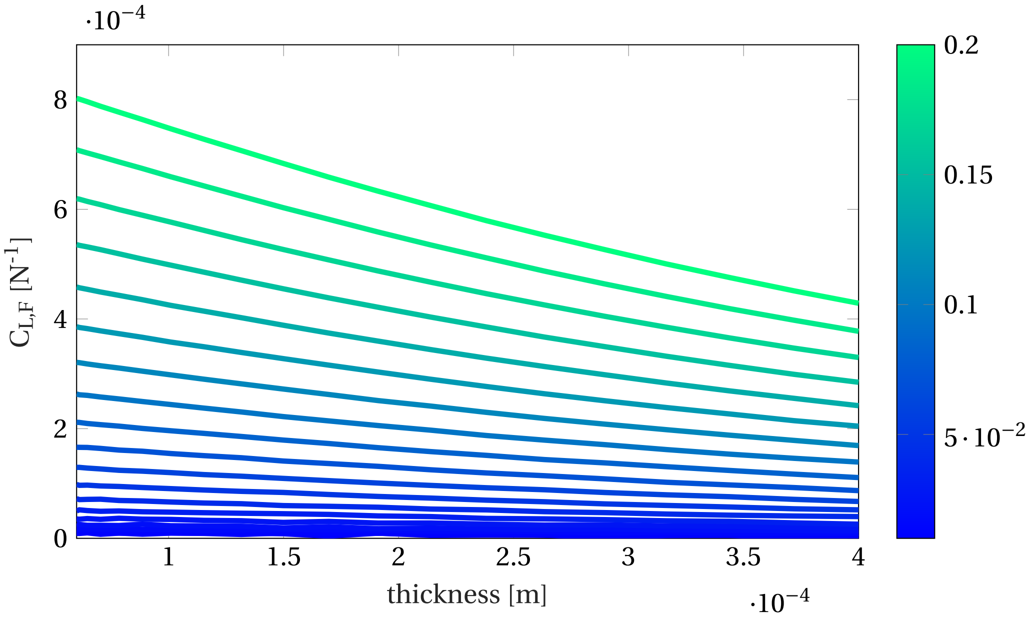

Figure 3.5: $C_{L,F}$ plotted as a function of the plate thickness for several plate lengths.

The computation leads to the results shown in figure 3.5 and 3.6. The $C_{L,F}$ increases superlinearly with the plate length. A thickness increment instead causes a $C_{L,F}$ decrease: this is due to the torque increasing only linearly with the thickness, while the flexural stiffness increases with its third power.

The $l - C_{L,F}$ graph has a very simple shape when plotted in logarithmic-scale axes (figure 3.7). As a matter of fact, the curves with different thicknesses - with a sufficient length - are parallel and straight. This means that they all follow a power-law with the same exponent and different multiplicative terms. Defining $\tilde{C}_{L,F}$ as the, approximate, scaling law for $C_{L,F}$, such a scaling law reads:

$$\tilde{C}_{L,F}(t,l) = K_{12}(t)\, l^{K_3}\,. \tag{3.2}$$

A least-square, first-order fit to this curves, excluding the first 7 points, owing to the presence of high oscillations, yields a set of Y-intercepts and slopes.
The slope has a mean value of 1.5239 and a standard deviation of 0.0039: it is not sensibly varying. The intercept instead vary linearly with the thickness (figure 3.8). A least-square, first-order fit of this term allows one to express it as linear function of the thickness, namely

$$K_{12}(t) = K_1 + K_2\, t\,. \tag{3.3}$$

The $C_{L,F}(t)$, reported in figure 3.5 on a linear scale, can be plotted in semi-logarithmic scale to unveil its scaling law with respect to the plate thickness (figure 3.9). The straight lines observed in figure 3.9 show that the scaling law is exponential. Now it is possible to completely define the $\tilde{C}_{L,F}(t,l)$ as a semi-empirical approximation of the complete scaling law $C_{L,F}(\dots,t,l)$:

$$\left.\begin{aligned} \ln\left(\tilde{C}_{L,F}(l,t)\right) &= K_{12}(t) + K_3 \ln l \\ K_{12}(t) &= K_1 + K_2\, t \end{aligned}\right\} \Rightarrow \ln\left(\tilde{C}_{L,F}(l,t)\right) = K_1 + K_2\, t + K_3 \ln l \Rightarrow \tilde{C}_{L,F}(l,t) = e^{K_1 + K_2\, t}\, l^{K_3}\,, \tag{3.4}$$

where K_1, K_2, and K_3 have the following values:

$$\begin{aligned} K_1 &= -4.564\,, \\ K_2 &= -1.852 \cdot 10^3\,, \\ K_3 &= 1.524\,. \end{aligned} \tag{3.5}$$

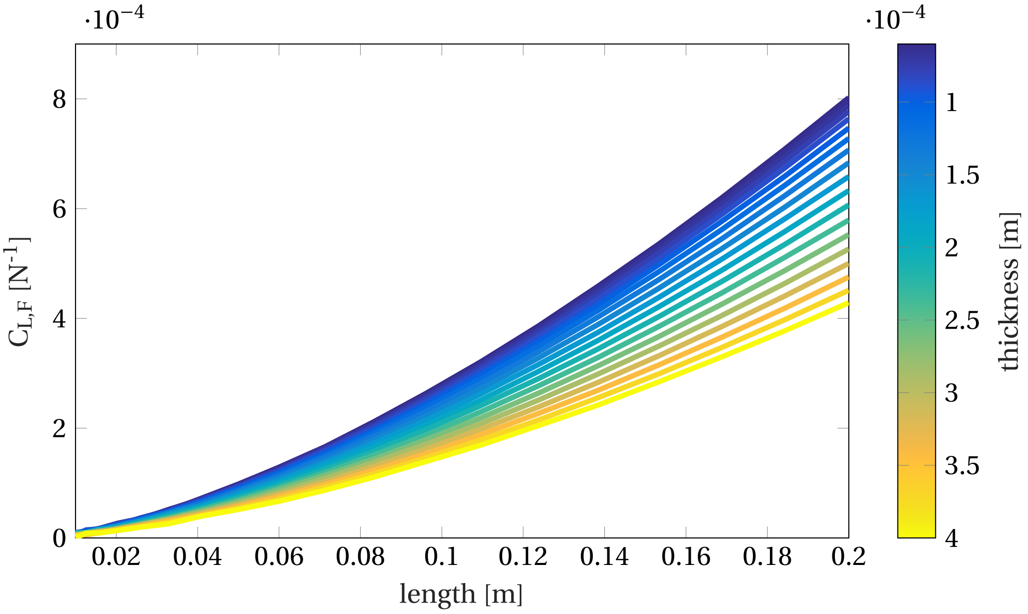

Figure 3.6: $C_{L,F}$ plotted as a function of the plate length for several plate thicknesses.

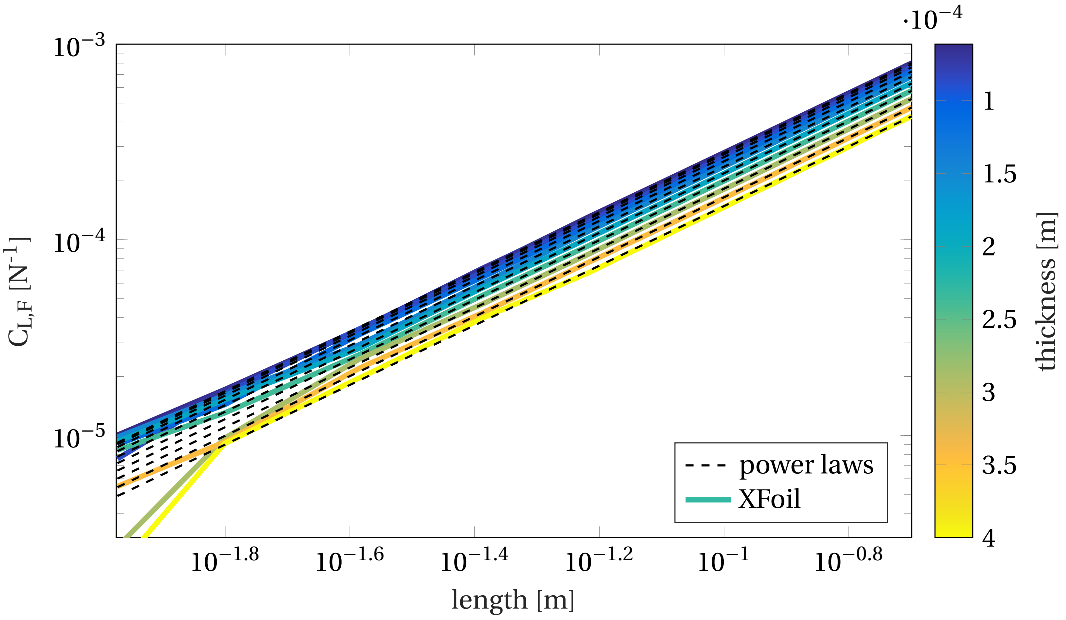

Figure 3.7: $C_{L,F}$ plotted as a function of the plate length for several plate thicknesses, with logarithmic axes; the dashed lines are power-law fits.

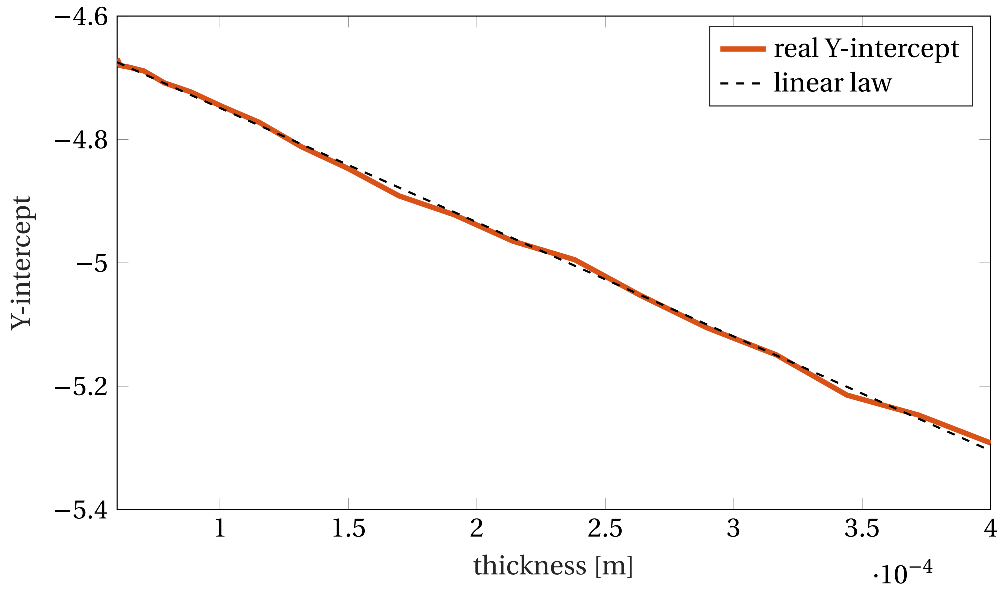

Figure 3.8: Values of the Y-intercept of a linear fit of $\log C_{L,F}$ over $\log l$, compared with a linear law.

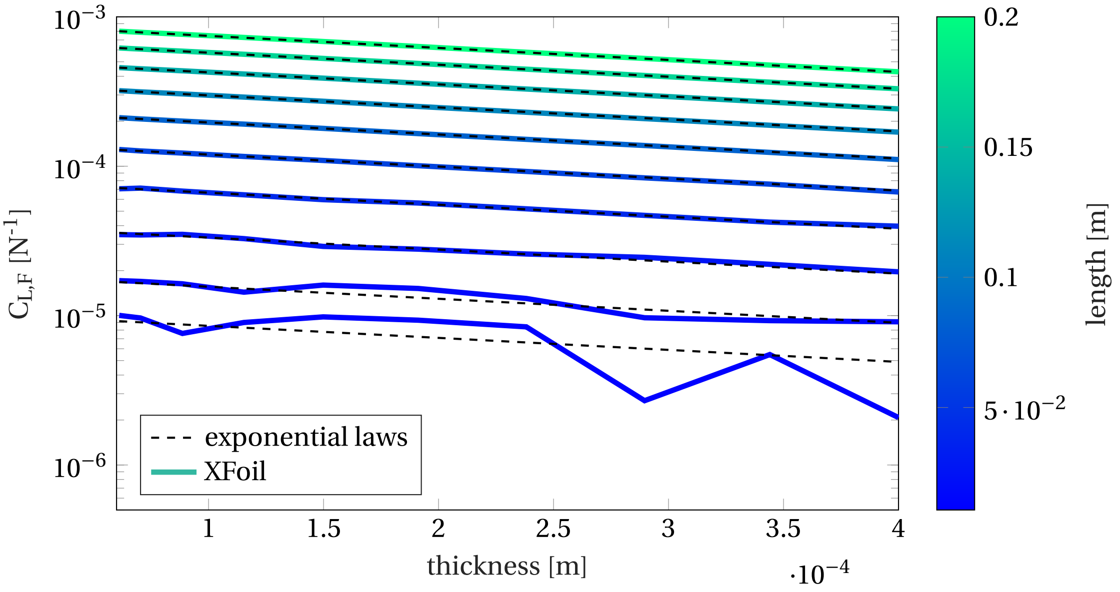

Figure 3.9: $C_{L,F}$ plotted as a function of the plate thickness for several plate lengths, with semilogarithmic axes; the dashed lines are exponential fits.

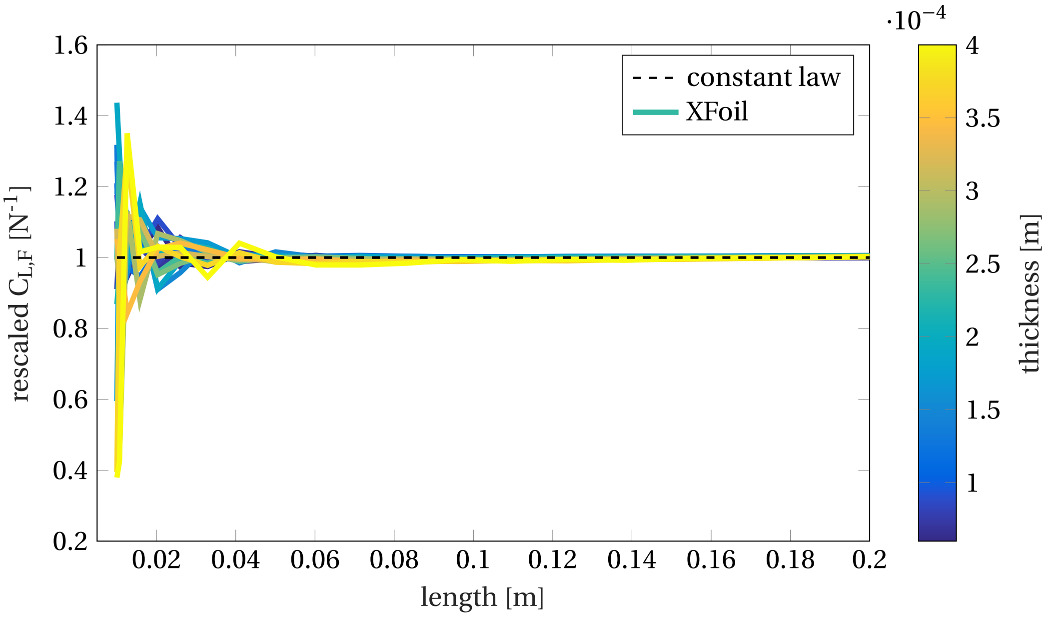

Figure 3.10: Ratio between numerical results and $\tilde{C}_{L,F}$ as function of l for several values of t; the closer the curve to the constant law, the more accurate the proposed scaling law.

Notice that the terms used are dimensional. Formally - being the solution computed with a panel method with an endpoint-loaded linear beam - the absolute beam length and thickness are not important, but it is their ratio with the airfoil length. This should be taken in mind when manipulating equation (3.4), that presents l and t implying their nondimensionality.

Figure 3.10 shows the ratio between the computed $C_{L,F}$ and the value predicted by the approximate scaling law $\tilde{C}_{L,F}$. The values tend to collapse on the constant value of 1 for sufficiently long plates, indicating the accuracy of the scaling law.

We can express the error as:

$$err = \frac{\tilde{C}_{L,F} - C_{L,F}}{C_{L,F}}\,. \tag{3.6}$$

Figure 3.11 shows the envelope of the errors as a function of the plate length. The proposed scaling law seems sufficiently accurate. The existence itself of such a simple scaling law for trailing edge actuation in an inviscid simulation is an interesting fact, even if the constants may be a function of the system properties.

These results are valid for a given Young modulus. This means that the constants could actually depend on E; thus a more complete formula should be written as:

$$\tilde{C}_{L,F}(l,t,E) = K_1(E)\, e^{K_2(E)\,t}\, l^{K_3(E)}\,. \tag{3.7}$$

A very similar scaling law for the $C_{L,F}$ as a function of the Young modulus E instead of the thickness t can be derived. The parameters varied in investigating it are reported in table 3.4.

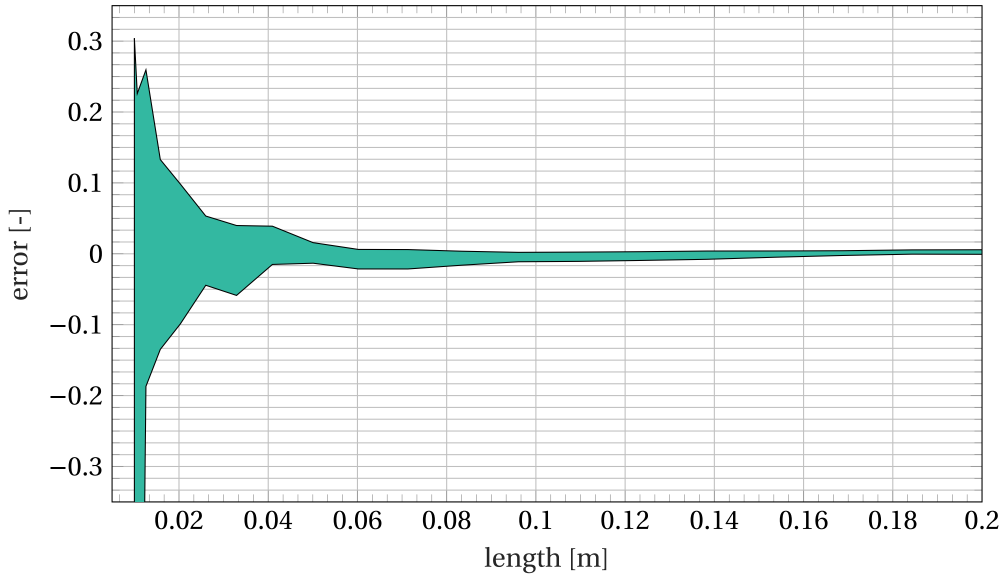

Figure 3.11: Envelope of the algebraic model errors.

parameter	minimum value	maximum value	steps
plate length	$0.1 \cdot 10^{-1}$ m	0.2 m	20
plate Young modulus	$0.1 \cdot 10^{10}$ Pa	$0.7 \cdot 10^{11}$ Pa	20

Table 3.4: Parameters varied to compute the plate Young modulus and length interdependence.

The results are not shown since they are very similar to those reported in figure 3.6 and 3.5 for the $C_{L,F}$; also in this case, therefore, the scaling law can be approximated as:

$$\tilde{C}_{L,F}(l,E) = e^{K_4+K_5E}\, l^{K_6}\,. \tag{3.8}$$

What does change with respect to the $l-t$ case are the constants of the resulting equation, in fact

$$\begin{aligned} K_4 &= -5.044\,,\\ K_5 &= -3.649\cdot 10^{-12}\,,\\ K_6 &= 1.525\,. \end{aligned} \tag{3.9}$$

This results are valid for a given thickness, thus

$$\tilde{C}_{L,F}(l,E,t) = e^{K_4(t)+K_5(t)E}\, l^{K_6(t)}\,. \tag{3.10}$$

It is very interesting to notice that $K_6 \approx K_3$, and that K_6 does not vary with E, such asK_3 does not vary with t; therefore we can assume that $K_3 = K_6 = K_l$ is neither a function of t or E.

The scaling laws reported in (3.7) and (3.10) can be seen as sections of a function of three variables, evaluated at a given $E = \overline{E}$ and $t = \overline{t}$, respectively. This means that the dependence of the constant on the evaluated parameter can only be linear, otherwise the two formulations could not “overlap”, namely

$$\begin{cases} K_1 = K_{1m}\overline{E} + K_{1q}\,, \\ K_2 = K_{2m}\overline{E} + K_{2q}\,, \\ K_4 = K_{4m}\overline{t} + K_{4q}\,, \\ K_5 = K_{5m}\overline{t} + K_{5q}\,. \end{cases} \tag{3.11}$$

The equality between the two $\tilde{C}_{L,F}$ yields:

$$\begin{aligned} &\left.\begin{aligned} \tilde{C}_{L,F}(l,\overline{t};\overline{E}) &= e^{K_1(\overline{E})+K_2(\overline{E})\overline{t}}\, l^{K_3} \\ \tilde{C}_{L,F}(l,\overline{E};\overline{t}) &= e^{K_4(\overline{t})+K_5(\overline{t})\overline{E}}\, l^{K_3} \end{aligned}\right\} \Rightarrow K_1(\overline{E}) + K_2(\overline{E})\overline{t} = K_4(\overline{t}) + K_5(\overline{t})\overline{E} \\ &\Rightarrow K_{1m}\overline{E} + K_{1q} + \left(K_{2m}\overline{E} + K_{2q}\right)\overline{t} = K_{4m}\overline{t} + K_{4q} + \left(K_{5m}\overline{t} + K_{5q}\right)\overline{E} \\ &\Rightarrow K_{1q} + K_{1m}\overline{E} + K_{2q}\overline{t} + K_{2m}\overline{E}\,\overline{t} = K_{4q} + K_{5q}\overline{E} + K_{4m}\overline{t} + K_{5m}\overline{E}\,\overline{t}\,. \end{aligned} \tag{3.12}$$

Equation (3.12) implies:

$$\begin{cases} K_{1q} = K_{4q}\,, \\ K_{1m} = K_{5q}\,, \\ K_{2q} = K_{4m}\,, \\ K_{2m} = K_{5m}\,. \end{cases} \tag{3.13}$$

Equation (3.11) and equation (3.13) together form a singular 8 × 8 system. It is therefore necessary to replace one row. To find the missing equation one can consider that, when the beam has a null thickness, its Young Modulus should not affect the deformation. Notice that the beam will still have non-null stiffness when the plate thickness goes to zero by virtue of the stiffness of the MFC actuators. Then:

$$\tilde{C}_{L,F}(l,0,E) = e^{K_{1q}+K_{1m}E+K_{2q}0+K_{2m}E0}\, l^{K_l} \Rightarrow K_{1m} = 0\,. \tag{3.14}$$

Substituting this last equation in the system, it becomes:

$$\begin{pmatrix} 1 & \overline{E} & 0 & 0 & 0 & 0 & 0 & 0 \\ 0 & 0 & 0 & 0 & 1 & \overline{t} & 0 & 0 \\ 0 & 0 & 1 & \overline{E} & 0 & 0 & 0 & 0 \\ 0 & 0 & 0 & 0 & 0 & 0 & 1 & \overline{t} \\ 1 & 0 & 0 & 0 & -1 & 0 & 0 & 0 \\ 0 & 1 & 0 & 0 & 0 & 0 & -1 & 0 \\ 0 & 0 & -1 & 0 & 0 & 1 & 0 & 0 \\ 0 & 1 & 0 & 0 & 0 & 0 & 0 & 0 \end{pmatrix} \begin{pmatrix} K_{1q} \\ K_{1m} \\ K_{2q} \\ K_{2m} \\ K_{4q} \\ K_{4m} \\ K_{5q} \\ K_{5m} \end{pmatrix} = \begin{pmatrix} K_1(\overline{E}) \\ K_2(\overline{E}) \\ K_4(\overline{t}) \\ K_5(\overline{t}) \\ 0 \\ 0 \\ 0 \\ 0 \end{pmatrix}. \tag{3.15}$$

Solving this system yields the values of the constants. Renaming them for clarity as

$$\begin{aligned} K &= K_{1q}\,, \\ K_t &= K_{2q}\,, \\ K_{Et} &= K_{2m}\,, \end{aligned} \tag{3.16}$$

the $\tilde{C}_{L,F}$ becomes

$$\tilde{C}_{L,F}(l,t,E) = e^{K+K_t t+K_{Et}E\,t}\, l^{K_l}\,, \tag{3.17}$$

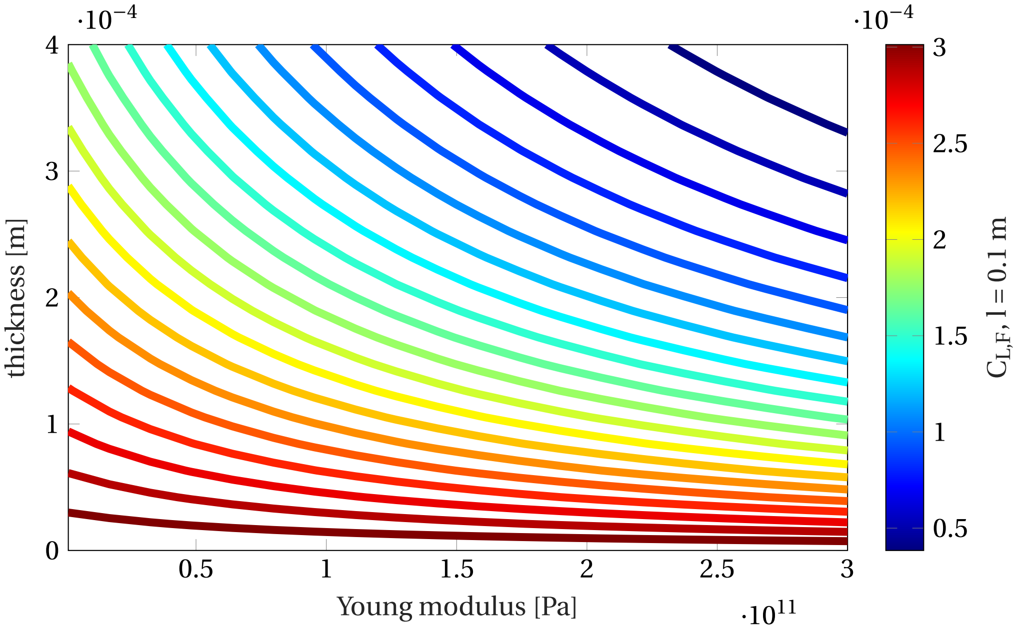

Figure 3.12: Isolines of the function $\tilde{C}_{L,F}(l,t,E)$ for $l = 0.1\,\mathrm{m}$.

or, rewritten in another form,

$$\ln\left(\frac{\tilde{C}_{L,F}}{l^{K_l}}\right) = K + (K_t + K_{Et}E)\,t\,. \tag{3.18}$$

The computed constant values are:

$$\begin{aligned} K &= 4.554\,, \\ K_t &= 1.486\cdot 10^{3}\,, \\ K_{Et} &= 1.631\cdot 10^{-8}\,, \\ K_l &= 1.524\,. \end{aligned} \tag{3.19}$$

The overall $\tilde{C}_{L,F}(l,t,E)$ behaviour is represented by its isolines in figure 3.12, for a given l. To validate the obtained scaling law, it is necessary now to test its accuracy in the complete parameter space (l,t,E). A complete cycle along t, l, and E would be excessively time consuming, for this reason a Monte Carlo approach is preferred here.
The three parameters are chosen at random, with a uniform distribution, in a range slightly larger than that used to compute the constants. The results of the simulations are compared with the value returned by the scaling law (3.17) for each iteration.
The mean error is −0.0041, and its standard deviation 0.0148. The first is an estimation of the method accuracy, and the second of the precision. Figure 3.13 is an histogram representation of the error.
The results show the good accuracy of the scaling law.

There are two visible flaws: the first are occasional high errors, up to 10%. They are due to simulations with very low $C_{L,F}$ (caused by low lengths), thus a very low denominator in equation (3.6). It could also be stated that the high errors are due to the lack of validity of the power law approximation at low length (figure 3.7). The other flaw is that the error distribution not centred in 0, but in −0.41%. The overall error is in any case sufficiently small, especially if it is considered that it is based on a low fidelity approximation of the airfoil aerodynamics. Nevertheless, the scaling law provides designer with a quick and dirty tool to explore the parameter space and select the main design parameters in a preliminary design phase.

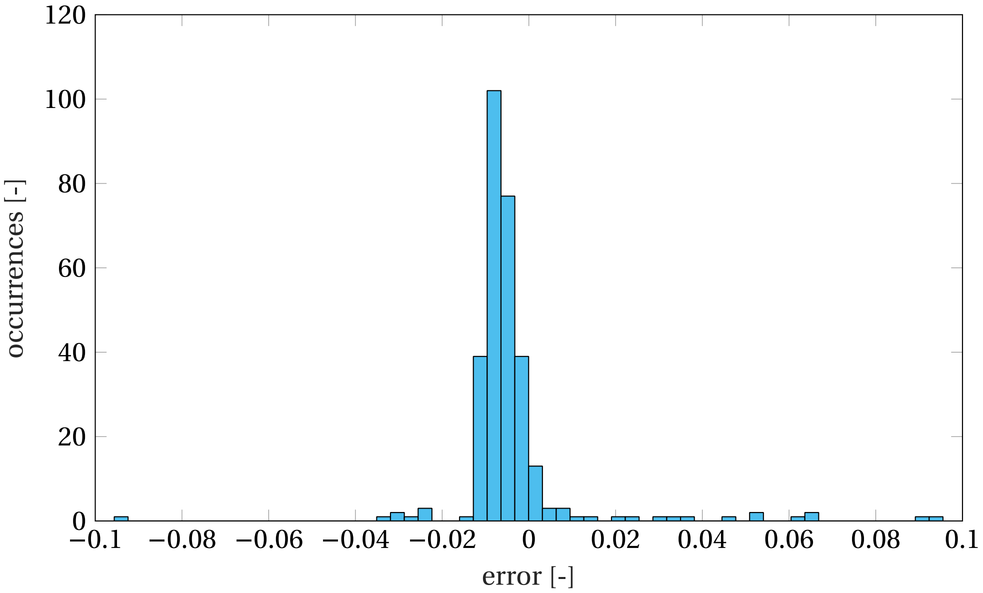

Figure 3.13: Error distribution of the $C_{L,F}$ algebraic model.

Pearson correlation coefficients between the error and the parameters sensibly different from zero may be linked to a poor estimation of some constants, or more generally to a bias of the scaling law. These coefficients are reported in table 3.5.

thickness	Young modulus	length
0.1116	0.0978	-0.3163

Table 3.5: Correlation coefficients between the prediction of the scaling law and the results of the simulations error and the values of the parameters.

The highest coefficient is the one associated with the length. Its value is ≈ -0.3, which indicates a weak correlation that can be explained with a slight misestimation of the K_l coefficient in particular.

A similar error analysis has been conducted for other airfoil shapes with comparable results, proving that this formulation is robust since it remains valid irrespective of the shape of the considered airfoil.

3.1.3 Aerodynamic parametric analysis

In the previous section, the actuation behaviour as function of its main structural characteristics was analysed still neglecting the effects of the Reynolds number, Mach number and angle of attack, for simplicity. In this section the dependence of the behaviour of the actuation system on these parameters will be discussed.

First, the effect of the angle of attack on the performance is evaluated. For this purpose, the $C_{L,F}$ is plotted as a function of the angle of attack and of another structural parameter, be it the plate thickness, its length or its Young modulus.
The range of values used in this analysis is reported in table 3.6.

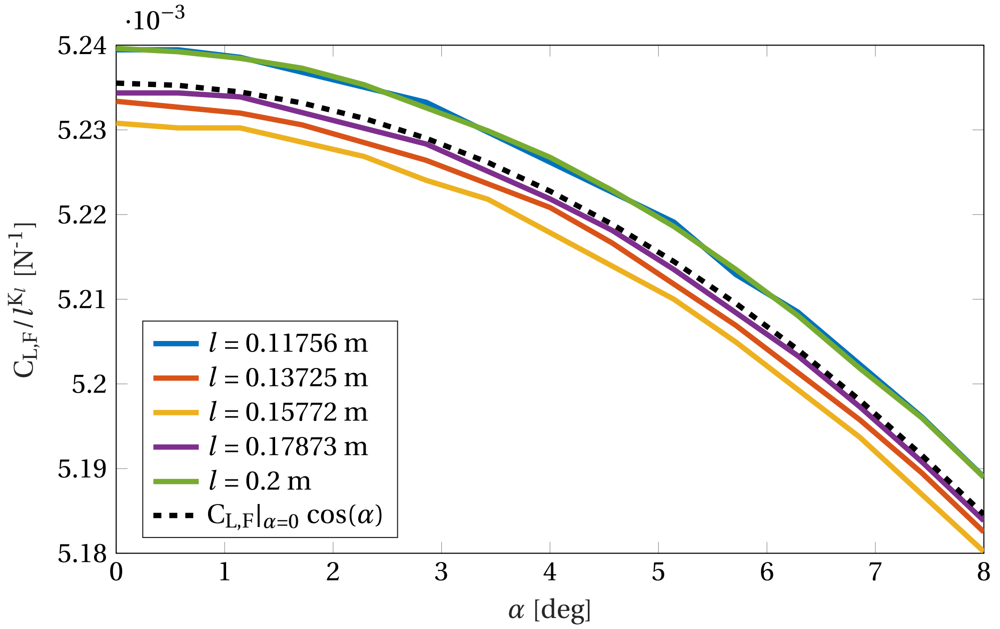

Figure 3.14: Inviscid $C_{L,F}$ dependence from α; the $C_{L,F}$ is scaled over l^{K_l} to facilitate the visualization of multiple curves.

parameter	minimum value	maximum value	
angle of attack	0°	8°	32
plate thickness	$6\cdot10^{-5}$ m	$4\cdot10^{-4}$ m	20
plate length	$1\cdot10^{-2}$ m	$2\cdot10^{-1}$ m	20
plate Young Modulus	$1\cdot10^{9}$ Pa	$7\cdot10^{10}$ Pa	20

Table 3.6: Range of the parameters used to investigate the angle of attack effects on the $C_{L,F}$.

The overall angle effect is a simple $C_{L,F}$ rescale by a $\cos\alpha$ term. This phenomenon is evident in figure 3.14 with the actuation length. The same effect is observed with both thickness and Young modulus.

The effect is rather small, and it is due to the apparent shortening of the plate with respect to the airflow by a $\cos\alpha$ coefficient.

The $C_{L,F}$ can therefore be completed as:

$$C_{L,F}(\alpha,l,t,E) = e^{K+(K_t+K_{Et}E)\,t}\, l^{K_l}\cos\alpha\,. \tag{3.20}$$

A further Monte Carlo analysis with this last formulation and the angle of attack as additional free parameter reveals that the model holds with the same accuracy and precision of the previous one. The mean error is -0.0051 with a standard deviation of 0.0112.

The coupling between the plate characteristics and the angle of attack is rather trivial in the inviscid case. When the viscosity is taken into account, the dependency between the parameters becomes more complicate.

In particular, the system behaviour varying the angle of attack and the Reynolds is now discussed.

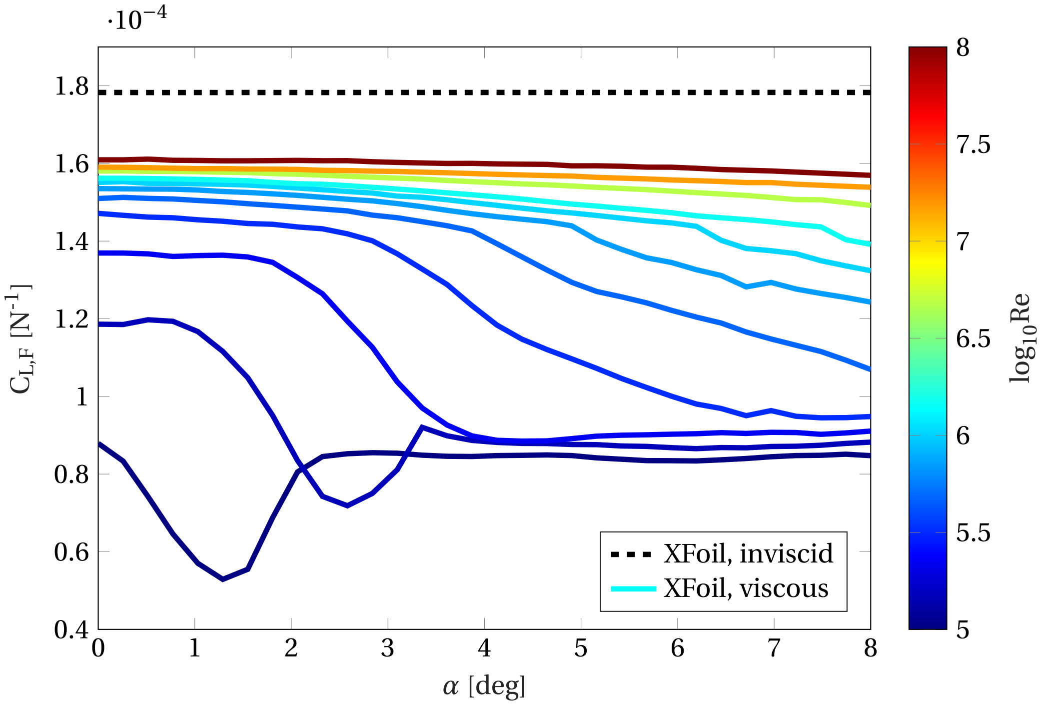

Figure 3.15: $C_{L,F}$ as a function of the angle of attack α and of the Reynolds number (colour map). The inviscid value is reported as a dashed line.

The intervals containing the values of the parameters used in the analysis are reported in table 3.7.

parameter	minimum value	maximum value	steps
angle of attack	0°	8°	32
Reynolds number	$1\cdot 10^5$	$1\cdot 10^8$	20

Table 3.7: Re and α intervals used to compute the $C_{L,F}$ viscous behaviour.

The numerical results are shown in figure 3.15. All the $C_{L,F}$ computed in this section are already corrected by a $\cos\alpha$ term to isolate the viscous effects.

The particular viscous $C_{L,F}$ behaviour shown in figure 3.15 is due to the boundary layer characteristics in the actuated part of the airfoil. Decreasing the Reynolds number reduces the effectiveness of the actuation. In fact the boundary layer and wake thickness are 0 in an inviscid simulation, thus the actuator always works in a region with a velocity similar to the asymptotic one. The presence of the boundary layer slows down the airflow near the airfoil in a viscous simulation, thus decreasing the actuation effectiveness [14].
The analysis should take into account the following parameters characterising the thickness and ve-

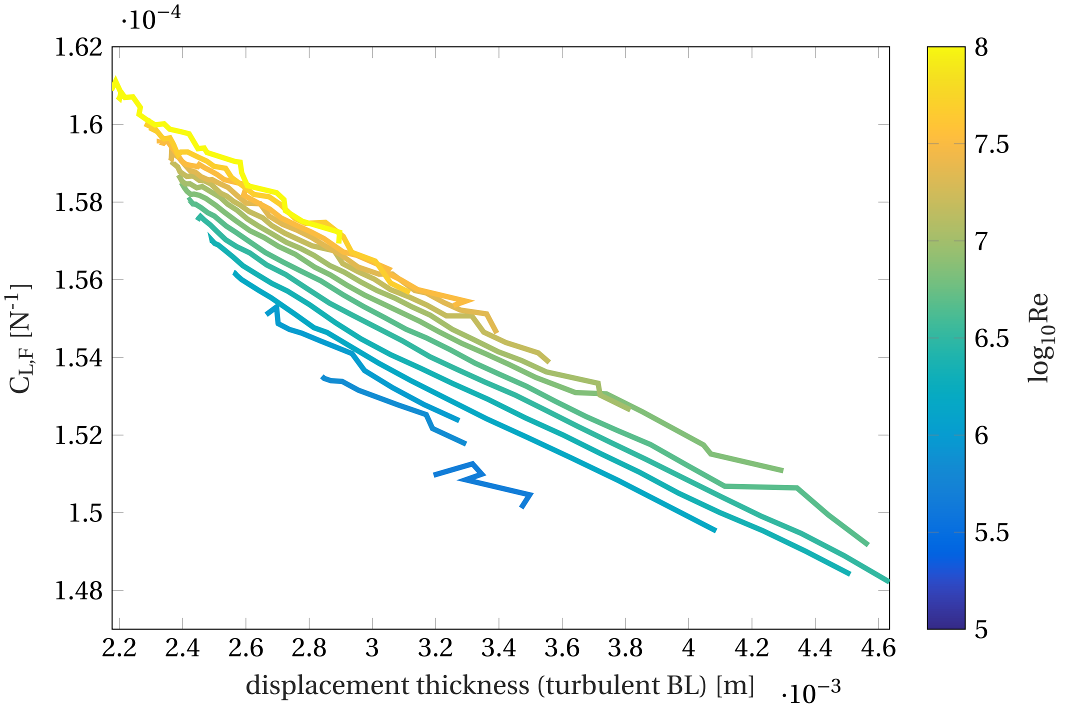

Figure 3.16: $C_{L,F}$ plotted against the displacement thickness over the actuator, plotted only for turbulent boundary layers; the curves vary along the α, not shown in this graph.

locity profile in the boundary layer to understand the underlying flow dynamics:

$$\begin{aligned} \delta^*(\xi) &= \int_0^\infty \left(1 - \frac{u_p(\xi,\eta)}{u_\infty}\right) \mathrm{d}\eta \ : \quad \textbf{displacement thickness}\,, \\ \theta(\xi) &= \int_0^\infty \frac{u_p(\xi,\eta)}{u_\infty}\left(1 - \frac{u_p(\xi,\eta)}{u_\infty}\right) \mathrm{d}\eta \ : \quad \textbf{momentum thickness}\,, \\ H(\xi) &= \frac{\delta^*(\xi)}{\theta(\xi)} \ : \quad \textbf{shape factor}\,. \end{aligned} \tag{3.21}$$

(ξ,η) are local curvilinear coordinates, with ξ parallel to the airfoil surface, and η normal to it.

An operator $\mathcal{M}(\bullet)$ is defined such that:

$$\mathcal{M}\left(a(\xi;\ldots,F),N_F,l\right) \overset{\text{def}}{=} \frac{1}{N_F}\sum_{i=1}^{N_F}\frac{1}{2l}\int_{S_{\text{act}}} a(\xi;\ldots,F_i)\,\mathrm{d}\xi\,, \tag{3.22}$$

where S_{act} is the actuator surface, and N_F the number of simulation with different actuation forces used to estimate the $C_{L,F}$. This term represents the average of a generic aerodynamic quantity a (e.g. the displacement thickness, or the shape factor) on the actuator, averaged in turn among the cases at different actuation forces used to estimate the $C_{L,F}$.
The application of the $\mathcal{M}$ operator on the displacement thickness at each (α,Re) condition reveals a particular trend: the results reported in figure 3.16 suggest that the $C_{L,F}$ decreases linearly with $\mathcal{M}(\delta^*)$ when the flow on the actuator is turbulent (i.e. $H > 1.5$).
These results confirm what had been anticipated about the dependence of $C_{L,F}$ on the Reynolds number.

The values of the shape factor have also been averaged by the $\mathcal{M}$ operator. The behaviour as a function of the shape factor and of α is reported in figure 3.17. The $\mathcal{M}(H)$ value shown in figure 3.17 is

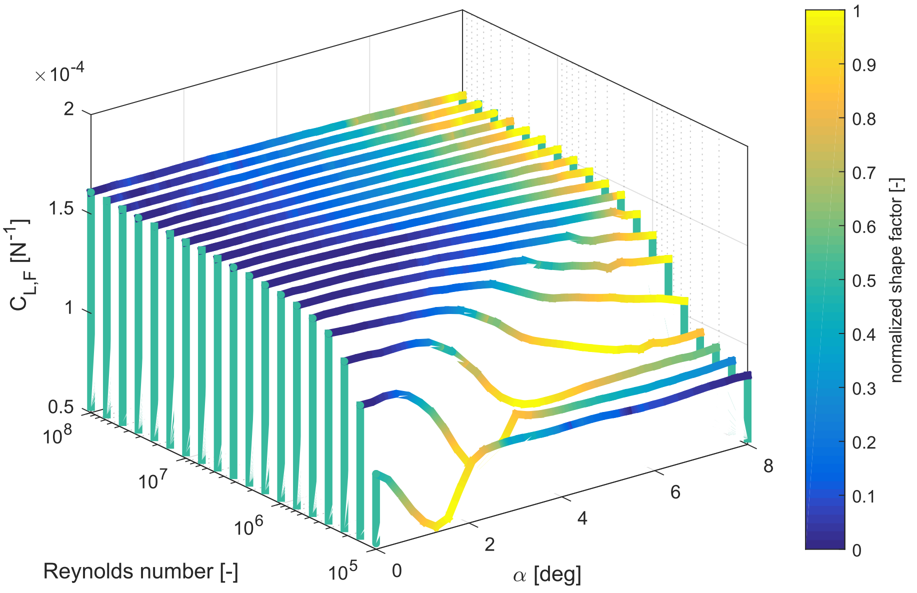

Figure 3.17: $C_{L,F}$ varying the angle of attack, Reynolds number and shape factor (colour).

(a) Low shape factor. **(b)** High shape factor.

Figure 3.18: Typical boundary layer velocity profiles for low and high values of shape factor; notice that high shape factors imply low velocity near the wall.

rescaled for each Reynolds number as follows:

$$\mathcal{M}_{H\,\mathrm{norm}}(\alpha,\mathrm{Re}) = \frac{\mathcal{M}(H(\alpha,\mathrm{Re})) - \mathcal{M}_{H\,\mathrm{min}}(\mathrm{Re})}{\mathcal{M}_{H\,\mathrm{max}}(\mathrm{Re}) - \mathcal{M}_{H\,\mathrm{min}}(\mathrm{Re})}\,, \tag{3.23}$$

where

$$\begin{aligned} \mathcal{M}_{H\,\mathrm{min}}(\mathrm{Re}) &= \min_{\alpha}\left(\mathcal{M}(H(\alpha,\mathrm{Re}))\right)\,, \\ \mathcal{M}_{H\,\mathrm{max}}(\mathrm{Re}) &= \max_{\alpha}\left(\mathcal{M}(H(\alpha,\mathrm{Re}))\right)\,. \end{aligned} \tag{3.24}$$

From figure 3.17 it can be seen that the local drop of $C_{L,F}$ is associated with high values of the shape factor. As a matter of fact, high shape factors are associated with boundary layer velocity profiles with a low derivative of the velocity with respect to the wall distance at the wall, and therefore small velocities near the wall. This is clearly shown in figure 3.17.

The complex behaviour of viscous flows prevents a simple representation of $C_{L,F}$ as a function of the Reynolds number in closed form, but these observations on the connection between the shape of the

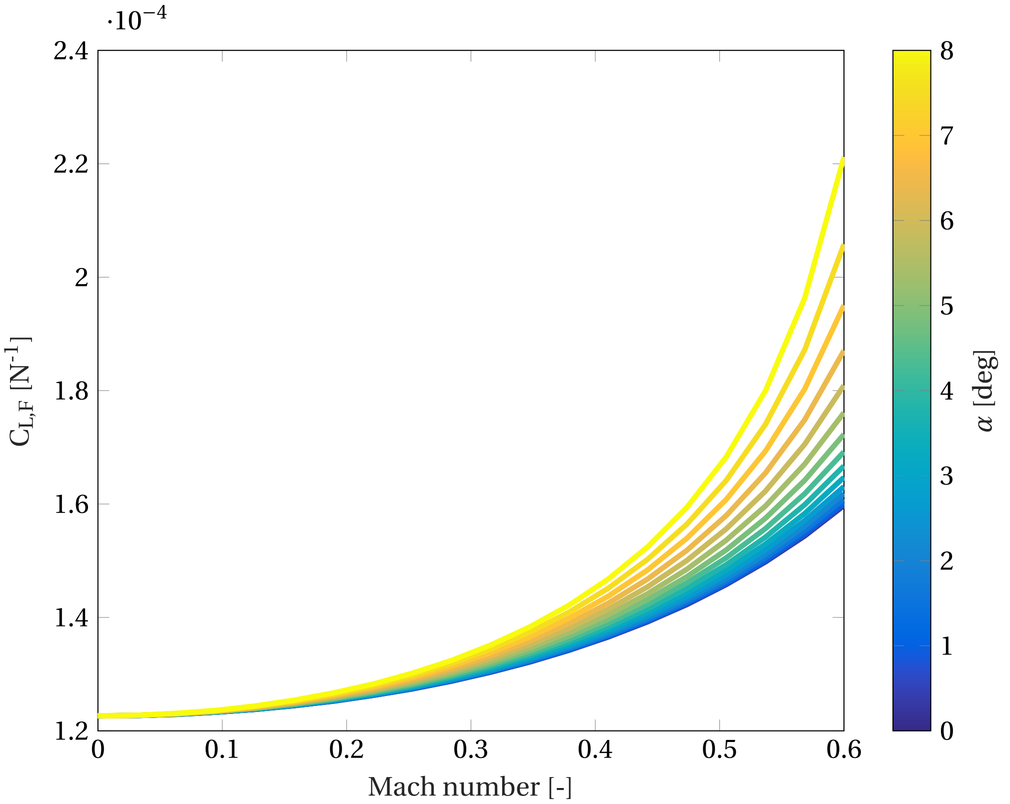

Figure 3.19: $C_{L,F}$ results as a function of the Mach number and of the angle of attack.

boundary layer velocity profile and the effectiveness of the control plate allow one to predict when such actuation systems could be ineffective.
XFoil can apply a correction to incompressible results for non-null Mach numbers. This is done exploiting the Karman-Tsien correction [1] (equation (3.25)). The results are valid while the Mach number is well below the airfoil critical Mach number.

$$\begin{aligned} C_P &= \frac{C_{P\text{inc}}}{\beta + \frac{\lambda}{2}(1+\beta)C_{P\text{inc}}}, \\ \beta &= \sqrt{1-M^2}, \\ \lambda &= \frac{M^2}{(1+\beta)^2}. \end{aligned} \tag{3.25}$$

The values are shown in table 3.8.

parameter	minimum value	maximum value	steps
angle of attack	0°	8°	16
Mach number	0	0.6	20

Table 3.8: Parameter intervals used to investigate the $C_{L,F}$ dependence on the Mach.

Figure 3.19 reveals the results. The actuation performance increases significantly with the Mach number, especially at high angles of attack, with an increase around 30% to 60% at a Mach number of 0.6.

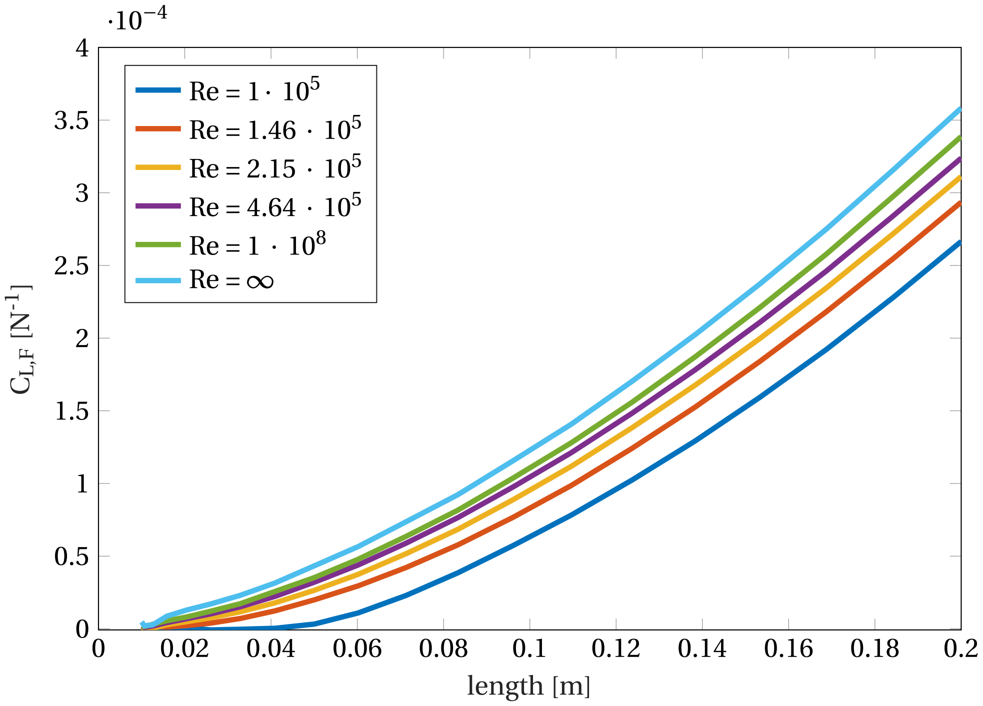

Figure 3.20: $C_{L,F}$ as function of the plate length, for different Reynolds numbers.

The Karman-Tsien correction does not depend explicitly on the angle of attack, but figure 3.19 suggests that the angle of attack still plays a significant role varying the Mach number. This is caused by the lack of commutativity of the Karman-Tsien correction with the integration. These results are neither power laws, exponential, or logarithmic.

Another interesting result can be obtained by plotting $C_{L,F}$ as a function of the Reynolds number and of the actuator length (table 3.9).

parameter	minimum values	maximum values	steps
plate length	$1 \cdot 10^{-2}$	$2 \cdot 10^{-1}$ m	20
Reynolds number	$1 \cdot 10^{5}$	$1 \cdot 10^{8}$	20

Table 3.9: Parameter intervals used to investigate the $C_{L,F}$ dependence on the Reynolds number and the length.

The results are presented in figure 3.20. The $C_{L,F}$ dependence on the Reynolds number and the length can be modelled as a decrease of the apparent length, as figure 3.21 shows. The $(l, \mathrm{Re}, C_{L,F})$ curves collapse on the same when appropriately translated by a function of the Reynolds number. The adopted scaling function is shown in figure 3.22 together with $\mathcal{M}(\delta^*)$ for the simulation with $l = 0.0158\,\mathrm{m}$, for instance. The two curves clearly exhibit the same behaviour, and the relation between the apparent shortening and the mean displacement thickness is shown in figure 3.23. The figure clearly shows that they depend linearly on each other in the two regions of fully laminar and fully turbulent regime, with a small step and a slope change when the boundary layer transition occurs on the actuator.
Te same qualitative behaviour can be observed for each l, the main difference being a shift for the portion associated with a turbulent boundary layer, and both a shift and a slope change for the laminar part. Figure 3.24 shows this behaviour.

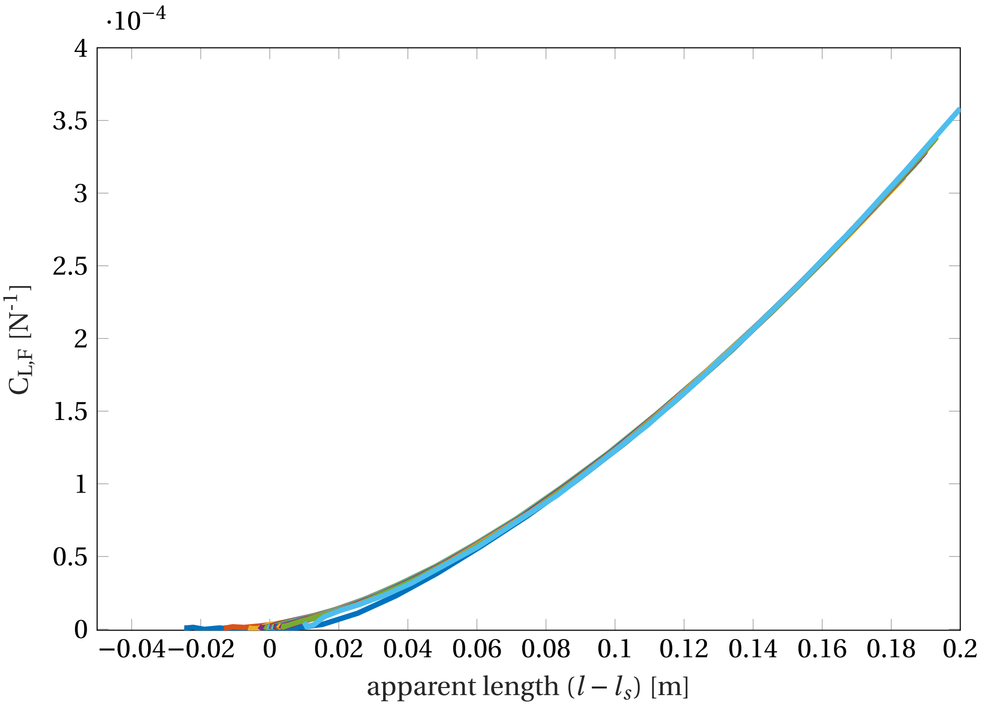

Figure 3.21: $C_{L,F}$ as a function of the length. The curves are obtained starting from those in fig. 3.20 by applying the scaling functions described in eq. (3.26). It is notable to note how the curves are nicely collapsed by the scaling function.

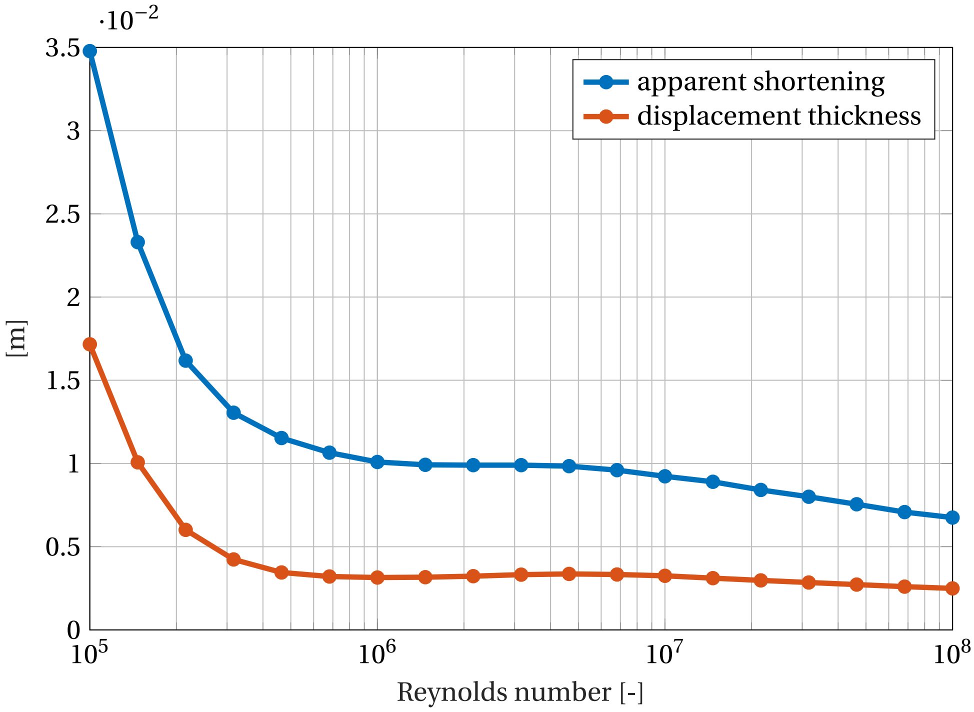

Figure 3.22: Shortening effect and mean displacement thickness at various Re.

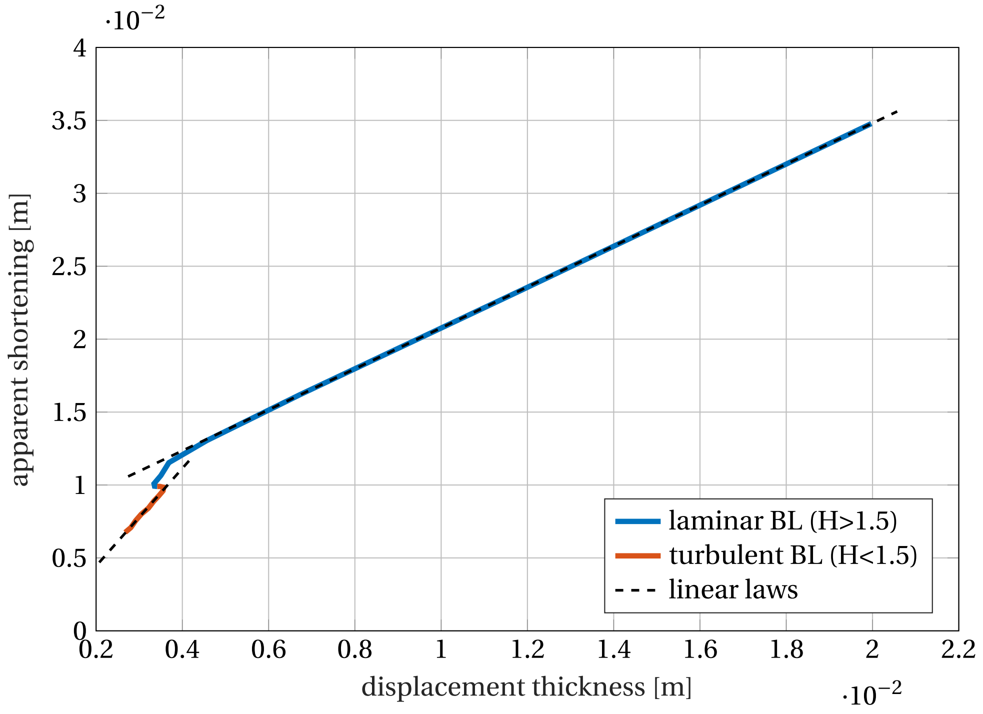

Figure 3.23: Apparent shortening as a function of the displacement thickness. The dashed lines represent the linear regression fro the two regions of the curve. The slope changes with transition.

The only fit parameter not varying with the l is the curve slope when the boundary layer over the actuator is turbulent, with a value of 0.289 ± 0.0249. The others fit parameters vary substantially, and a simple algebraic description of this variation has to be found yet.

$$\begin{cases} l_s(l, \mathrm{Re}) = S_{1t}\mathcal{M}\left(\delta^*(\xi; l, \mathrm{Re})\right) + S_{2t}(l) \; : & \textbf{turbulent boundary layer}\,, \\ l_s(l, \mathrm{Re}) = S_{1l}(l)\mathcal{M}\left(\delta^*(\xi; l, \mathrm{Re})\right) + S_{2l}(l) \; : & \textbf{laminar boundary layer}\,. \end{cases} \tag{3.26}$$

Table 3.10 summarizes the couples of parameters analysed together in this section.

	l	t	E	α	Re	Ma
l	–	✓	✓	✓	✓	
t	✓	–		✓		
E	✓		–	✓		
α	✓	✓	✓	–	✓	✓
Re	✓			✓	–	
Ma				✓		–

Table 3.10: Parameters that have been varied in the same computations.

This analysis reveals different properties of this type of actuation that are summarised hereafter:

1. in the inviscid case the scaling law for $C_{L,F}$, $C_{L,F}^{\mathrm{inv}}(\alpha, l, t, E)$ has a simple algebraic formulation:

$$C_{L,F}^{\mathrm{inv}}(\alpha, l, t, E) = e^{K+(K_t+K_{Et}E)t}\, l^{K_l} \cos\alpha\,; \tag{3.27}$$

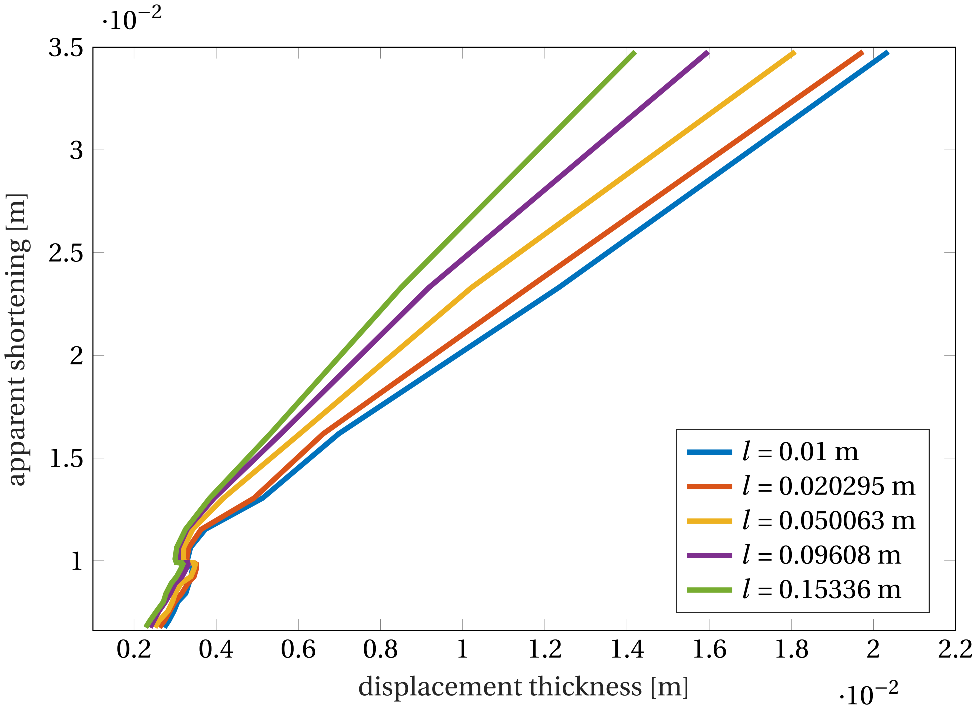

Figure 3.24: Apparent shortening as a function of the displacement thickness, for several plate lengths.

2. in the viscous case the scaling laws for $C_{L,F}$ become more involved. $C_{L,F}^{\text{visc}}$ decreases linearly with the displacement thickness when varying the angle of attack for turbulent boundary layer:

$$C_{L,F}^{\text{visc}}(\alpha,\dots) = \left(K_{\text{Re}}(\text{Re}) - \delta^*(\alpha,\dots)\right) C_{L,F}^{\text{inv}}\,; \tag{3.28}$$

if the boundary layer is laminar, the behaviour seems too difficult to be described in closed form.

3. the viscous effects can be modelled as an apparent actuator shortening; this effect is a directly proportional to the displacement thickness,

$$l_{\text{eff}} = l - l_s(l,\text{Re})\,; \tag{3.29}$$

4. the shape factor H influences heavily the $C_{L,F}^{\text{visc}}$: high shape factors cause it to drop; this phenomenon is particularly evident at low Reynolds numbers.

With these results in mind we can proceed to a lower abstraction level introducing the aeroelastic static coupling.

3.2 Coupled formulation

In the previous section, the aerodynamic calculation were not coupled with the structural deformation for simplicity. The presented results were thus overestimated the actual effect of compliant surfaces. Compliance can hardly be neglected in the present problem, where very thin control surfaces are considered.

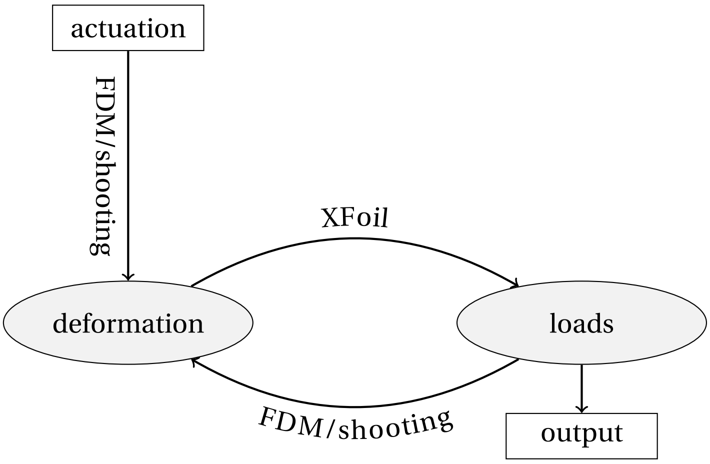

Figure 3.25: Simple scheme of the coupled structural-aerodynamic computations.

The goal of the present section is to investigate how the deformation of the control surfaces owing due to aerodynamic loads may influence their performance. A scheme describing the computational procedure is shown in figure 3.25. The coupled simulations take generally 15 to 40 iterations to converge: this means that the $C_{L,F}$ estimations are significantly slower than in the uncoupled case.
Being the deflection a function of both the structural and the aerodynamic loads, it is legitimate to cast a doubt on the linearity of the $C_{L,F}$ with respect to actuation forces variations. Figure 3.26 shows the behaviour linearity with respect to the actuation force and its accordance with the nonlinear beam model (their ratio is shown in figure 3.27). This means that the $C_{L,F}$ is still a meaningful parameter.

The first analysis is done with the parameter values specified in table 3.11.

parameter	value	parameter	value
airfoil	NACA 0012	**MFC Young modulus**	30 GPa
airfoil points	100	**MFCs per spanwise meter**	5
plate thickness	$0.3 \cdot 10^{-3}$ m	**MFC forces range**	$-308 \div 308$ N
plate length	$0.1 \cdot 10^{0}$ m	**angle of attack**	0
plate angle	0	**Reynolds number**	∞
plate Young modulus	70 GPa	**Mach number**	0
plate points	30	**max XFoil iterations**	150
MFC thickness	$0.3 \cdot 10^{-3}$ m	**XFoil kill time**	3 s
MFC width	$0.64 \cdot 10^{-1}$ m	**XFoil kill time**	3 s
MFC width	$0.64 \cdot 10^{-1}$ m	**air density**	$0.9\,\mathrm{kg/m^3}$
MFC plate coverage	100%	**wind velocity**	$50\,\mathrm{m\,s^{-1}}$

Table 3.11: Base data used for the coupled $C_{L,F}$ analysis.

The $C_{L,F}$ analysis varying the plate length and thickness reveals a quite different behaviour with respect to the uncoupled case (figure 3.28). While, in the uncoupled case, we observed a monotonic increasing behaviour for $C_{L,F}(l)$ and a monotonic behaviour for $C_{L,F}(t)$, in the present case the behaviour is no longer monotonic. The reason is that the deformation of the actuation plate due to aerodynamic loads increases with the plate length, decreasing its effectiveness.
Since the computation of the complete (l, t, V) space is computationally onerous, an approach in terms of optimum-envelope has been chosen. Figure 3.28 also shows the envelope of $C_{L,F}(l, t)$ as a

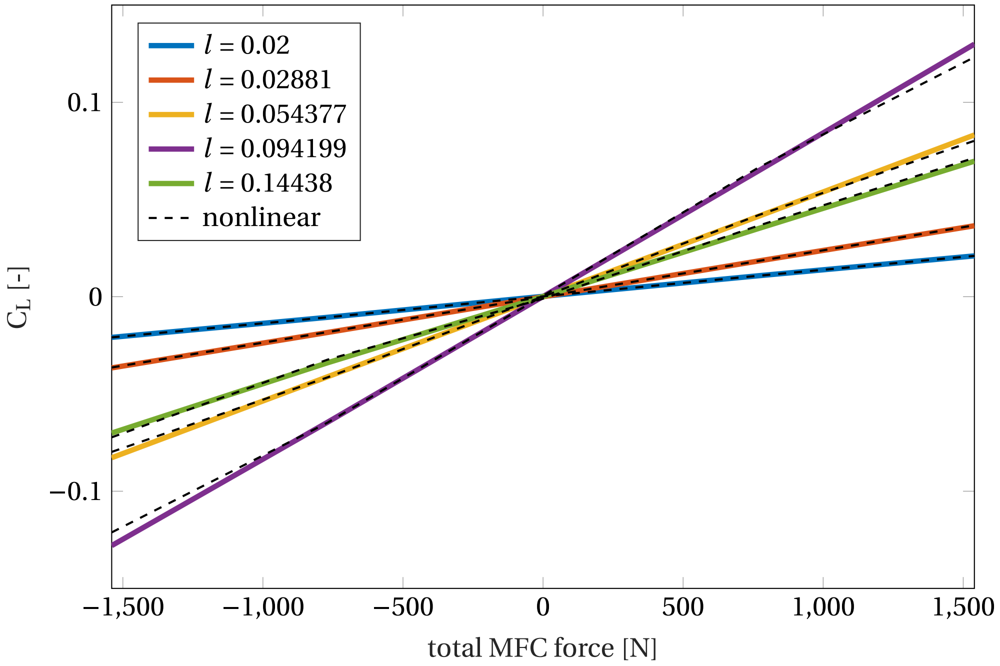

Figure 3.26: Lift coefficient for the coupled formulation as a function of the actuation force for several actuator lengths computed by both the linear and the nonlinear model; the key in the figure does not show the length for each nonlinear result since they are almost overlapped to the corresponding linear result.

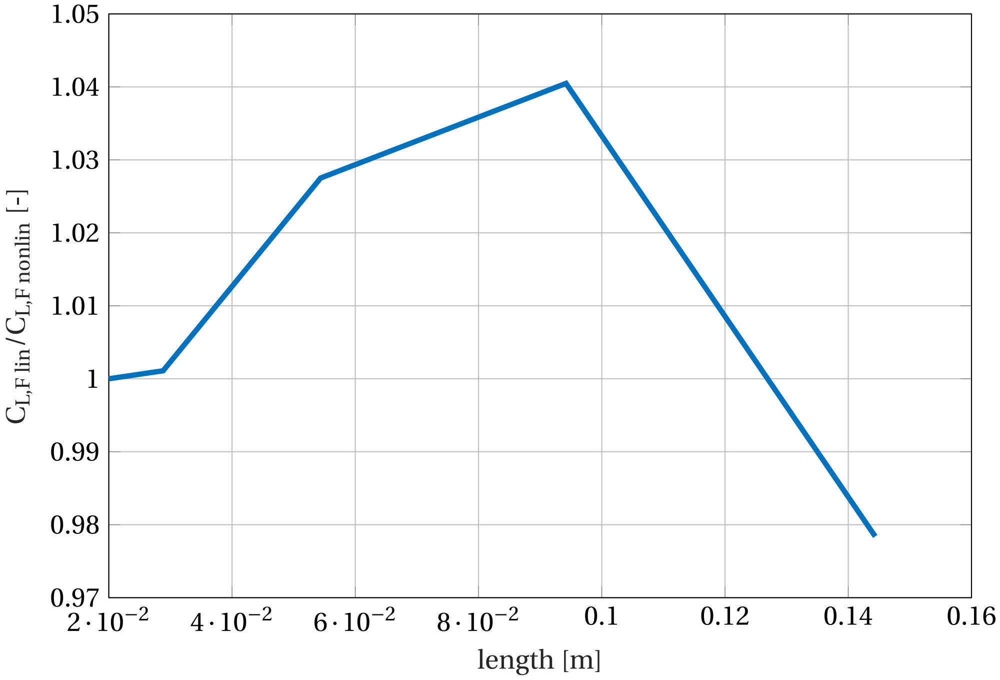

Figure 3.27: Ratio between the values of $C_{L,F}$ computed with by the linear and nonlinear formulations; the calculation for $l = 0.2$ did not converge.

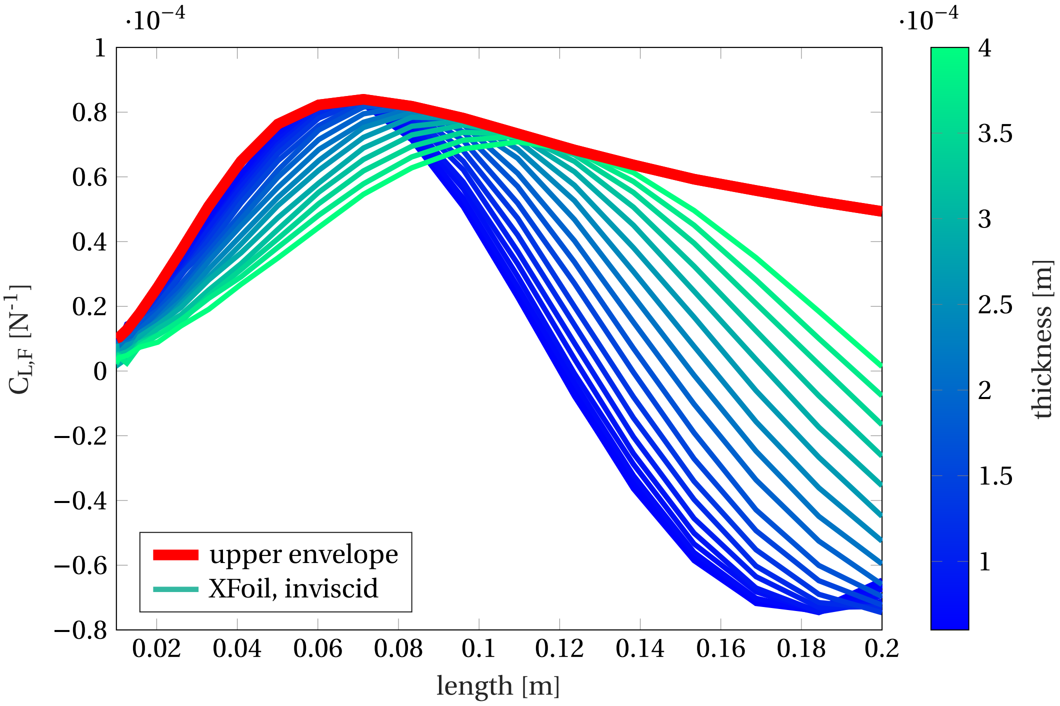

Figure 3.28: $C_{L,F}$ plotted as a function of the plate length for several values of thickness (blue-green lineas), at $50\,\mathrm{m\,s^{-1}}$. The envelope of the curves is also reported (red line).

function of l. The envelope presents a maximum, that is the maximum inviscid $C_{L,F}$ achievable at a given velocity ($50\,\mathrm{m\,s^{-1}}$).
The optimal thickness is shown in figure 3.29 as a function on the length. It is reasonably represented by a piecewise linear behaviour. For small lengths the optimum thickness is zero, meaning that the rigidity of the actuator (30 GPa) is sufficient or even excessive for the purpose.

The results reported in figure 3.30 are obtained by computing the envelope for different velocities. The null velocity curve is equivalent to the uncoupled computation case, and is given as a reference in order to estimate the $C_{L,F}$ loss due to the aeroelastic coupling. Figure 3.31 shows a zoom of the lower part of the graph.
A log-log plot shows a clearer picture of the coupled behaviour: figure 3.32 unveils how the uncoupled-case power law behaviour is substituted with another power-law, but with negative exponent.
This is positively surprising: even though these curves are defined in a more complex way than the ones in figure 3.30, their modeling is way simpler, and the complexity in their definition does not end up in a complexity in their description.
The ratio between the uncoupled $C_{L,F}$ and the coupled one can be interpreted as an aeroelastic efficiency:

$$\mathcal{E}_c = \frac{C_{L,F}^{\text{coupled}}}{C_{L,F}^{\text{uncoupled}}} \in [0,1]\,. \tag{3.30}$$

This ratio decreases with a power law of both length (figure 3.33) and velocity (figure 3.34). The exponents do not sensibly vary in both the parametrisations. Varying the length, it is −2.136 ± 0.05454, varying the velocity it is −1.398 ± 0.08058. Being a power law on both parameters means that the

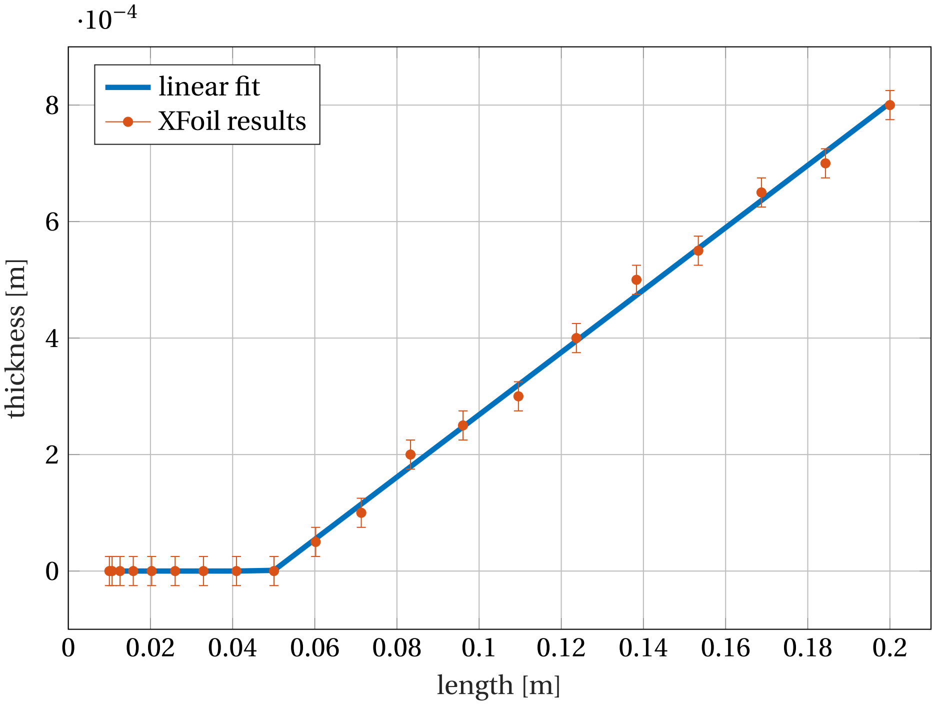

Figure 3.29: Optimal thickness as function of the plate length; the error bar represents the resolution of the method used to identify the envelope.

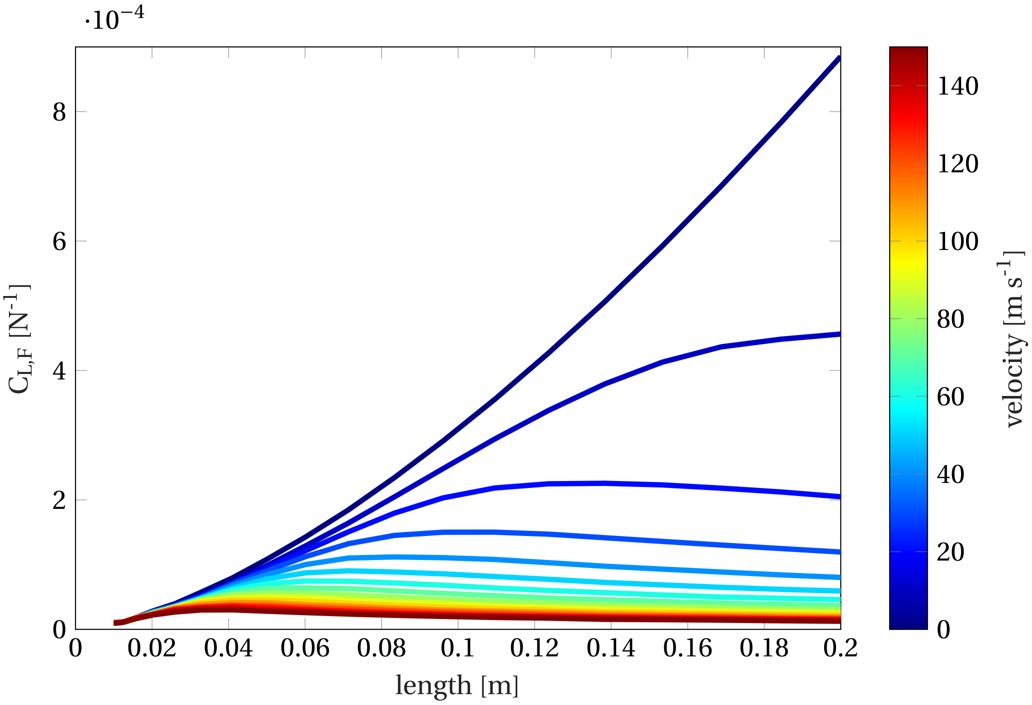

Figure 3.30: $C_{L,F}$ as function of the plate length, for several velocities; every computed condition is at optimal thickness.

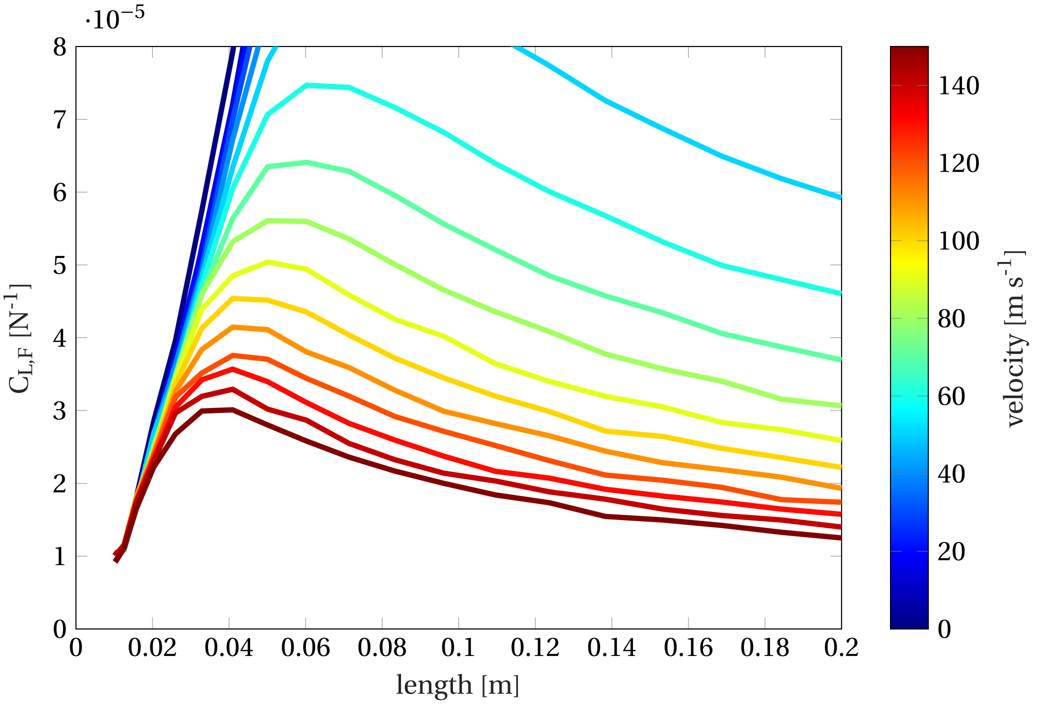

Figure 3.31: Zoom of the lower part of figure 3.30.

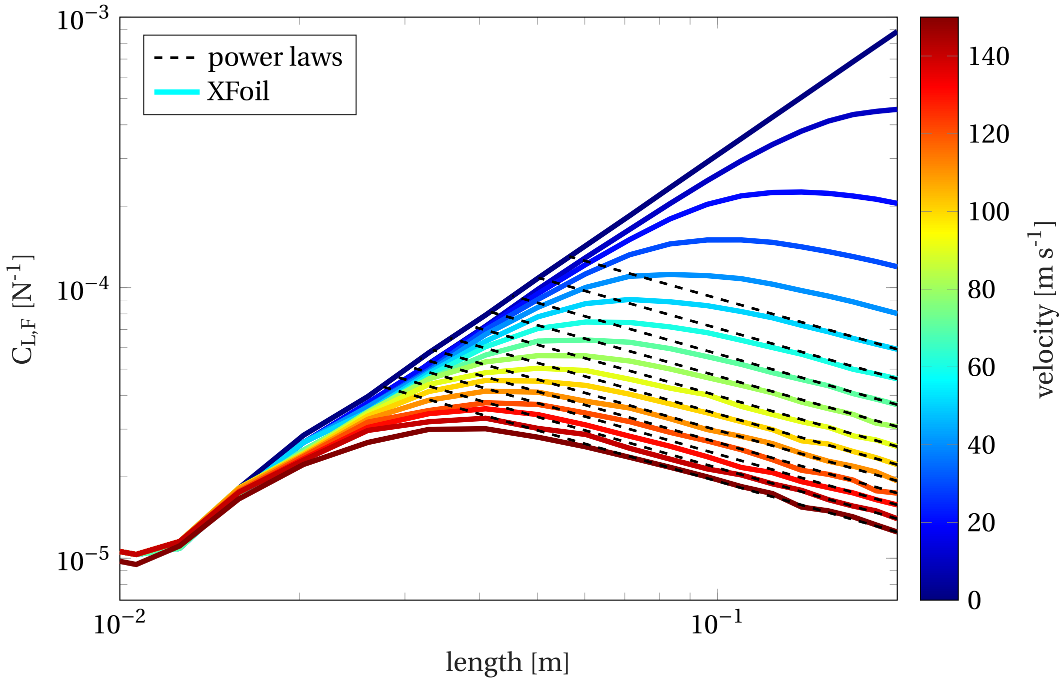

Figure 3.32: $C_{L,F}$ as function of the plate length, for several velocities, at optimal thickness, in logarithmic axes. The dashed lines model some of the decreasing branches as power laws.

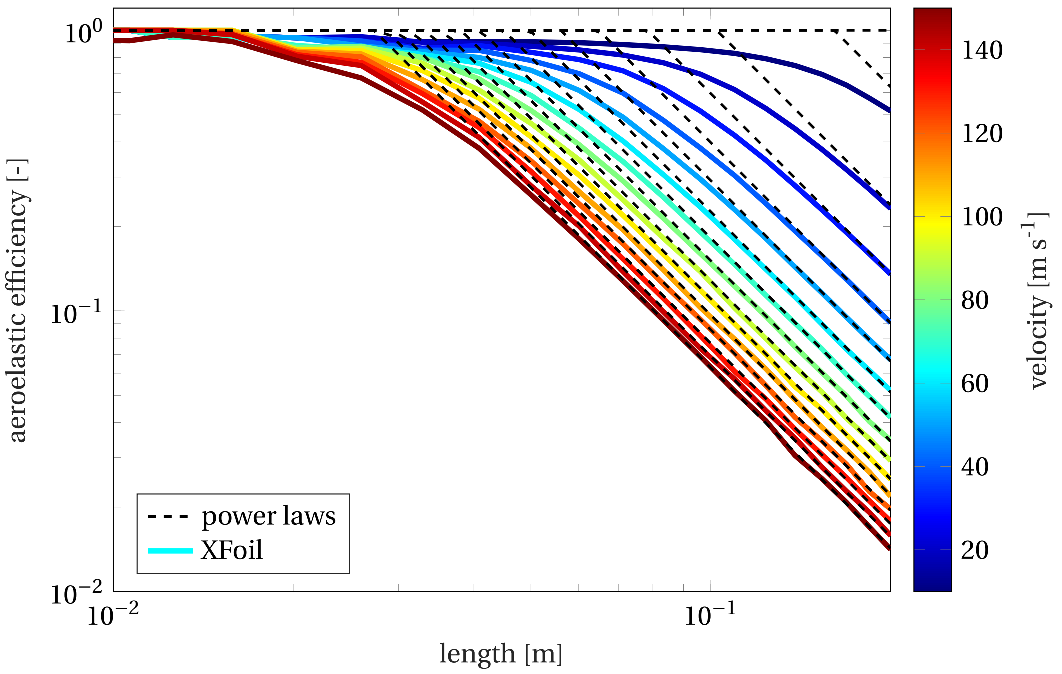

Figure 3.33: Aeroelastic efficiency as function of the length of the plate, for several velocities. It is defined as the ratio of the coupled and uncoupled optimal $C_{L,F}$ for a given condition. It has a transition between being constant and unitary to being a decreasing power law.

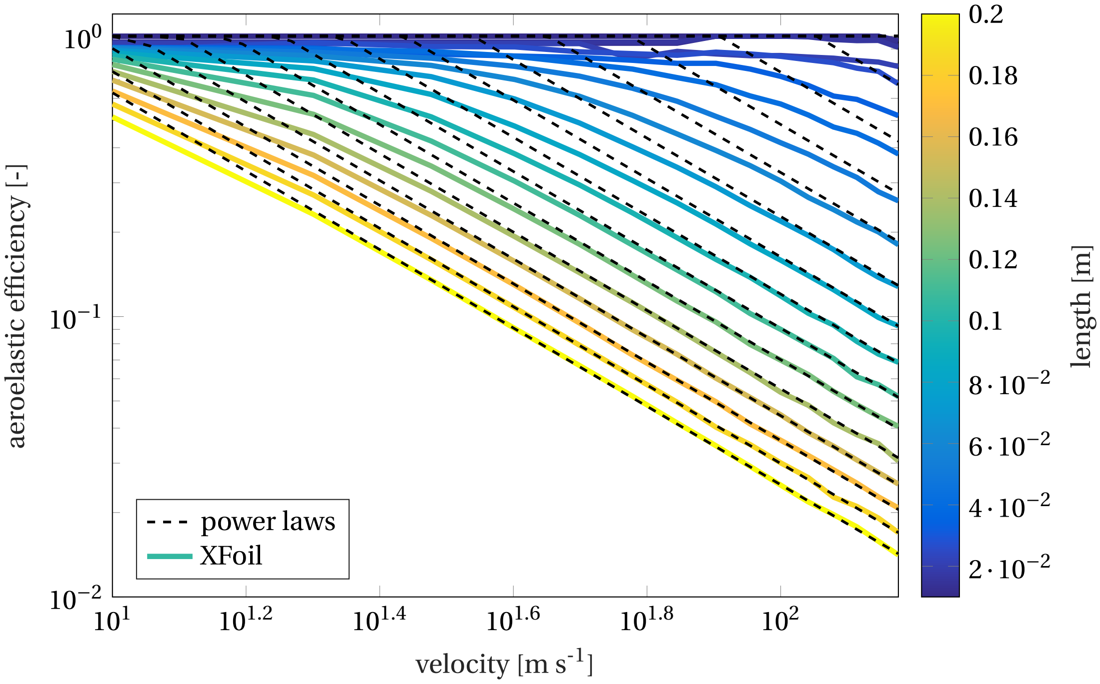

Figure 3.34: Coupling efficiency as function of the velocity, for several lengths. It has a transition between being constant and unitary to being a decreasing power law.

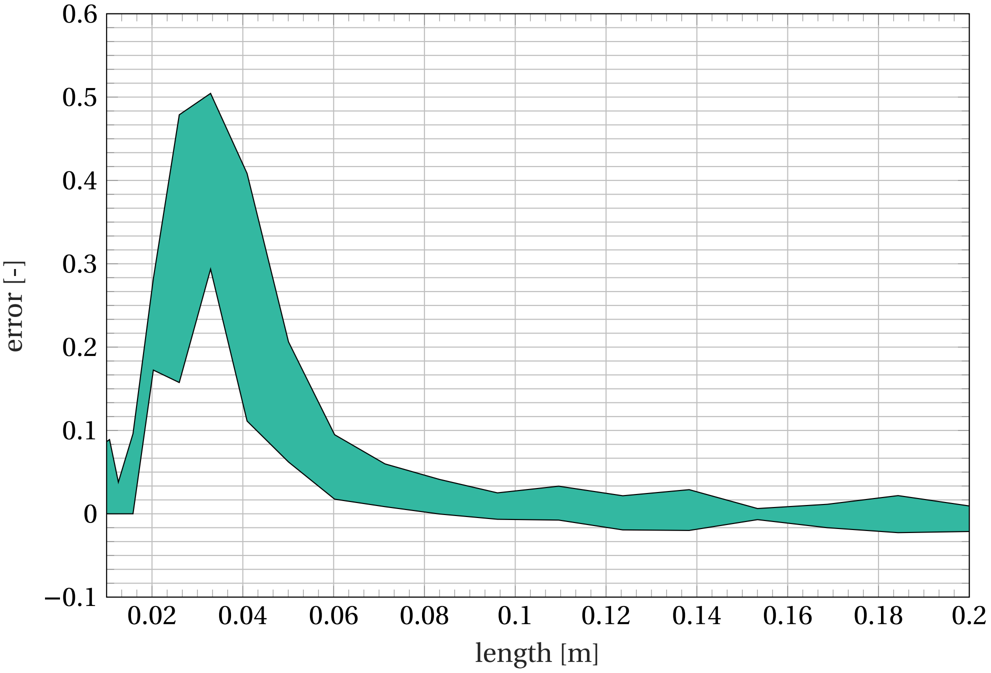

Figure 3.35: Envelope of the efficiency power-law model errors for different velocities ($90 \div 150\,\mathrm{m\,s^{-1}}$); notice the peak corresponding to the transition from the decreasing power law to the constant unit value.

scaling law for $\mathcal{E}_c$ can be expressed as

$$\tilde{\mathcal{E}}_c(l,V) = \begin{cases} Q\,V^{Q_V}\,l^{Q_l} & l > l_c(V)\,, \\ 1 & l < l_c(V)\,, \end{cases} \tag{3.31}$$

where l_c is the length at which the power laws intersect with the value $\mathcal{E}_c = 1$, and the computed constants are:

$$\begin{aligned} Q &= 0.505\,, \\ Q_V &= -1.398\,, \\ Q_l &= -2.136\,. \end{aligned} \tag{3.32}$$

Notice that these values can be function of other parameters, e.g. the Young modulus. A more complete parameter space exploration is considered too computationally onerous and out of the scope of the present investigation.
The error of equation (5.7) efficiency is computed as

$$err = \frac{\tilde{\mathcal{E}}_c - \mathcal{E}_c}{\mathcal{E}_c}\,, \tag{3.33}$$

and it is shown in figure 3.35. It has a peak associated with presence of a transition zone between the power law and the $\mathcal{E} = 1$ model. Figure 3.36 provides a clearer understanding of the $\mathcal{E}_c$ validity showing the error isolines as function of both length and velocity.
This scaling law does not work when $l \approx l_c$. If precision is needed in the transition between the constant law model and the decreasing power law, it is possible to model the aeroelastic efficiency as a fractional power law, i.e.:

$$\tilde{\mathcal{E}}_c(l,V) = \frac{1}{1 + G\,V^{G_V}\,l^{G_l}}\,, \qquad l < (1+P)\,l_c(V)\,, \tag{3.34}$$

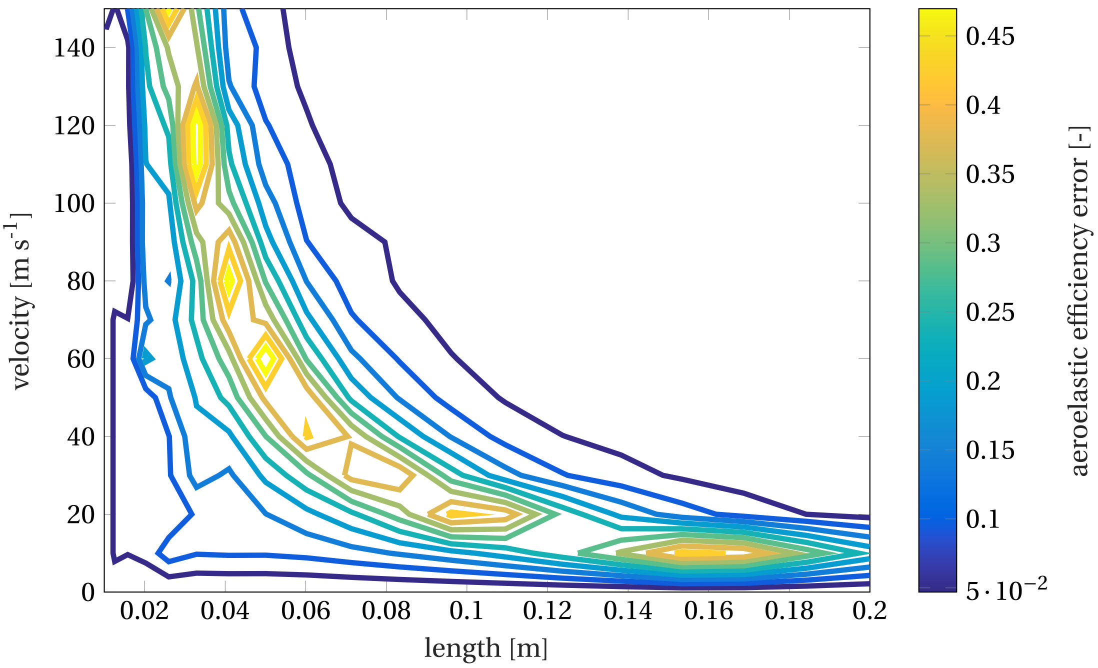

Figure 3.36: These error isolines show how length and velocity influences together the validity of the algebraic efficiency.

where

$$\begin{aligned} G &= 1.33\,, \\ G_V &= 1.7168\,, \\ G_l &= 2.6387\,, \end{aligned} \tag{3.35}$$

and P is a positive value that extends the applicability range of the scaling law also to actuators slightly longer than l_c.
This model works better in the transition between the two behaviours, as figure 3.37 suggests, but when lengths and velocities are high enough, it starts to fail.

The following list summarizes the aeroelastic effects that have been analysed, where $C^{\mathrm{c}}_{L,F}$ and $C^{\mathrm{uc}}_{L,F}$ indicate the coupled and uncoupled cases respectively:

1. the $C^{\mathrm{uc}}_{L,F}$ is a good approximation of the $C^{\mathrm{c}}_{L,F}$ only for low velocities or low lengths,
2. the $C^{\mathrm{c}}_{L,F}$ presents a maximum both as a function of length and as a function of thickness,
3. high lengths can cause the sign of $C^{\mathrm{c}}_{L,F}$ to become negative, i.e. a control reversal,
4. the optimal plate thickness for each velocity is a linear function of the plate length,
5. the $C^{\mathrm{c}}_{L,F}$ curves with the optimal thickness for each condition exhibit a power law decrease due to the aeroelastic coupling; modelling this effect as a coupling efficiency results as:

$$\begin{aligned} C^{\mathrm{c}}_{L,F} &= C^{\mathrm{uc}}_{L,F}\tilde{\mathcal{E}}_c\,, \\ \tilde{\mathcal{E}}_c(l,V) &= \begin{cases} Q\,V^{Q_V}\,l^{Q_l} & l > (1+P)\,l_c(V)\,, \\ \dfrac{1}{1+G\,V^{G_V}\,l^{G_l}} & l < (1+P)\,l_c(V)\,, \end{cases} \end{aligned} \tag{3.36}$$

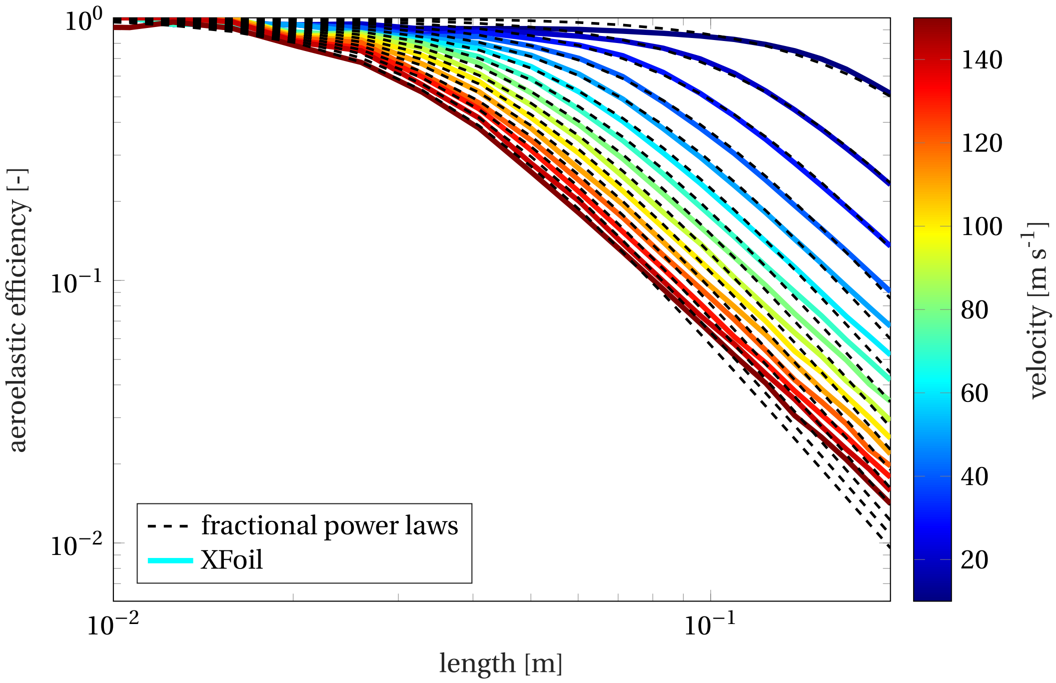

Figure 3.37: Aeroelastic efficiency as function of the length of the plate, for several velocities, with the fractional power law scaling represented with dashed lines.

It is useful now to repeat the computations for real cases, in order to understand the typical values that the $C_{L,F}$ can have in different situations.

3.3 Real case examples

3.3.1 PA-28-161 Warrior II

This sections will provide a more application-oriented analysis of the trailing edge MFC actuation. The Piper PA-28-161 Warrior II - a small general aviation aircraft - is used as study case [26] [19]. The aim of this analysis is to provide $C_{L,F}$ values and C_L increases with a MFC actuation for a typical general aviation application.

The values used for this computation are provided in table 3.12.

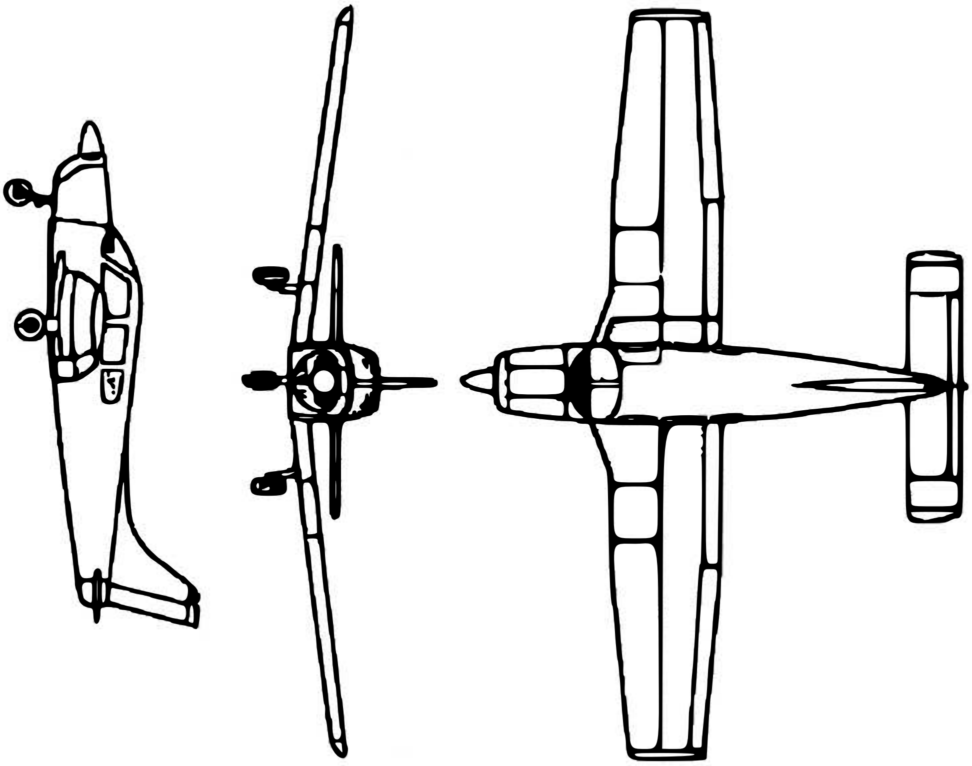

Figure 3.38: PA-28-161 Warrior II schematic view [26].

parameter	symbol	value
max cruising speed	V_{max}	$64\,\text{m}\,\text{s}^{-1}$
stall speed (flaps up)	V_{stall}	$28\,\text{m}\,\text{s}^{-1}$
max operating altitude	H_{max}	$4400\,\text{m}$
wing span	b_w	$10.67\,\text{m}$
wing surface	S_w	$15\,\text{m}^2$
wing chord at root	C_r	$1.6\,\text{m}$
wing chord at tip	C_t	$1.07\,\text{m}$
airfoil at root		NACA 65-415
airfoil at tip		NACA 65-415
max take-off weight	W_a	$1107\,\text{kg}$
basic empty weight	W_e	$680\,\text{kg}$

Table 3.12: PA-28-161 Warrior II characteristic needed for a first $C_{L,F}$ estimation.

Table 3.13 shows the actuation characteristics [21] envisaged for this application..

parameter	symbol	value
plate length	l	9.4 cm
plate thickness	t	$0 \rightarrow 0.5$ mm
plate material		aluminium
plate Young modulus	E_B	70 GPa
plate angle	β_B	0°
MFC plate coverage		90.4%
MFCs per meter		5
MFC model		M-8557-P1

Table 3.13: Properties of the actuation system selected for the PA-28-161 Warrior II.

The parameter space is explored varying the plate thickness and the wind velocity (table 3.14), with a 2000 m altitude and weight $W = 800\,\mathrm{kg}$. The angle of attack is computed for each horizontal, rectilinear, steady flight condition as a function of the flight speed with a simple equilibrium consideration:

$$\alpha_{\mathrm{eq}} = \alpha \quad s.t. \quad C_L(\alpha, \ldots)\frac{1}{2}\rho S_w V^2 - W = 0\,. \tag{3.37}$$

This is an approximation of the real case, since it does not take into account the horizontal tail downforce and the fuselage lift.

parameter	minimum value	maximum value	steps
plate thickness	0 mm	0.5 mm	10
flight velocity	$36\,\mathrm{m\,s^{-1}}$	$64\,\mathrm{m\,s^{-1}}$	10

Table 3.14: Parameter intervals chosen for the $C_{L,F}$ computation; the unspecified ones are taken from table 3.12 and 3.13.

The $C_{L,F}$ results are provided in figure 3.39. Figure 3.40 shows instead the maximum of the ratio between the actuated and non-actuated C_L. If XFoil does not converge in a particular condition, the $C_{L,F}$ value is computed with a cubic spline from adjacent conditions. These points are highlighted in the figures. The corresponding C_M increase is shown in figure 3.41. A correction in the elevator position is necessary to retain the aircraft longitudinal equilibrium.

The results look promising, but the model oversimplification must be taken into account. The values shown in this section must be taken as an optimistic reference w.r.t. the real case.

It is possible to scale up the problem and compute the actuation efficacy with a regional aircraft.

3.3.2 ATR-42

The second case study is on a ATR 42-300, a twin-turboprop regional airliner developed by ATR. A scheme can be found in figure 3.42 [3]. Its target are medium range domestic flights for 40 to 52 passengers.

Table 3.15 contains the needed data [3] [19] for an actuator effectiveness estimation.

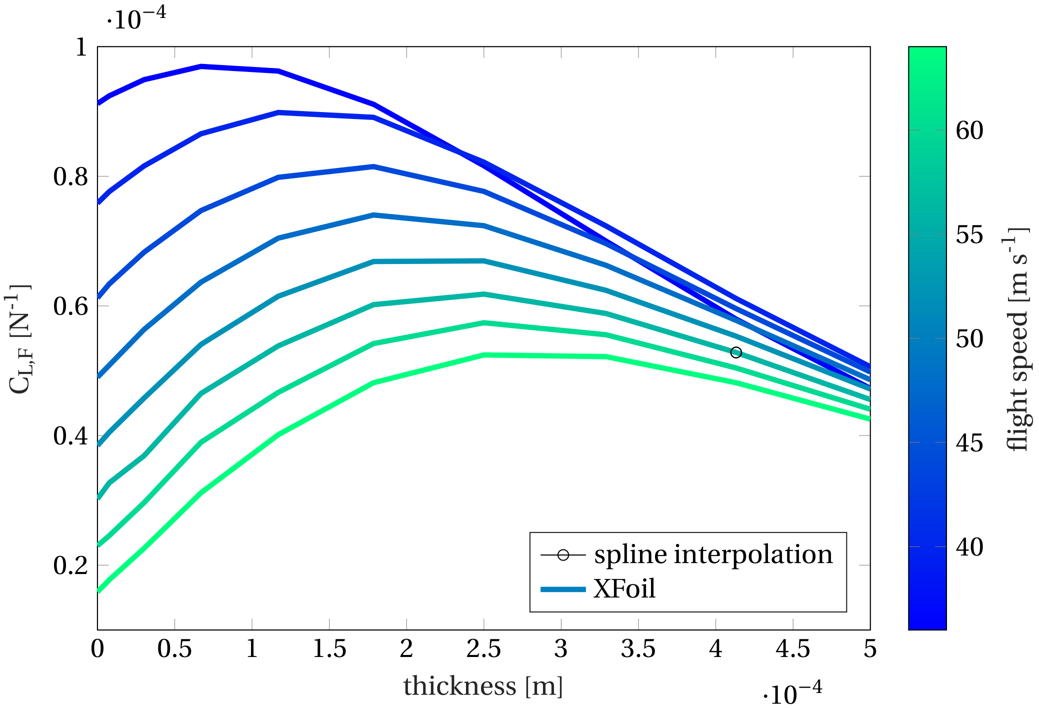

Figure 3.39: $C_{L,F}$ as function of the plate thickness, at several flight velocities, at a given altitude (2000 m), for the PA-28-161.

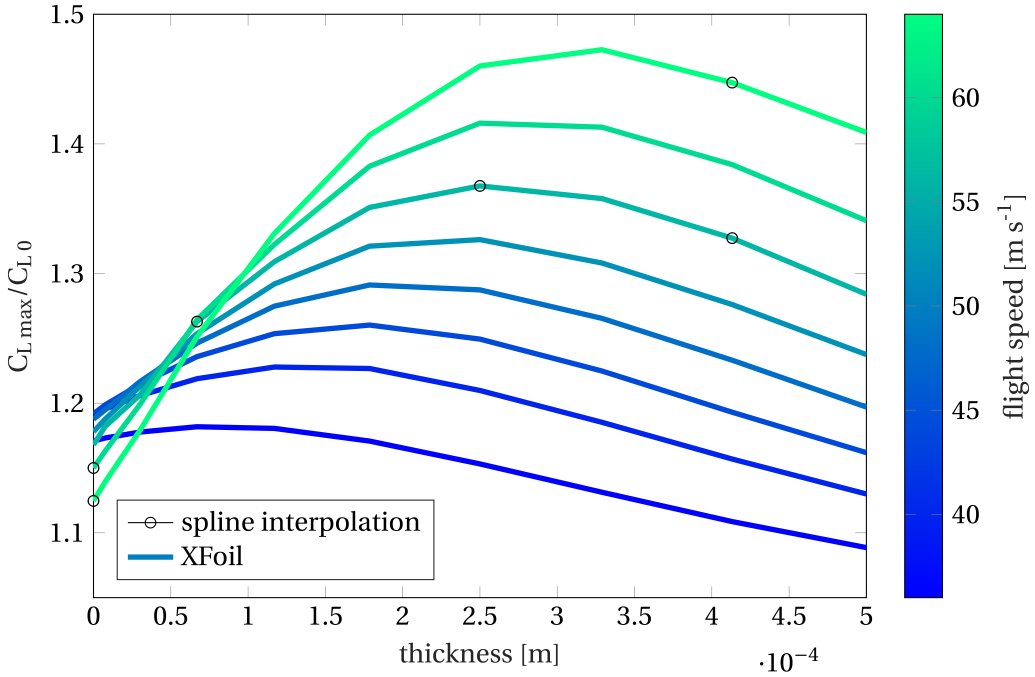

Figure 3.40: C_L increase as function of the plate thickness, at several flight speeds, at a given altitude (2000 m), for the PA-28-161; differently from the $C_{L,F}$, it increases with the velocity: this is due to the lower C_{L0} at higher speeds.

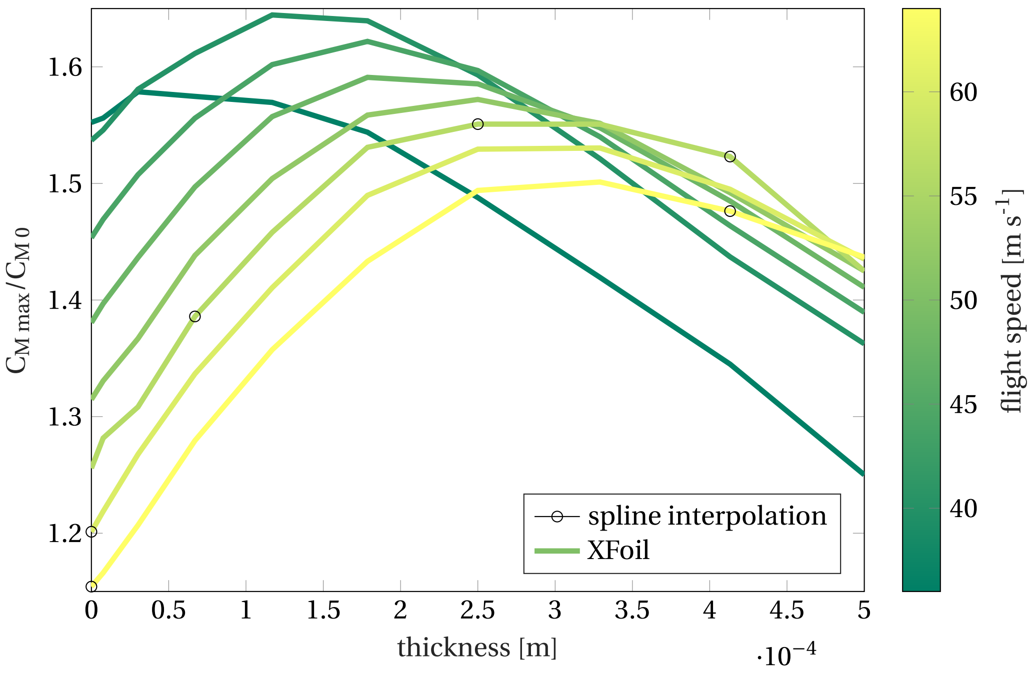

Figure 3.41: C_M increase as function of the plate thickness, at several flight speeds, at a given altitude (2000 m), for the PA-28-161.

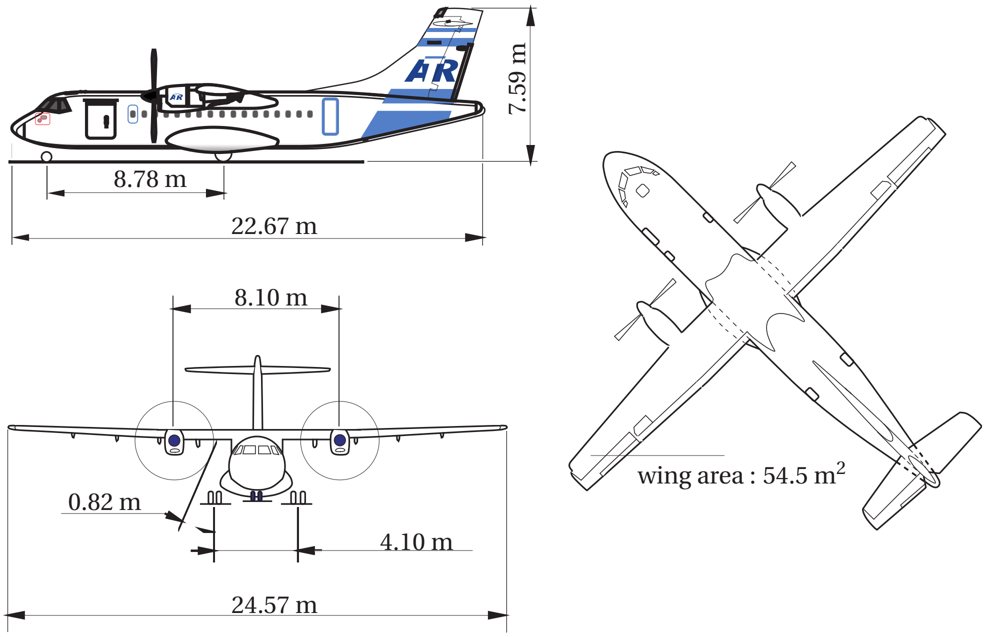

Figure 3.42: ATR 42-300 scheme.

parameter	symbol	value
max cruising speed (optimum FL)	V_{max}	$137\,\text{m}\,\text{s}^{-1}$
stall speed (flaps up)	V_{stall}	$54\,\text{m}\,\text{s}^{-1}$
max operating altitude	H_{max}	7620 m
wing span	b_w	24.57 m
wing surface	S_w	$54.5\,\text{m}^2$
wing chord at root	C_r	2.57 m
wing chord at tip	C_t	1.41 m
airfoil at root		NACA 43018
airfoil at tip		NACA 43013
max take-off weight	W_a	16 900 kg

Table 3.15: ATR 42-300 specifications needed for a $C_{L,F}$ estimation.

The actuation system has the following properties [21]:

parameter	symbol	value
plate length	l	9.4 cm
plate thickness	t	$0 \rightarrow 0.8$ mm
plate material		aluminium
plate Young modulus	E_B	70 GPa
plate angle	β_B	0°
MFC plate coverage		90.4%
MFCs per meter		5
MFC model		M-8557-P1

Table 3.16: Chosen actuation system properties for the ATR 42-300.

Notice that the size of the trailing edge plate is less than 5% of the mean airfoil chord. This is due to the chosen actuator, which is the longest available with sufficient actuation force at the moment. As the previous case, the first set of simulations will explore the parameter space with respect to the actuation thickness and the flight velocity between the stall condition and the maximum cruising speed (table 3.17). The chosen altitude is 7500 m, rather near to the ceiling one.
The angle of attack is computed for each flight speed imposing the equilibrium between the lift force and the maximum take-off weight.
The set of points describing the airfoil is computed from an average of the tip and root airfoils, introducing therefore an additional approximation.

parameter	minimum value	maximum value	steps
plate thickness	0 mm	0.8 mm	15
flight velocity	$63\,\text{m}\,\text{s}^{-1}$	$137\,\text{m}\,\text{s}^{-1}$	10

Table 3.17: Parameter invervals chosen for the $C_{L,F}$ computation; the unspecified ones are taken from table 3.16 and 3.15.

Figure 3.43 provides the $C_{L,F}$ results, while figure 3.44 shows the ratio between the non-actuated and

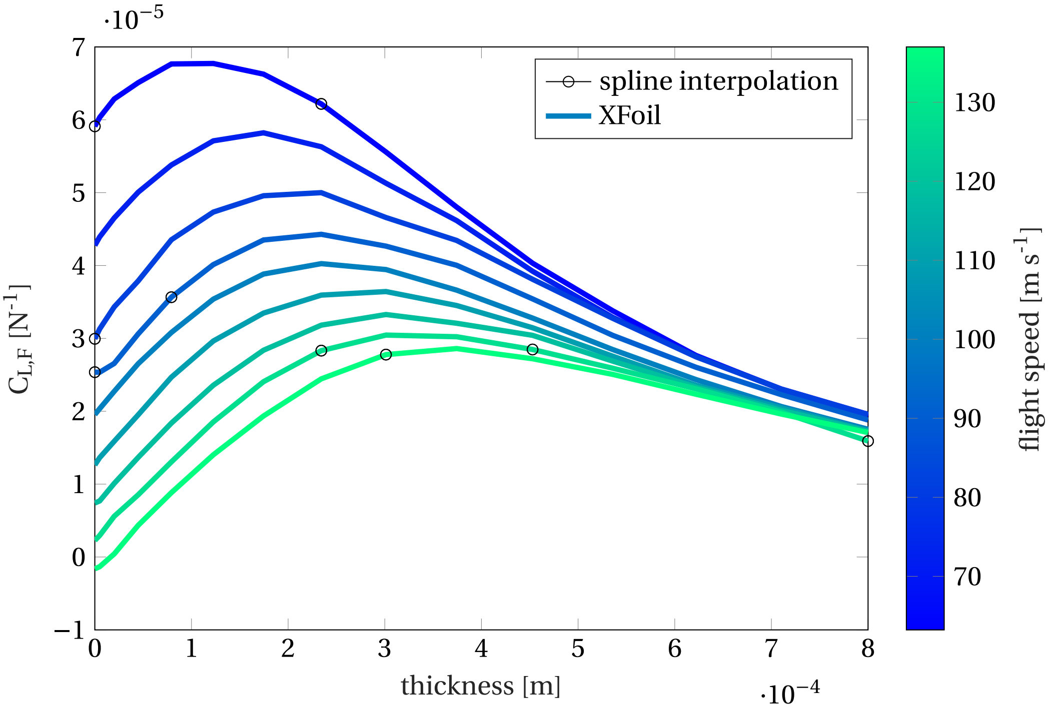

Figure 3.43: $C_{L,F}$ as function of the plate thickness, for several flight speeds, at a given altitude (7500 m), for the ATR 42-300.

actuated C_L. The “spline interpolation” mark has the same meaning of the previous case. The results in terms of C_L increase are very favourable. A C_L increase of the 16% is possible with the optimal actuator thickness and at maximum cruising speed. All the 3D effects are neglected by the very nature of the used solver.
Moreover, the use of the optimal configuration could not be possible in the real case: the optimal actuator corresponds to an aluminium plate with a thickness of about half millimeter, and a 10 cm length. This structure could be easily subject to damage, and a real case could employ a thicker structure, or some reinforcement system that could degrade the aerodynamic performances. On the positive side, doubling the thickness - and choosing therefore a sub-optimal configuration - still grants a 10% C_L increase.

Figure 3.45 shows the C_M increase: in the optimal $C_{L,F}$ conditions the C_M almost doubles. The results as a function of the altitude for a given actuation system are provided in figure 3.46. The air condition are computed in accordance with the Standard Atmosphere model. These computations take into account the change in the air density, speed of sound, viscosity, and equilibrium angle of attack, without varying the flight speed; therefore, all the used nondimensional groups and the aeroelastic coupling are corrected as function of the altitude. The $C_{L,F}(V(h), \rho(h), \alpha_{\text{eq}}(h), \text{Ma}(h), \text{Re}(h))$ shows a linear performance degradation. This phenomenon should be taken into account when sizing the actuation system since it appears to heavily with the altitude, being halved at sea level w.r.t. the cruise altitude.

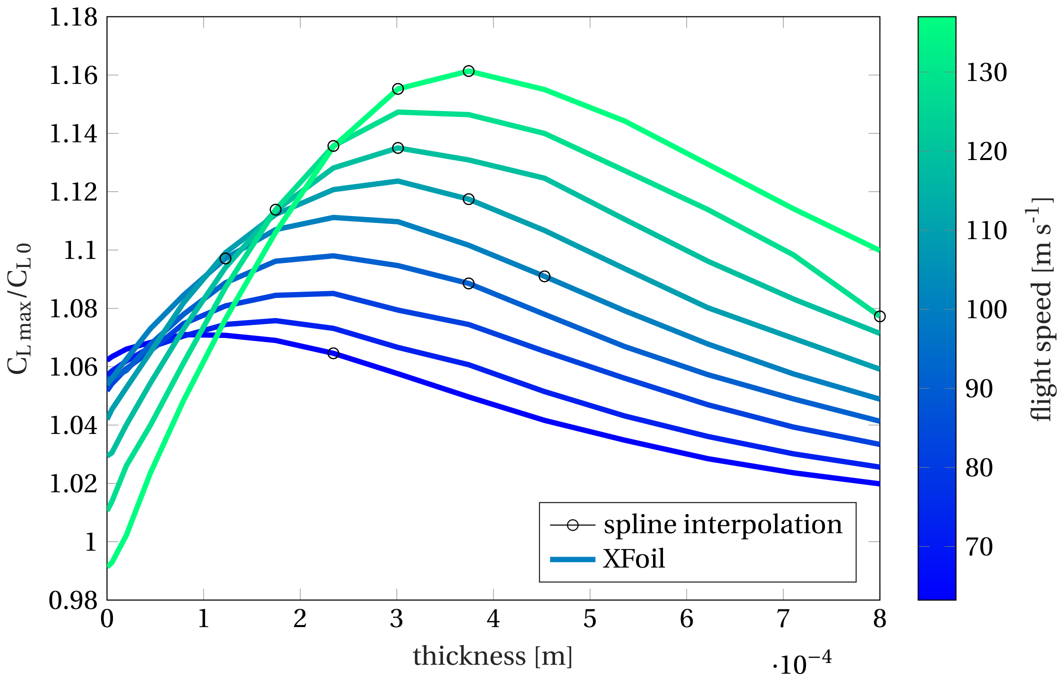

Figure 3.44: C_L increase as function of the plate thickness, at several flight velocities, at a given altitude (7500 m), for the ATR 42-300.

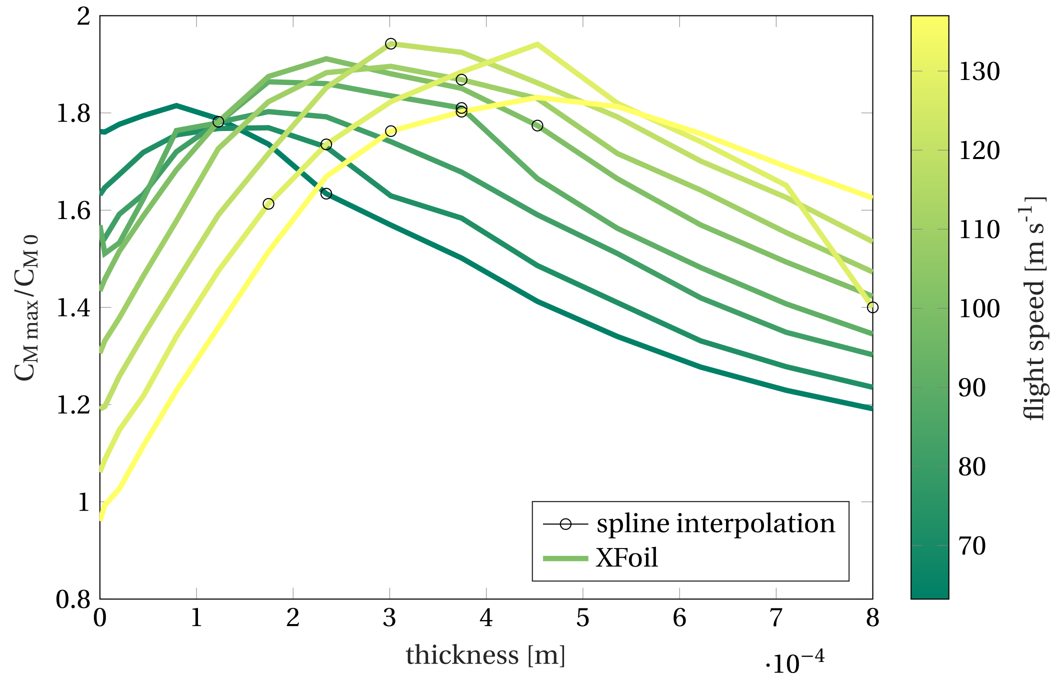

Figure 3.45: C_M increase as function of the plate thickness, at several flight velocities, at a given altitude (7500 m), for the ATR 42-300.

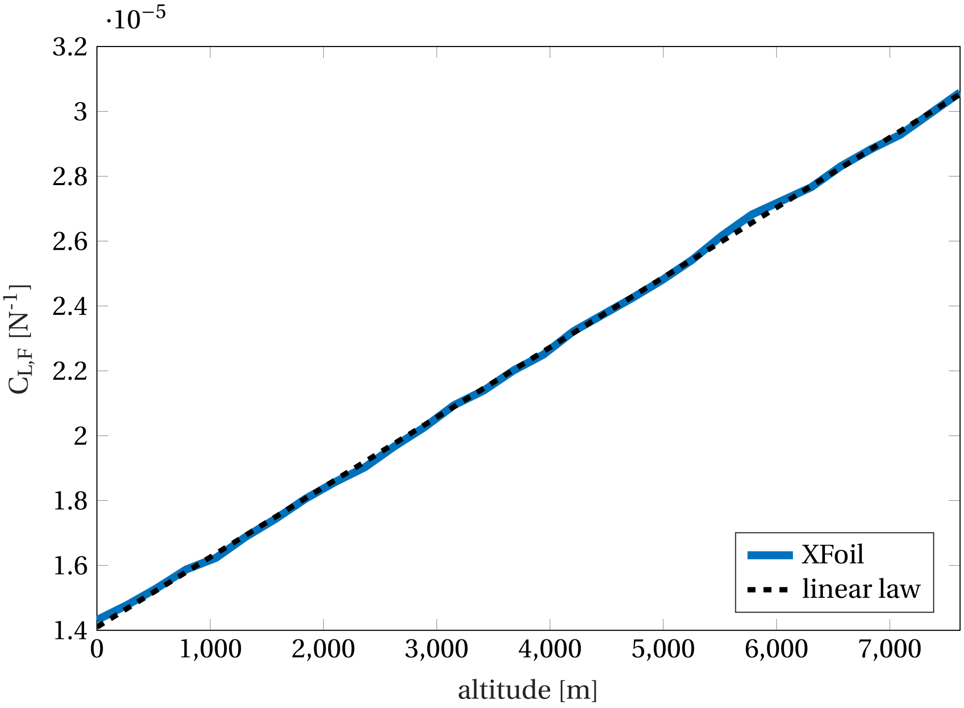

Figure 3.46: $C_{L,F}(V(h), \rho(h), \alpha_{\text{eq}}(h), \text{Ma}(h), \text{Re}(h))$ linear increase as function of the altitude for the ATR 42-300 in standard atmosphere conditions.

Chapter four

Experimental activities

4.1 Plate design and technological issues

4.1.1 Material choice

In this chapter the experimental procedures and results will be discussed and compared with numerical simulations.

The importance of a high spanwise stiffness, as opposed to a low chordwise one, was explained in section 2.2.1. This requirement suggests the use of an orthotropic material. This is achievable by laminating a composite material plate with the appropriate pre-impregnated composite fibers and sheets, in order to get a final structure with the desired properties.

Several materials have been initially considered appropriate with this objective. They are reported in table 4.1

material	utility
unidirectional carbon fiber	provides the needed strong orthotropy
glass fiber fabric	avoids damages along the carbon fiber direction
unsupported adhesive sheet	adds epoxy to engulf the fibers
supported adhesive sheet	adds epoxy and drifts the carbon fiber apart from the median line
non-stick sheet	leaves the plate Y-shaped so that it can be glued to the trailing edge

Table 4.1: Materials tested for the trailing edge plate, and reason of their choice.

The materials actually chosen for the tests reported in table 4.2.

material	acronym	name
unidirectional carbon fiber	**UCF**	Hexcel Hexply 913/CHTA/12K/5/34%
glass fiber fabric	**GFF**	SAATI Seal EE48 REM
unsupported adhesive sheet	**UAS**	3M Scotch Weld AF163-2-OST
supported adhesive sheet	**SAS**	3M Scotch Weld AF163-2U
non-stick sheet	**NSS**	Teflon

Table 4.2: Materials used for the trailing edge plate, with manufacturer and model name; the acronym is used in this chapter when referring to the specific material.

All these materials were laminated using the following procedure:

1. a set of sheets is cut with a specific orientation with the use of a template slightly bigger than the final plate,
2. the sheets are piled together in a specific order, with a Teflon sheet separating the two middle prepregs along the whole span, and for about one third of the chord,
3. the plate is inserted between two non-stick coated metal slabs and put in a press, with 2-bar pressure and at a temperature of 120°C (125°C for the glass fiber) for 1 hour, without considering the heating and cooling phases.

Various combinations of these materials have been tested during the experimental campaign, each one with its advantages and disadvantages. Hereafter a list of the chosen lamination sequences is reported using the abbreviations specified in table 4.2; the $X°$ superscript indicates a particular warp or fiber orientation; the non-stick sheet is not a layer extended over the complete plate, but only on a restricted part.

1. **UCF - GFF - NSS - UCF**: this configuration is the only one produced with an asymmetry with respect to the Teflon layer; the asymmetric configuration has been abandoned because it caused a strong plate asymmetry with respect to the bifurcation,
2. **GFF - UCF - NSS - UCF - GFF**: the external fabric causes the glass fibers to work axially when the plate is bended chordwise, considerably contributing to the stiffness,
3. **UCF - $\mathbf{GFF^{45°}}$ - T - $\mathbf{GFF^{45°}}$ - UCF**: the internal use of the glass fiber decreases the chordwise stiffness with respect to the previous configuration,
4. **UCF - NSS - UCF**: this configuration shows the lowest chordwise stiffness, but also a high fragility and risk of being damaged,
5. **UCF - SAS - NSS - SAS - UCF**: the use of supported resin sheets between the carbon fiber layers increases considerably both the spanwise and chordwise stiffness, and greatly reduces the brittleness; the high resin quantity may cause fiber bowing if precautions are not taken,
6. **UCF - UAS - NSS - UAS - UCF**: this configuration shows a stiffness higher than the carbon fiber alone, but lower than the previous one, retaining its increased resistance to damage; as the previous configuration, special precautions are needed owing to the high quantity of unsupported resin.

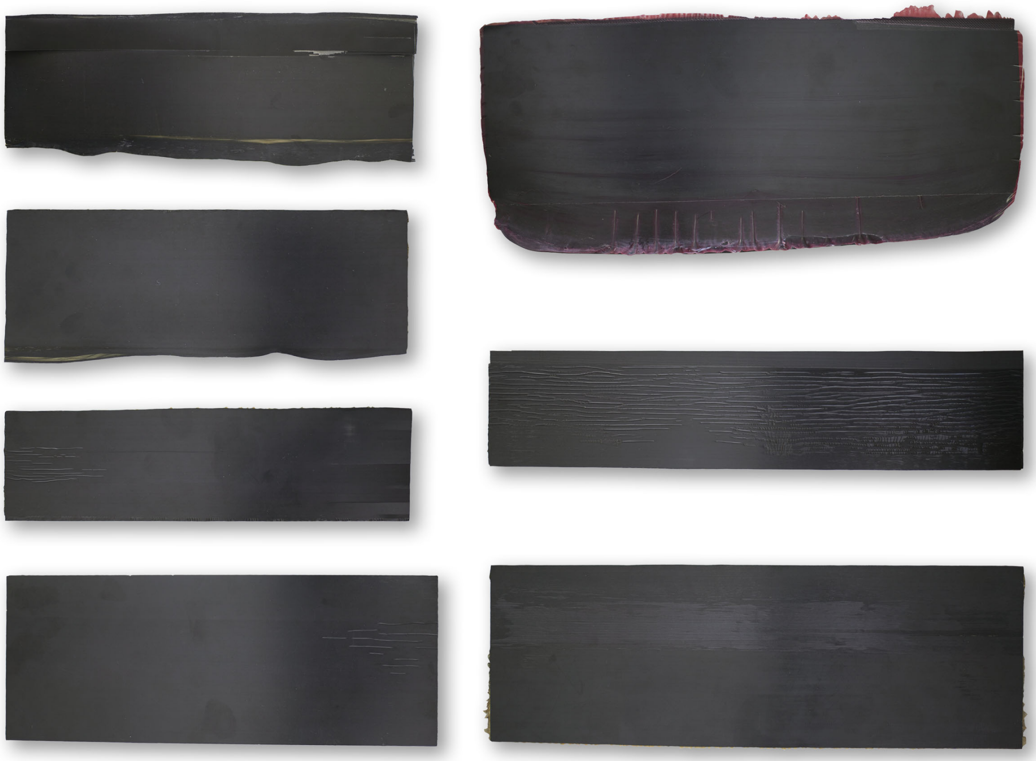

Figure 4.1: Results of lamination tests aimed at choosing the right production procedure; defects should be noticed.

Figure 4.1 shows different tests of lamination, many of them have visible defects, such as fiber warping, or fractures.

Figures 4.2, 4.3, and 4.4 show a zoom of the defects, with a brief description for each case.

Two configurations are chosen for the aerodynamic testing: configuration n° 4, characterized by a very low chordwise stiffness but high risk of damage during the installation, and configuration n° 6, more stiff but also more robust and less prone to damage.

4.1.2 Manufacturing

The flatness of the needed surface allows the use of a press (figure 4.5) instead of an autoclave, simplifying considerably the production process. The production of the carbon-only laminates reveals some critical points. The structure can easily be broken along the fiber, especially where the two carbon pre-impregnated layers split up. Furthermore, the greater height in the section with the Teflon caused an inferior surface pressure on the rest of the laminate, resulting in a coarse superficial texture (figure 4.2b is an example). A solution for both problems is the use of two rubber sheets above and below the metal plates, redistributing evenly the press force. An exploded view of the needed configuration is shown in figure 4.6.

The Scotch Weld and carbon pre-impregnated laminate is characterized by a large amount of resin. As anticipated, precautions are needed to prevent the pressure from moving the resin outside the

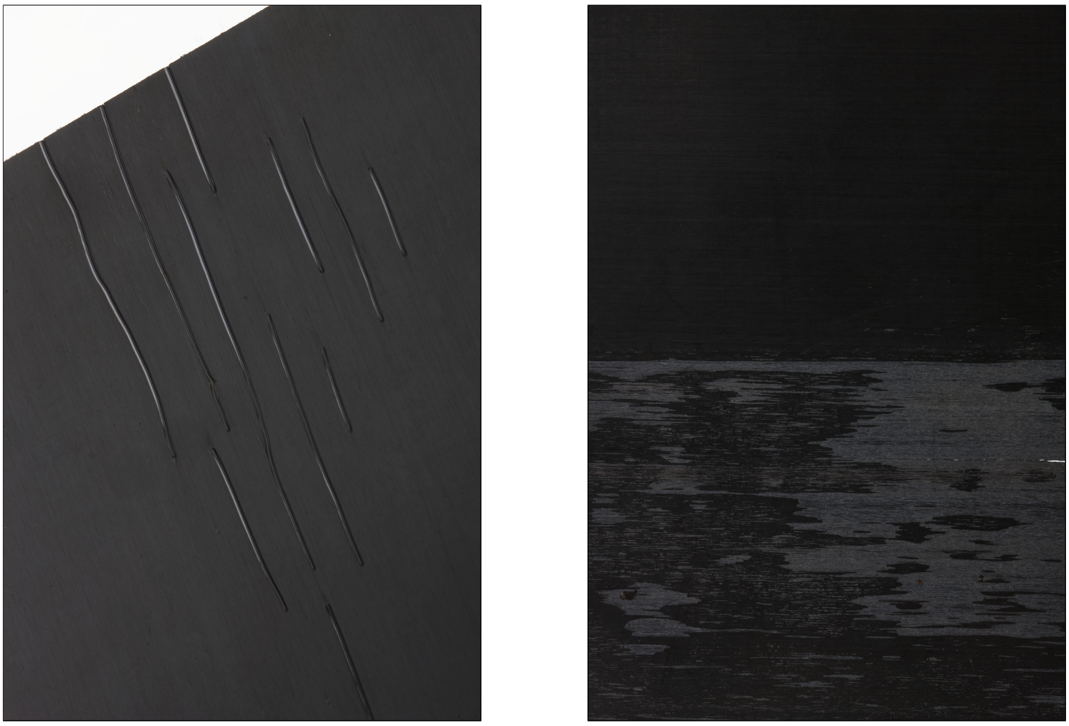

(a) Surface grooves caused by the initial use of a non-stick plastic sheet instead of release-film treated metal plates; trapped air bubbles caused the sheet ripples, that in turn caused these defects.

(b) Carbon-fiber plate laminated without the use of rubber sheets redistributing the press force. The rough part did not present the intermediate Teflon sheet.

Figure 4.2: Two examples of surface defects: surface grooves (a), rough surface (b).

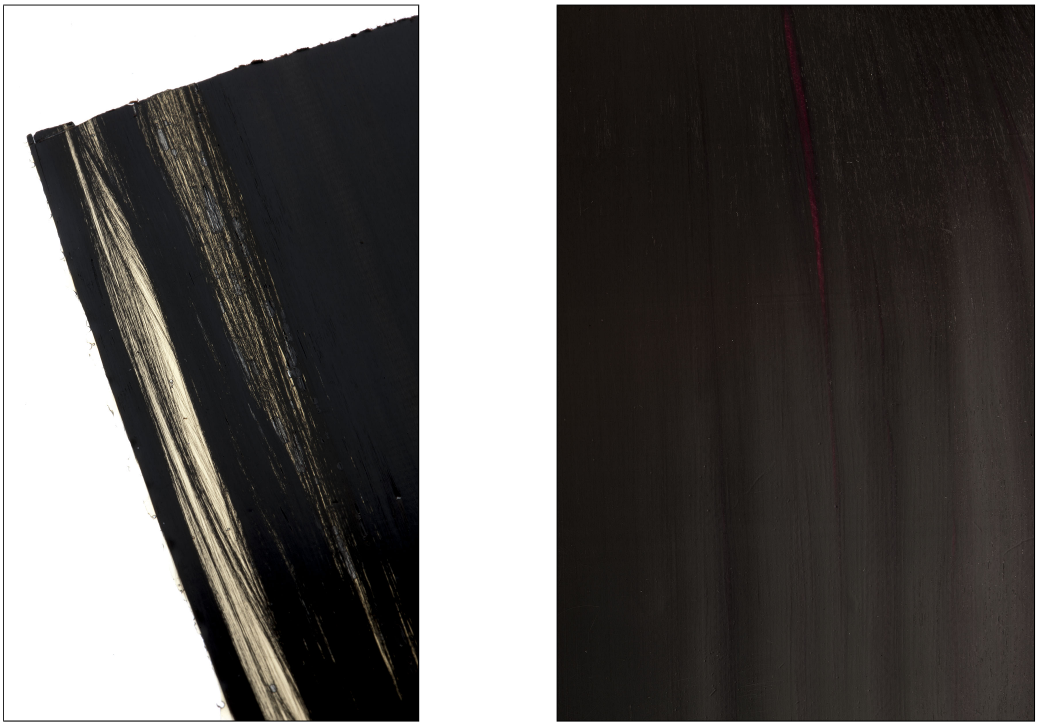

(a) Carbon fiber spread; this effect is local, and can be fixed by oversizing the plate and then cutting it.

(b) Fiber curvature and separation caused by the additional resin without the use of lateral dams.

Figure 4.3: Two examples of fiber spreading and curving.

laminate, bowing the fibers (figure 4.3b) and causing a nonuniform thickness of the plate. The adoption of lateral dams stops the resin from moving. These dams are made of polymerized plates with the same lamination sequence, so that they can be thick enough to stop the resin overflow without interfering with the laminate pressing. Figure 4.7 shows its exploded view.

The following step is to decide the MFC arrangement on the plate and to mount the system on the airfoil.
The first actuator configuration is made with the carbon fiber and Scotch Weld laminate, with a length slightly higher than that of the MFC. Table 4.3 summarizes its characteristics.

lamination sequence	*UCF - UAS - NSS - UAS - UCF*
total length	8.5 cm
cantilevered length	3.5 cm
thickness	0.6 mm
MFC type	M-2814-P1
MFC number	3
MFC conditions	partially worn-out
disposition	one-sided
MFC gluing	non-technical adhesive tape
mounting angle	0

Table 4.3: Specifications of the actuation system for the first wind-tunnel experimental campaign.

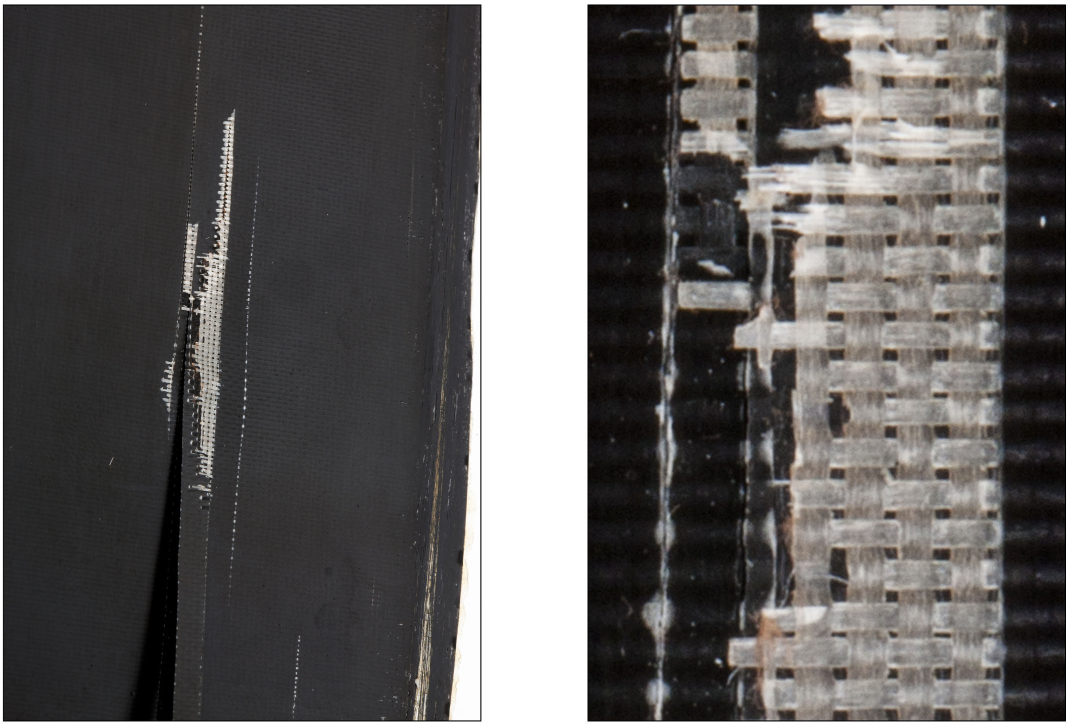

(a) Crack of a carbon and glass fiber laminate, in correspondence with bifurcation.

(b) Zoom on the crack; notice the glass fibers.

Figure 4.4: Example of a crack in correspondence with the laminate thickness variation, due to the lack of a press force redistribution system.

Figure 4.5: Press used at DAER (Dipartimento di Scienze e Tecnologie Aerospaziali, Politecnico di Milano) material laboratory to laminate the plates.

Figure 4.6: Exploded views of all the components needed in the lamination process of the only-carbon plate; top to bottom: two rubber sheets, nonstick metal plate, carbon prepreg, Teflon sheet, carbon prepreg, nonstick metal plate, two rubber sheets.

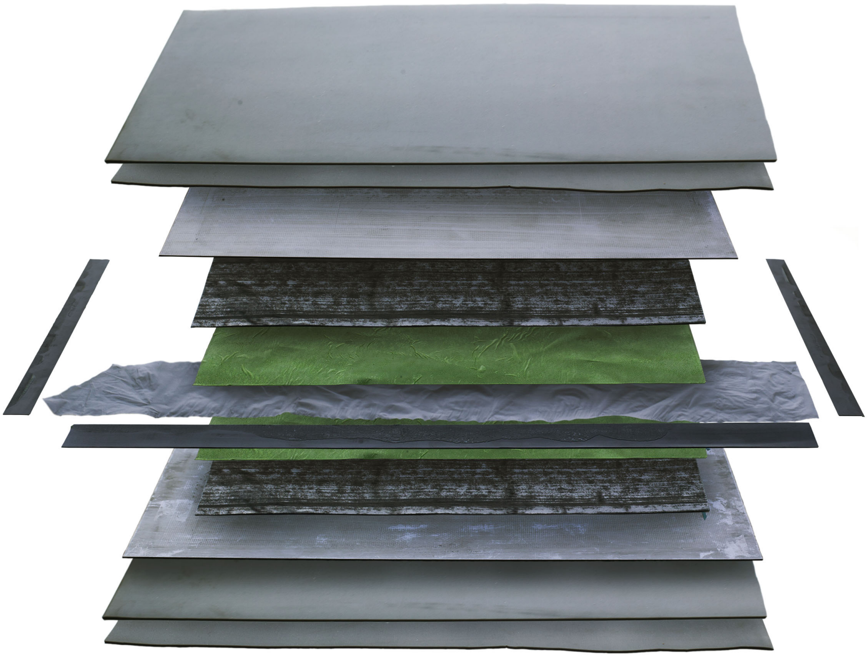

Figure 4.7: Exploded views of all the components needed in the lamination process of the resin-reinforced plate; top to bottom: two rubber sheets, nonstick metal plates, Scotch Weld, carbon prepreg, Teflon sheet (with three lateral dams), Scotch Weld, carbon prepreg, nonstick metal plate, two rubber sheets.

Figure 4.8: Photo of the first actuation system; the first actuator from the left has different overall size, since it is an earlier model, but the actuation force and the active section size are identical to the other two.

Figure 4.8 shows the actuated laminated setup. The electrical setup is characterized by 0.225 mm enameled wires, isolated from the carbon surface and covered with electrical tape. The wires are separated from each other, even if they have the same polarity. This allows us to monitor the functioning of each actuator.

The second configuration is characterized by a longer and more compliant structure (figure 4.9), equipped with bigger MFCs (see table 4.4). The carbon-only configuration was chosen in this case.

lamination sequence	*UCF - NSS - UCF*
total length	12 cm
cantilevered length	6.5 cm
thickness	0.2 mm
MFC type	M-8528-P1
MFC number	2
MFC conditions	as new
disposition	one-sided
MFC gluing	non-technical adhesive tape
mounting angle	13°

Table 4.4: Specifications of the actuation system for the second wind-tunnel experimental campaign.

The non-technical adhesive tape was chosen over more efficient solutions since it assured the reusability of the actuators. The high mounting angle is due to the one-sided disposition of the MFCs, making the upper side of the plate bifurcation stiffer. The electrical setup has no significant differences from the previous one.

The last tested configuration, figure 4.10, is more similar to the cases studied in the numerical parametric study. The surface is highly compliant and short (carbon-only lamination). Table 4.5 summarises its properties.

Figure 4.9: Second actuation system; it is significantly longer than the other ones.

Figure 4.10: Third actuation system; the high quantity of wires caused an uneven surface in the first half of the plate.

lamination sequence	*UCF - NSS - UCF*
total length	7.8 cm
cantilevered length	3 cm
thickness	0.2 mm
MFC type	M-2814-P1
MFC number	6
MFC conditions	new
disposition	one-sided
MFC gluing	non-technical adhesive tape
mounting angle	5°

Table 4.5: Specifications of the actuation system for the third wind-tunnel experimental campaign.

The original choice was to have a two-sided disposition. The presence of only one high-voltage output channel prevented its implementation, since this setup needed two independent high-voltage output channels.

The electrical setup is slightly different from the previous ones. All the wires connected to the positive end are placed over the electrical tape isolating them from the carbon. They are connected into a unique wire. The wires connected to the negative end are placed over a second layer of electrical tape. They end into a unique wire too.

This setup simplified the installation, since only two wires come out from the airfoil, but made impossible to check the proper functioning of each MFC after the mounting.

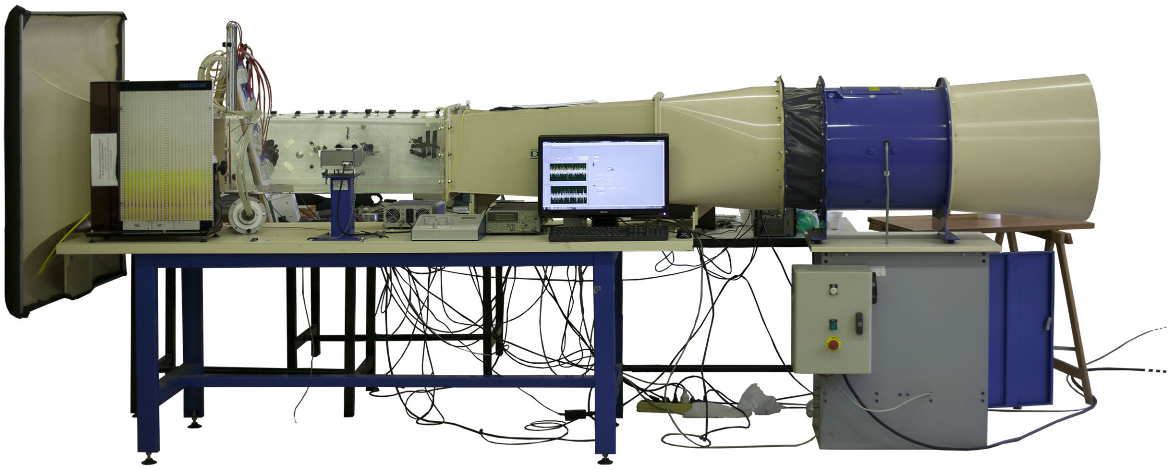

Figure 4.11: Deltalab EA103 open-circuit wind tunnel used for aerodynamic the experiments.

4.2 Aerodynamic experiments

4.2.1 General setup

The aerodynamic experimentation is performed in the Politecnico di Milano's Deltalab EA103 wind tunnel (figure 4.11). Table 4.6 shows its characteristics and operative ranges.

model	Deltalab EA103
type	open circuit
test chamber type	closed
total size (h×w×l)	$2.1 \times 1.1 \times 4\,\mathrm{m}$
test chamber size (h×w×l)	$30 \times 30 \times 100\,\mathrm{cm}$
nominal velocity range	$0 \div 45\,\mathrm{m\,s^{-1}}$
fan operation type	suction
maximum fan power	3 kW
total weight	350 kg

Table 4.6: Specifications of the wind tunnel used for experimentation.

The airfoil configurations all consist of a NACA 63(.2)-218 with a small end plate on each side and the different actuated plates at the trailing edge. The total span of the airfoil, including the end plates, is 29.3 cm, 7 mm less than the width of the test section.

The velocity measurements obtained through an upstream Pitot-static tube.

The measures concerning the second setup (table 4.4) were completed with a endpoint deformation measure. The deformation of the endpoint of the actuated plate were measured by postprocessing the images acquired with a Canon 1DS Mark-I camera, fixed on a tripod, and equipped with a 50 mm lens with an additional macro ring. The focus plane was aligned with the lateral end of the plate.

The large displacement of the actuator prevents the use of correlation-based methods. The develop-

ment of an automated photo analysis software to measure the displacement is considered too time-consuming if it must be sufficiently generic to work with every photo without a complicated ad-hoc tuning, owing to the non-optimal illumination of the scene and to the irregular plexiglass surface. A more efficient method in this case seems to measure the displacement with the integrated ruler tool provided by Photoshop, after a proper calibration.
The length-to-pixel ratio is measured taking a photograph of a sheet of graph paper placed on the camera focal plane, where the deflection is measured. 80 measures were taken, and a normal distribution of values was assumed. The expected value of the distribution was taken as pixel-to-length ratio: it results of $43.0817 \pm 1.3749\,\mathrm{px\,mm^{-1}}$, or, conversely, $2.3212 \cdot 10^{-2} \pm 1.4831 \cdot 10^{-3}\,\mathrm{mm\,px^{-1}}$.

All the numerical simulations computed in this chapter use both viscous and compressible corrections. The Reynolds and Mach numbers are estimated with the standard air model at sea level and the wind velocity.

4.2.2 Wind tunnel results and model validation

4.2.2.1 First setup

The first tested system is the one shown in figure 4.8 whose specifications are reported in table 4.3. This configuration revealed ineffective. The relatively high thickness of the laminted plate caused a too high bending stiffness that combined with the non-optimal state of the MFC and the suboptimal gluing. The complete system caused a maximum endpoint deflection of $\approx 0.12\,\mathrm{mm}$, as measured by a laser meter. A quick wind tunnel test revealed no measurable effects in term of C_L variations.

4.2.2.2 Second setup

The second system, see table 4.4 for the specifications, showed significant results. The system installed in the test section is shown in figure 4.12. Figure 4.13 allows a first qualitative appreciation of the effect. The overall structure has two important differences from what has been modelled numerically, cfr. chapter 2: the first one is the very high compliance of the plate in the airfoil trailing edge, where the actuated plate is attached, the second one is the suboptimal gluing of the MFC.

The local high compliance is due to the actuation structure: there is a small portion of the plate where the two carbon fiber plies are neither glued to the airfoil nor laminated together. This small gap actually acts as a concentrated torsional spring connecting the airfoil and the plate. The gluing is particularly critical since the actuators work with displacements of microns, and a small lash can significantly reduce performances. This performance degradation can be modelled with a coefficient in the range $[0,1]$ multiplying the actuation force.

A direct measurement of these two parameters, the concentrated spring K_t, and the performance degradation E, is impractical. The chosen approach is to identify the parameters by comparing experiments and calculations.
The first experimental campaign with the actuator described in table 4.4 is at a fixed angle, varying the actuation voltage, at different velocities. The precise test conditions are expressed in table 4.7.

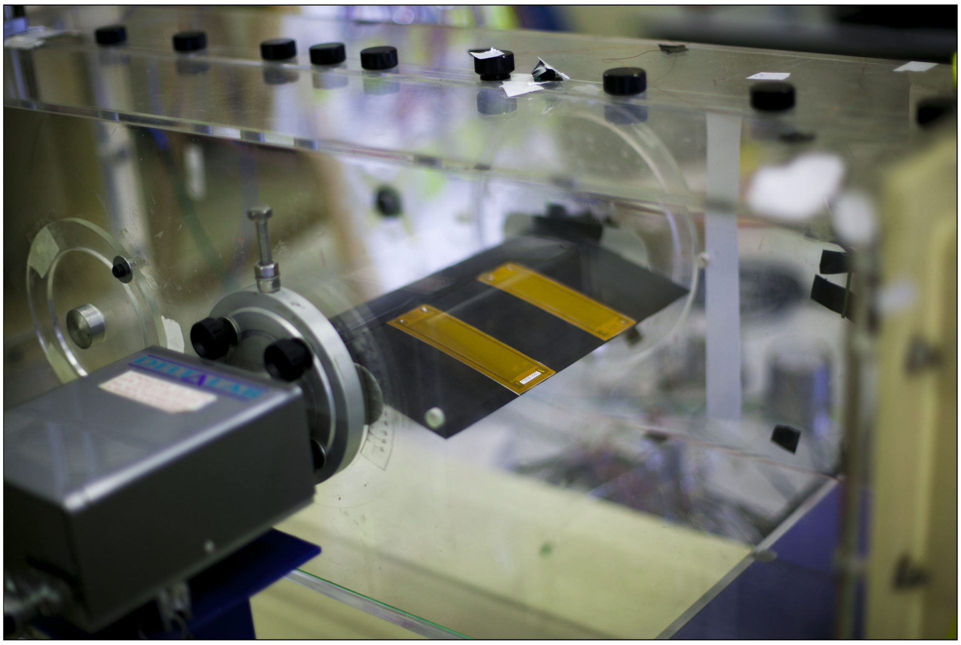

Figure 4.12: Second actuation setup mounted in the wind tunnel for testing.

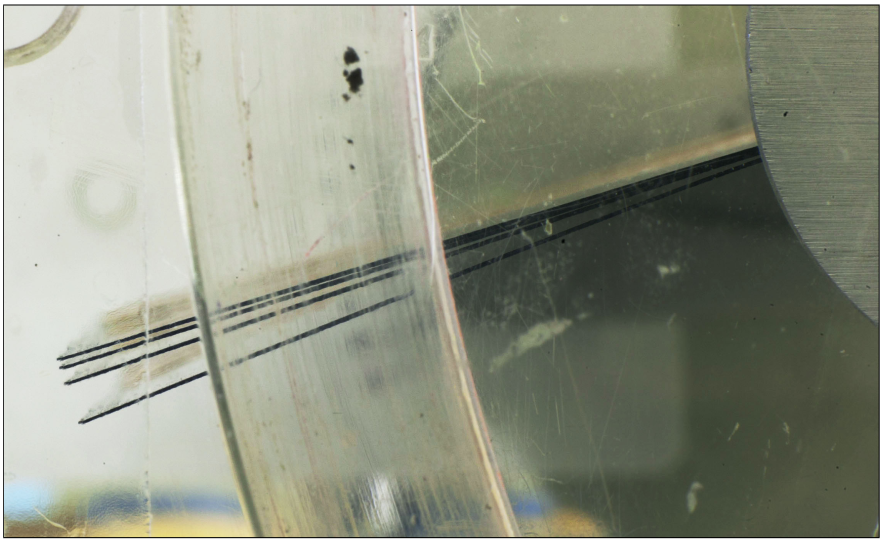

Figure 4.13: Superposition of several frames associated with different actuation voltages and zero velocity; the four position of the plate from top to bottom correspond to −500, 0, 500, and 1500 V, respectively.

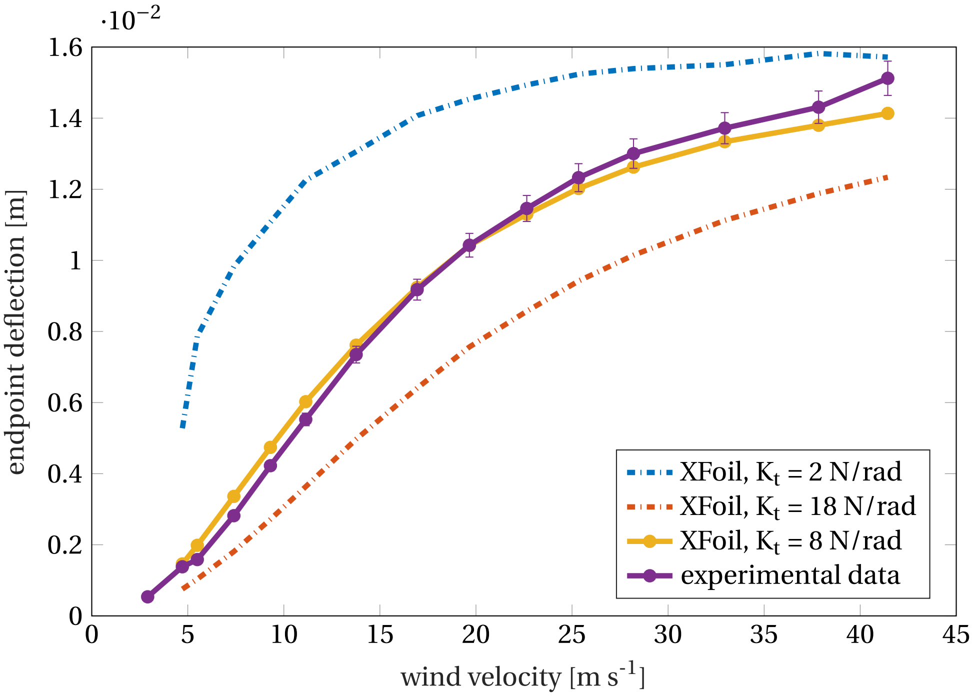

Figure 4.14: Endpoint deformation as a function of the velocity for the two simulation with guessed concentrated spring coefficients and the final one, compared with the experimental data; the error bars represent the uncertainty due to the pixel-to-length conversion.

actuation setup	2
angle of attack	3°
wind velocities	$0 \rightarrow 44\,\mathrm{m\,s^{-1}}$
actuation voltages	−500, 0, +500, +1500 V
employed instruments	balance, actuation monitor, camera

Table 4.7: Setup of the first experimental campaign with the M-8528-P1 actuated trailing edge plate.

The torsional spring stiffness is computed fitting the measured 0 V deformations with the computed ones. The correct parameter value is sought using a bisection method, with $2\,\mathrm{N\,rad^{-1}}$ and $18\,\mathrm{N\,rad^{-1}}$ as initial guesses for the parameters and the mean of the difference between the computed and measured deformation as the function to be annihilated. A value of $8\,\mathrm{N\,rad^{-1}}$ is a good approximation of the optimal parameter value, as figure 4.14 reveals. The resulting C_L values are in good agreement as well, despite the parameter was evaluated with respect to the endpoint deflection. Figure 4.14 shows the computed and measured deformation values. The resulting C_L values (figure 4.15) were revealed to be reasonably consistent, despite not being part of the objective function.

The choice of using only 0 V deformations was motivated by the need to estimate a second free parameter, the performance-degradation one. The present choice of the voltage allowed us to decouple the two effects.

The actuation efficacy is estimated by comparison among the computed and measured $C_{L,F}$. The used method is again the bisection, with starting points 0 and 1; this time the objective function is the $C_{L,F}$. A value of 0.5 seems to provide a good matching between numerical and experimental data.

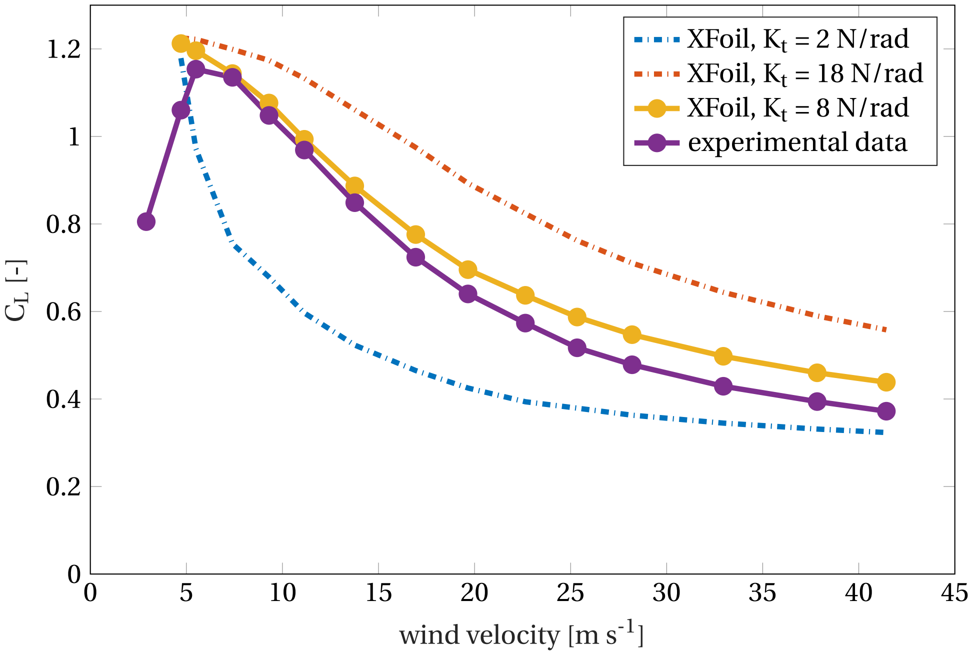

Figure 4.15: C_L as a function of the velocity for the starting K_t guesses, the final K_t, compared with the experimental data.

Figure 4.16 shows the comparison of experimental and numerical results, the latter obtained with the estimated parameters. There is a fundamental difference at low speed, due to XFoil convergence difficulties linked to the low Reynolds number.

In order to have a more intuitive grasp on the effective C_L variation, figure 4.17 shows the different C_Ls, and figure 4.18 the relative C_L increase, defined as:

$$C_{L\text{incr}} = \frac{C_{L1500\text{V}} - C_{L0\text{V}}}{C_{L0\text{V}}} \, . \tag{4.1}$$

Figure 4.19 shows the C_L as a function of the endpoint deflection. The isovelocity lines show a standard behaviour in the $0 \div 32\,\text{m}\,\text{s}^{-1}$ range, then there is a deflection reversal for higher velocities, followed by a C_L reversal for even higher velocities. We define a new derivative as:

$$d_{,F} \overset{\text{def}}{=} \frac{\partial d}{\partial F} \, , \tag{4.2}$$

where d is the endpoint deflection. It is now possible to see more clearly the aforementioned reversal phenomenon: figure 4.20 shows how the reversal with respect to the deflection and the C_L happens at different velocities.
Another visualization of the actuation and its inversion is given by figure 4.21, where the deflection is compared directly with the lift, and an intersection between the curves at different voltage can easily be noticed.
Figure 4.22 shows the inversion phenomenon captured by camera and visually edited for clarity by plotting several frames overlapped.

Up to now, the analysis has been carried out only for the C_L. The other two integral nondimensional parameters typically used in the description of the performance of an airfoil are the C_D and C_M.
Figure 4.23 shows the C_D variation. The C_M acquisitions are compared with the XFoil results in fig-

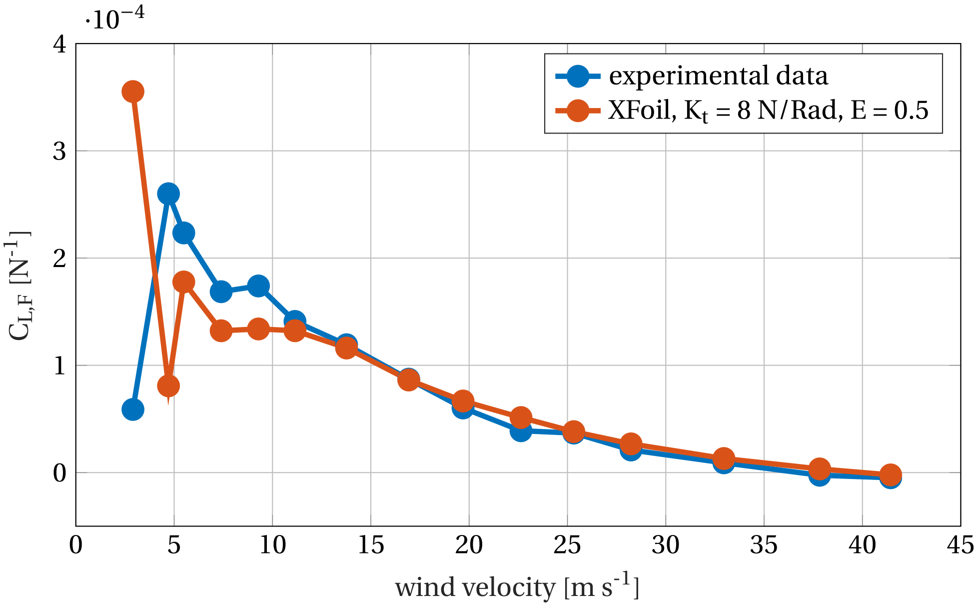

Figure 4.16: Measured and computed $C_{L,F}$ for with a 3° angle of attack.

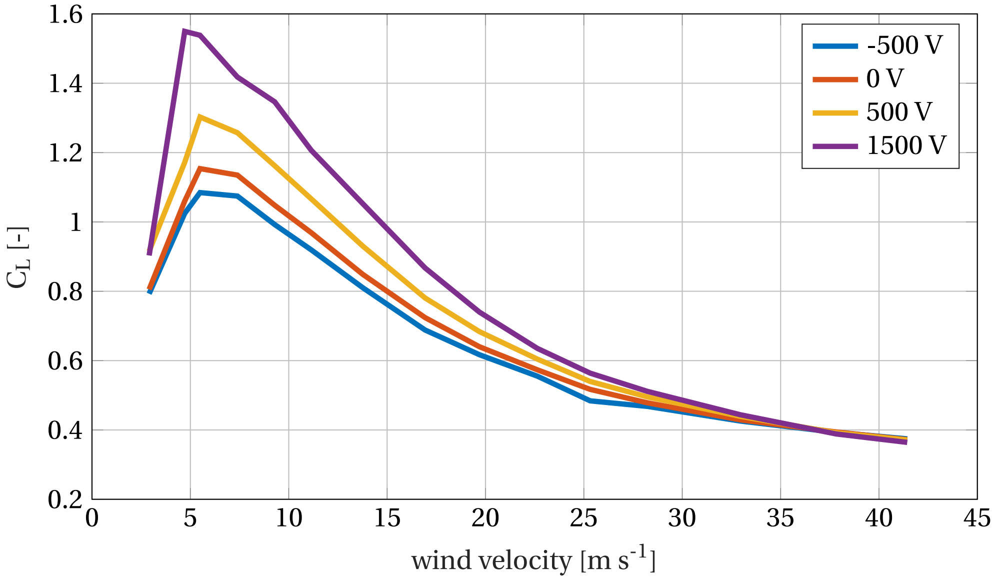

Figure 4.17: Measured C_L for different voltages at different velocities, and a 3° angle of attack.

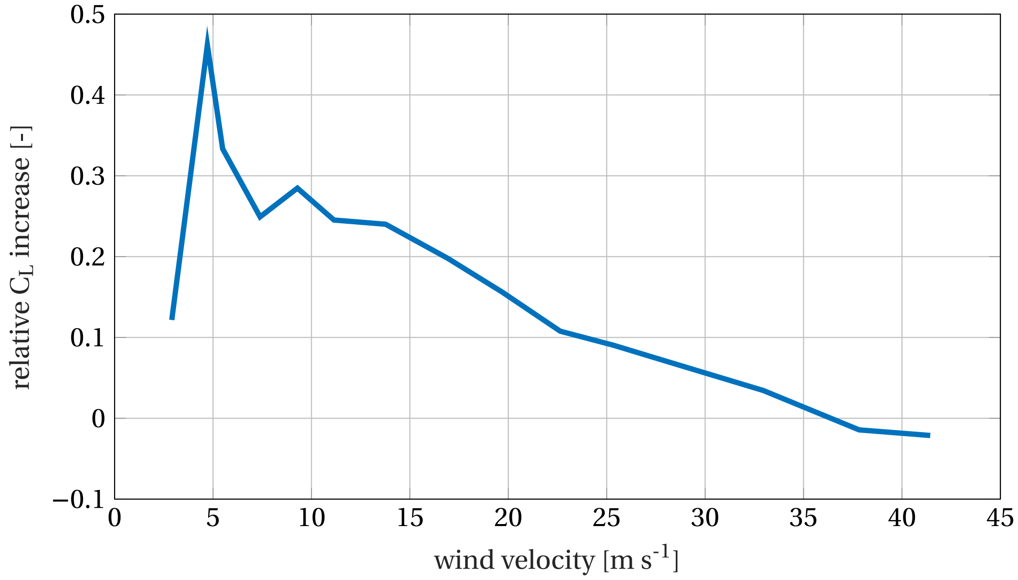

Figure 4.18: Relative C_L increase ($C_{L\text{incr}}$) as a function of the velocity, for $\alpha = 3°$.

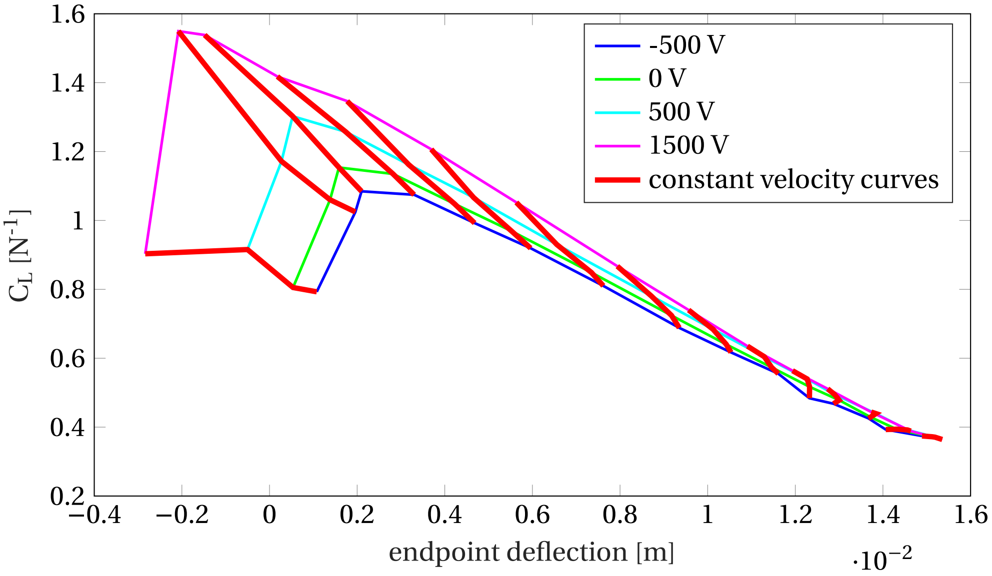

Figure 4.19: Measured C_L as a function of the deflection, for four different voltages, and 3° angle of attack.

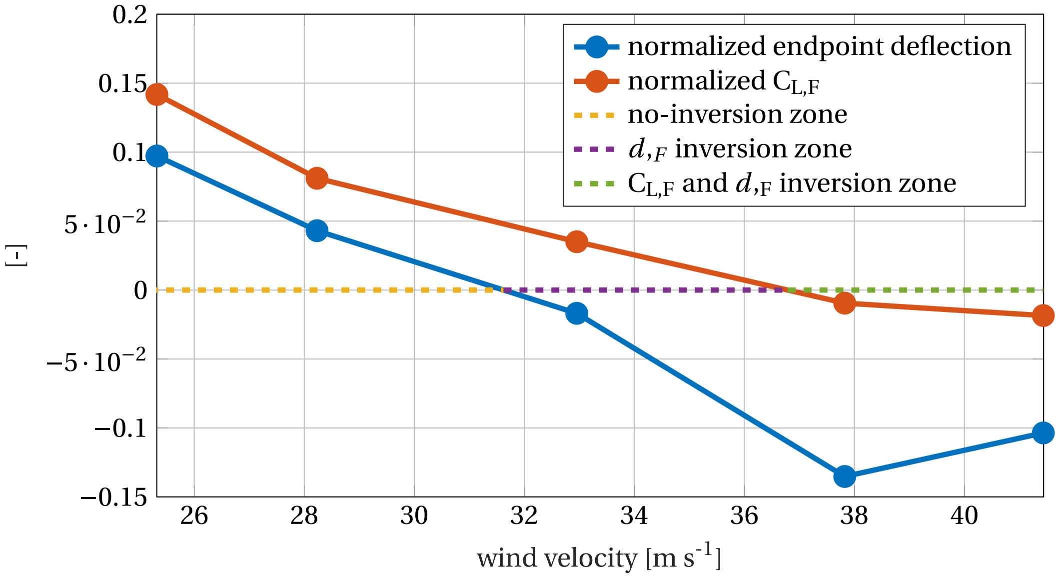

Figure 4.20: Values of the derivative of the endpoint deflection and C_L with respect to the actuation force, normalized over their highest value; the velocity when the normalizations equal 1 is not present since the graph shows only the $26 \div 41\,\mathrm{m\,s^{-1}}$ velocity range; notice how they cross the axis at different velocities.

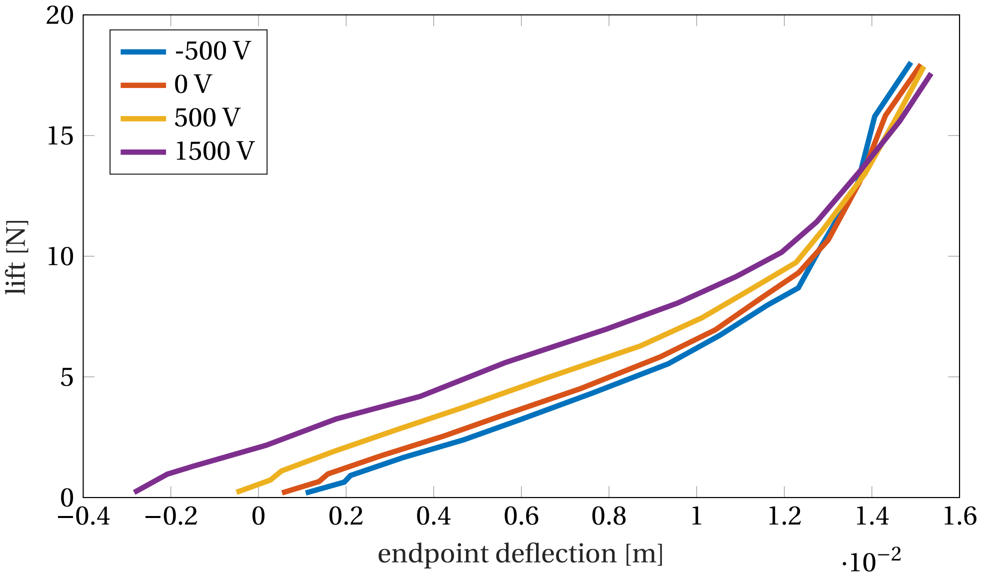

Figure 4.21: Lift as a function of the endpoint deflection, obtained increasing the velocity, for different actuation voltages.

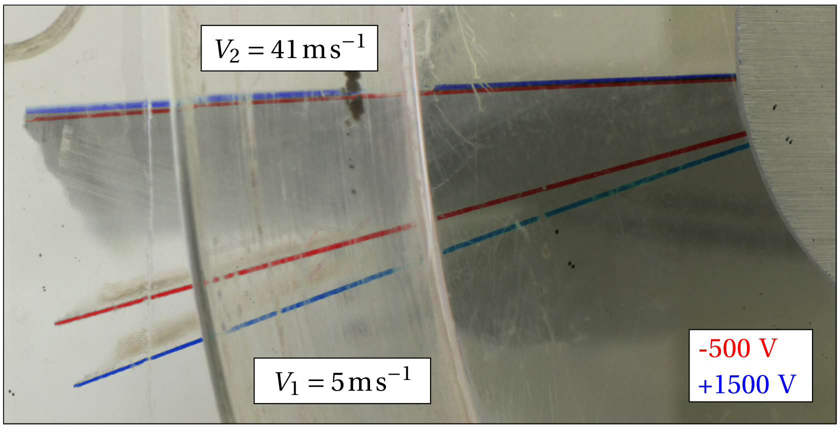

Figure 4.22: Superposition of four photographs taken for two different actuation voltages (-500 V and 1500 V) and two different velocities ($5\,\mathrm{m\,s^{-1}}$ and $41\,\mathrm{m\,s^{-1}}$); notice the actuation reversal.

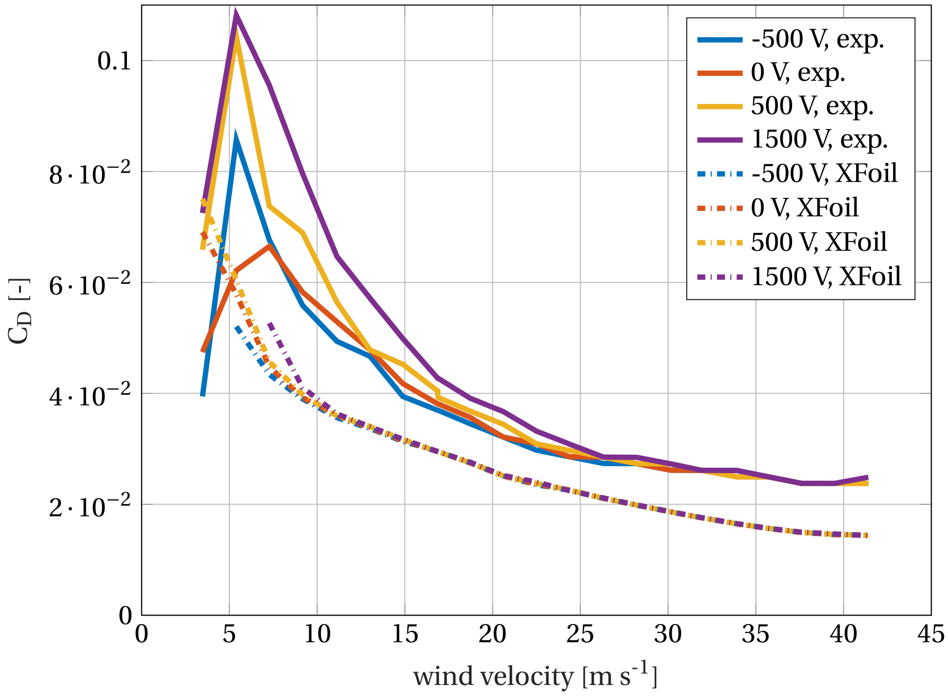

Figure 4.23: C_D behaviour as a function of the speed for different input voltages; experimental and numerical results.

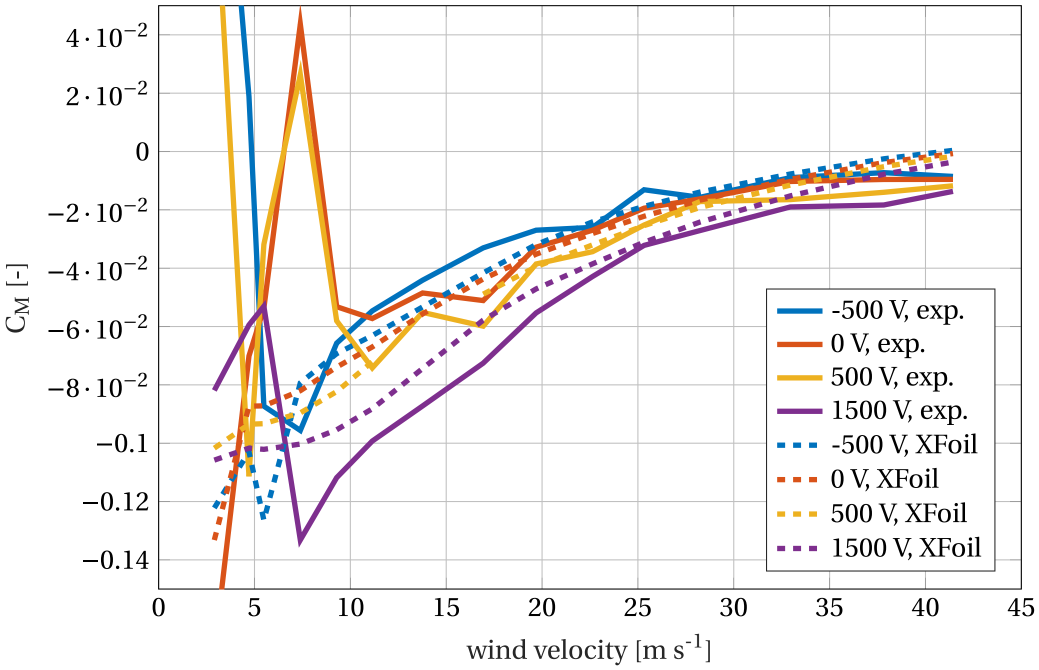

Figure 4.24: C_M behaviour as a function of the speed for different input voltages for an airfoil at 3° incidence. Experimental and numerical results are compared. Under $10\,\mathrm{m\,s^{-1}}$ the results are very inaccurate.

ure 4.24. The experimental results are corrected by $C_L\,l_d$, where l_d is the distance between the airfoil sting and the quarter-chord.

The second acquisition campaign was done with the same actuation setup, but a different angle of attack (table 4.8).

actuation setup	2
angle of attack	0°
wind velocities	$0 \rightarrow 44\,\mathrm{m\,s^{-1}}$
actuation voltages	-500, 0, $+500$, $+1500$ V
employed instruments	balance, actuation monitor

Table 4.8: Setup of the second experimental campaign with the M-8528-P1 actuated trailing-edge plate.

Since the actuation has not changed from the previous case, and the only difference is in the flight condition, the same K_t and E correction values should be taken. The resulting $C_{L,F}$ is shown in figure 4.25. The $C_{L,F}$ XFoil data point is not reported for the first velocity for lack of convergence.
The actuation behaviour is similar to that observed in the previous case.

Another $C_{L,F}$ analysis varying the velocity has been done with a −3° angle of attack; for completeness, the employed parameters are reported in table 4.9.

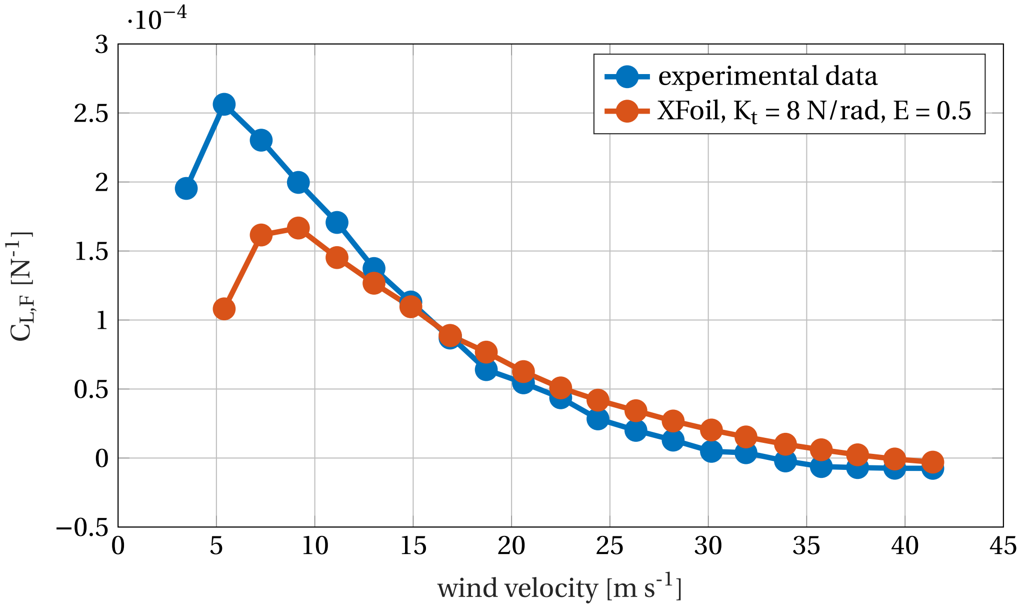

Figure 4.25: Measured and computed $C_{L,F}$ as a function of speed for a 0° angle of attack.

actuation setup	2
angle of attack	$-3°$
wind velocities	$0 \rightarrow 44\,\mathrm{m\,s^{-1}}$
actuation voltages	$-500, 0, +500, +1500\,\mathrm{V}$
employed instruments	balance, actuation monitor

Table 4.9: Setup of the third experimental campaign with the M-8528-P1 actuated trailing edge plate.

The resulting $C_{L,F}$ is reported in figure 4.26. The measured and computed data differ substantially at very low speeds, as the previous cases, but in this set of computations, XFoil seems to overestimate the $C_{L,F}$. Figure 4.27 shows the three different $C_{L,F}$ curves superimposed. It appears that the $C_{L,F}$ does not depend strongly on the angle of attack, at least for low α, especially at high speed. This is consistent with the results of the parametric analysis reported in the previous chapter.

Table 4.10 shows the parameters employed for the last set of measures with the present airfoil configuration.

actuation setup	2
angle of attack	$0 \rightarrow 13°$
wind velocity	$23.87\,\mathrm{m\,s^{-1}}$
actuation voltages	$-500, 0, +500, +1500\,\mathrm{V}$
employed instruments	balance, actuation monitor

Table 4.10: Setup of the fourth experimental campaign with the M-8528-P1 actuated trailing edge plate.

In this measures the wind velocity was held fixed and the angle of attack varied. The results are shown in figure 4.28. It should be noticed that the angle is set by hand and measured visually by the wind-

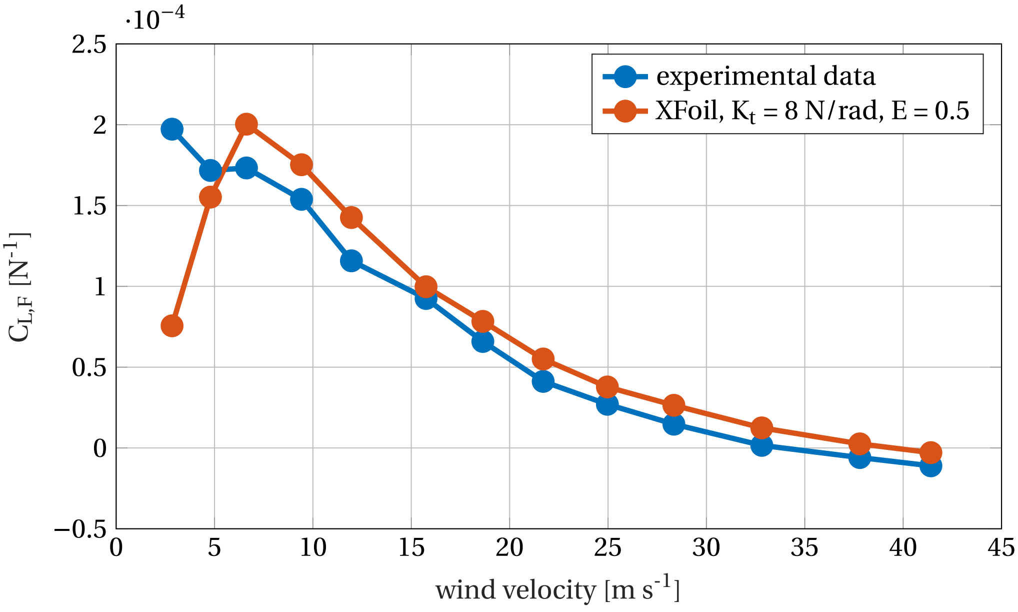

Figure 4.26: Measured and computed $C_{L,F}$ for with a −3° angle of attack as a function of speed; comparison between numerical results and experiments.

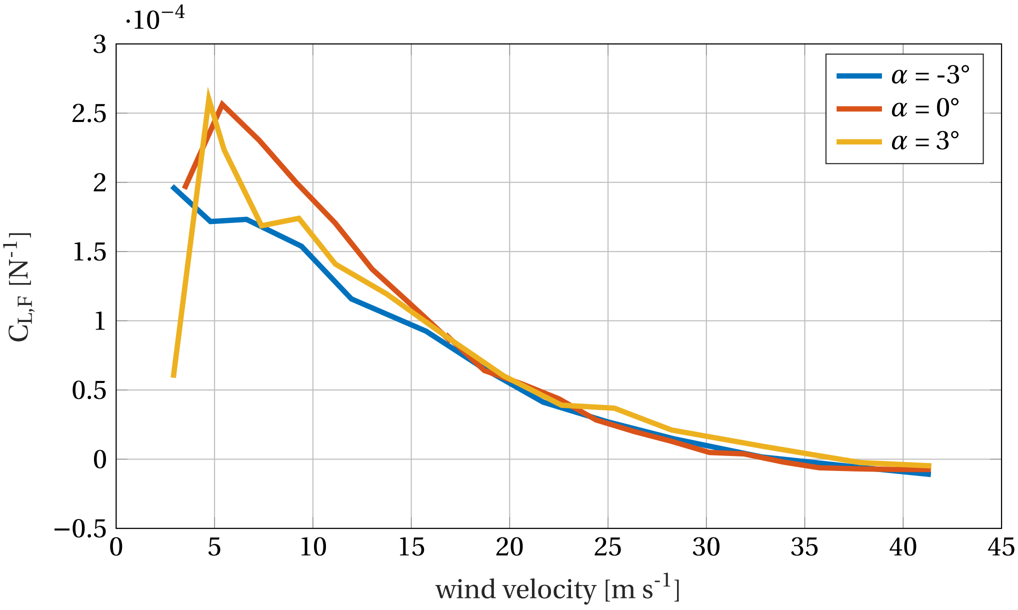

Figure 4.27: Comparison of the wind speed-$C_{L,F}$ curves obtained in the 3 experimental campaigns with the M-8528-P1 actuated trailing edge plate for 3 different angles of attack.

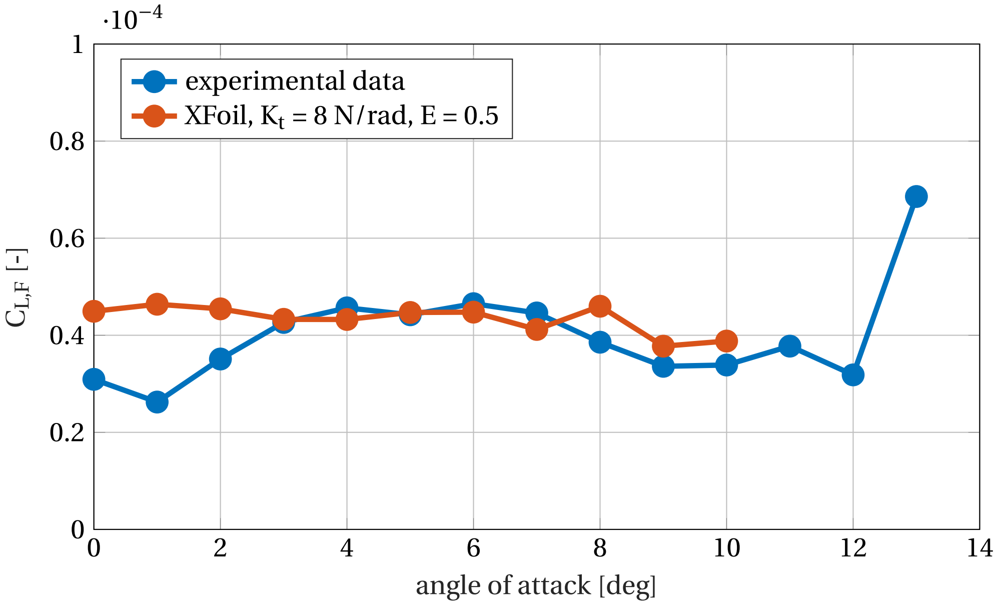

Figure 4.28: Measured and computed $C_{L,F}$ as a function of the angle of attack, at 23.87 m s^{-1}; for α = 11°, 12°, and 13° XFoil did not converge.

tunnel user, therefore the angle accuracy is limited by the user ability. There is a marked difference between the computed and measured results at low angles. The reason is probably an high shape factor on a significant portion of the airfoil. This phenomenon is discussed more extensively in section 3.1.3.

At high angles of attack the steadiness hypothesis is no longer valid, and the actuation system starts to oscillate vehemently, compromising its structural integrity. This is a phenomenon that should be taken into account: this kind of actuation could present heavy criticalities outside its operative range if proper reinforcements and safety measures are not employed.

4.2.2.3 Third setup

The last experimental setup used is specified in table 4.5. The actuated plate is shown in figure 4.10. Figure 4.29 shows the mounted setup.

Owing to the quite short trailing edge plate and to the consequent small displacement, its endpoint acquisition by the camera was rather difficult. The displacement data is necessary to compute the two free parameters (K_t and E), and without it their estimation can be problematic. For this reason, the torsional stiffness K_t was estimated by matching the C_L curve shape of a chosen data set by trial and error, while E was found by comparison between $C_{L,F}$ curves.

Table 4.11 provides the configurations of the three set of measures.

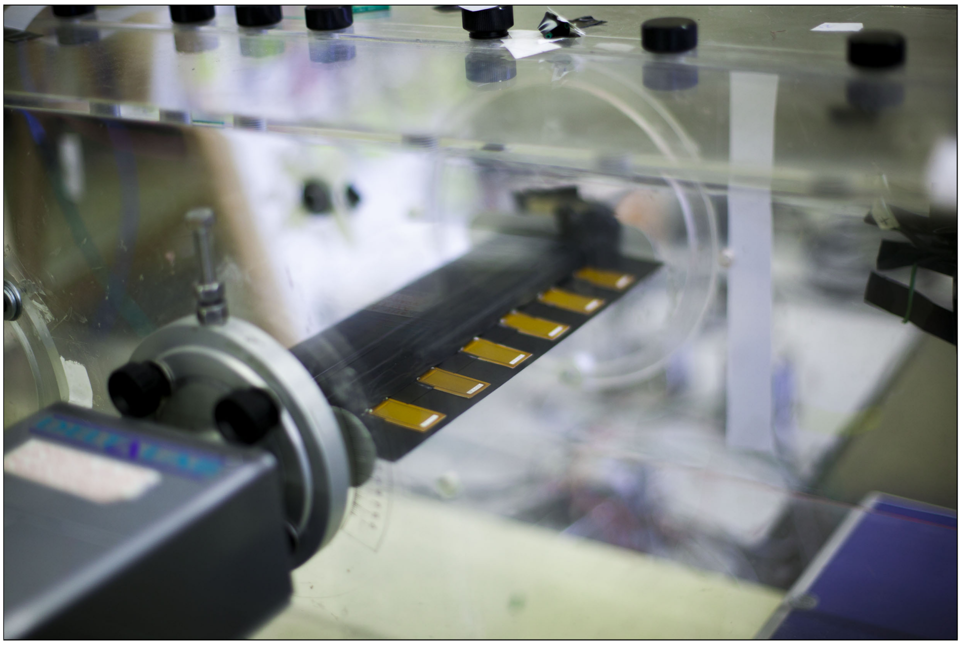

Figure 4.29: Third setup mounted in the wind tunnel for testing.

actuation setup	3
angle of attack	3, 0, −3°
wind velocities	$0 \rightarrow 44\,\mathrm{m\,s^{-1}}$
actuation voltages	−500, 0, +500, +1500 V
employed instruments	balance, actuation monitor

Table 4.11: Data corresponding to the fifth, sixth, and seventh experimental campaigns, at $\alpha = 3°$, 0°, and −3° respectively.

The results for $\alpha = 3°$ are shown in figure 4.30. The estimated parameters are $K_t = 20\,\mathrm{N\,rad^{-1}}$ and $E = 0.15$. K_t is higher then the previous setup, meaning a better gluing at the airfoil trailing edge, but the E is significantly lower. This could be due to a disconnection of one or more actuators. As previously explained, the electrical wiring of this setup prevented the user from checking each one of the MFCs in the final configuration. The numerical and experimental results are reasonably similar, with the exception of the low speed part, and a $C_{L,F}$ decrease overestimation at high speeds.

Varying the angle of attack from 3° to 0° and keeping the estimated K_t and E values we get the results shown in figure 4.31.

The last experimental campaign ($\alpha = -3°$) is the least consistent with the XFoil computation (figure 4.32). In this case both the overall behaviour and magnitude of the effect do not agree with the experimental results. A comparison of the three simulations (figure 4.33) and the three experimental results (figure 4.34) can give a better understanding of this discrepancy. The three XFoil simulations behave more consistently, with a small difference between the three angles of attack at moderate-to-high speeds. The measures instead show a drastic difference, with the curve corresponding to the lowest angle of attack being vertically translated by roughly $-0.5\,\mathrm{N^{-1}}$ if compared with the other two.

While the $C_{L,F}$ is a useful tool to describe and model this kind of actuation, it gives little insight to

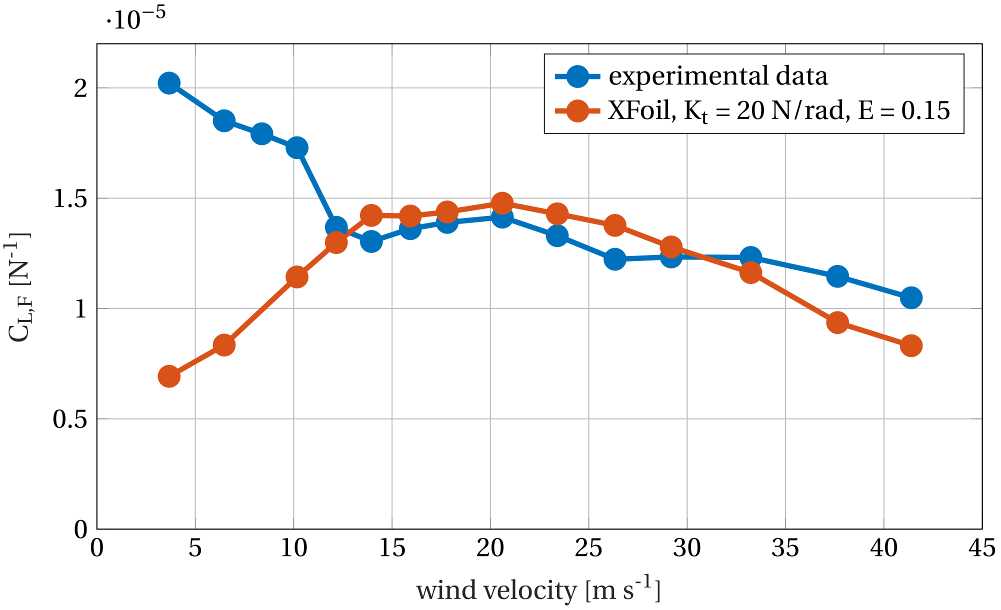

Figure 4.30: Measured and computed $C_{L,F}$ as a function of wind speed for with a 3° angle of attack; missing points in the red curve are due to lack of convergence of XFoil.

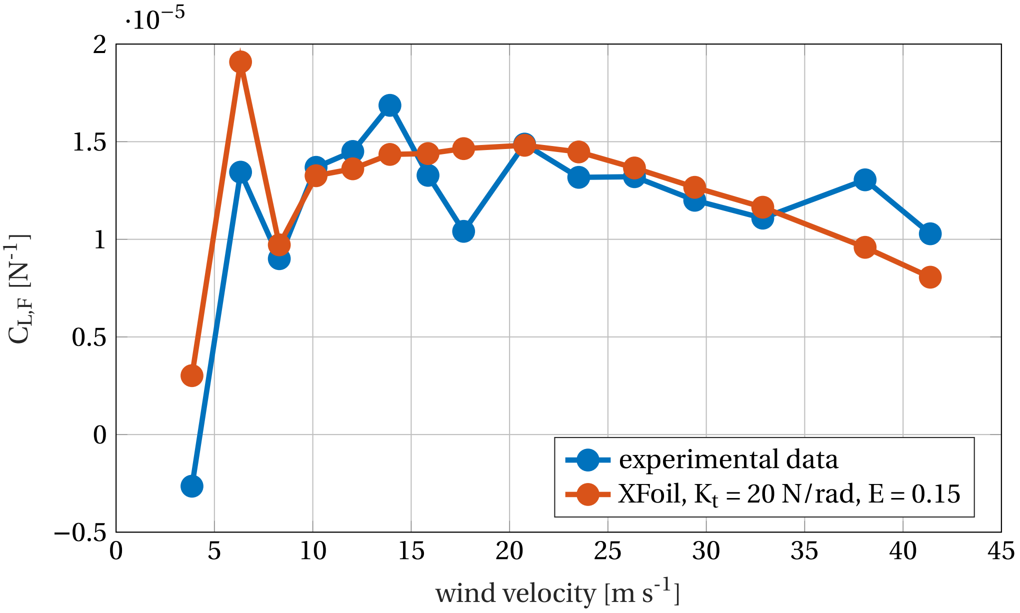

Figure 4.31: Measured and computed $C_{L,F}$ as a function of wind speed for a 0° angle of attack.

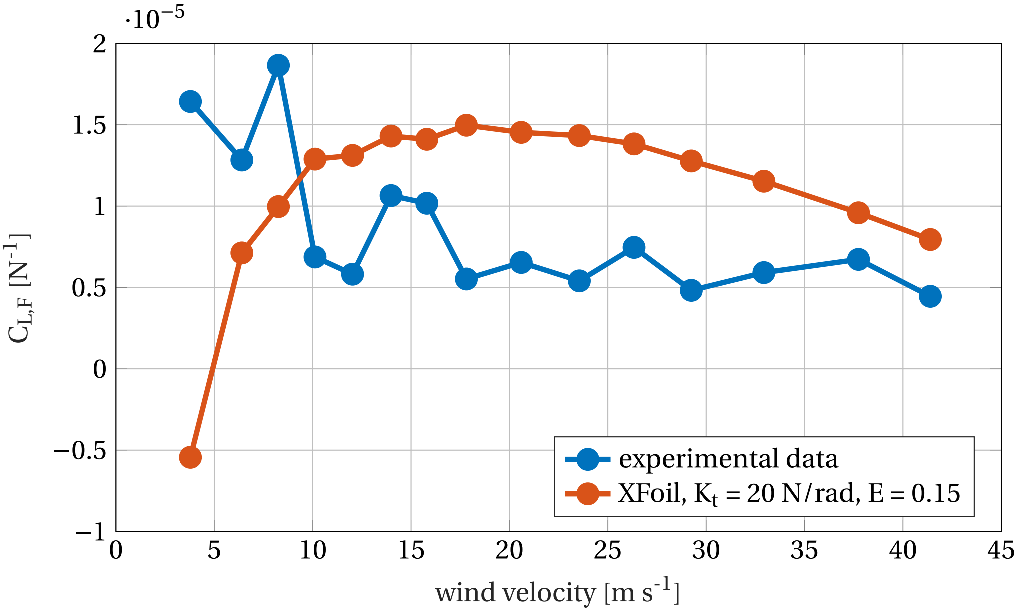

Figure 4.32: Measured and computed $C_{L,F}$ as a function of wind speed for a $-3°$ angle of attack.

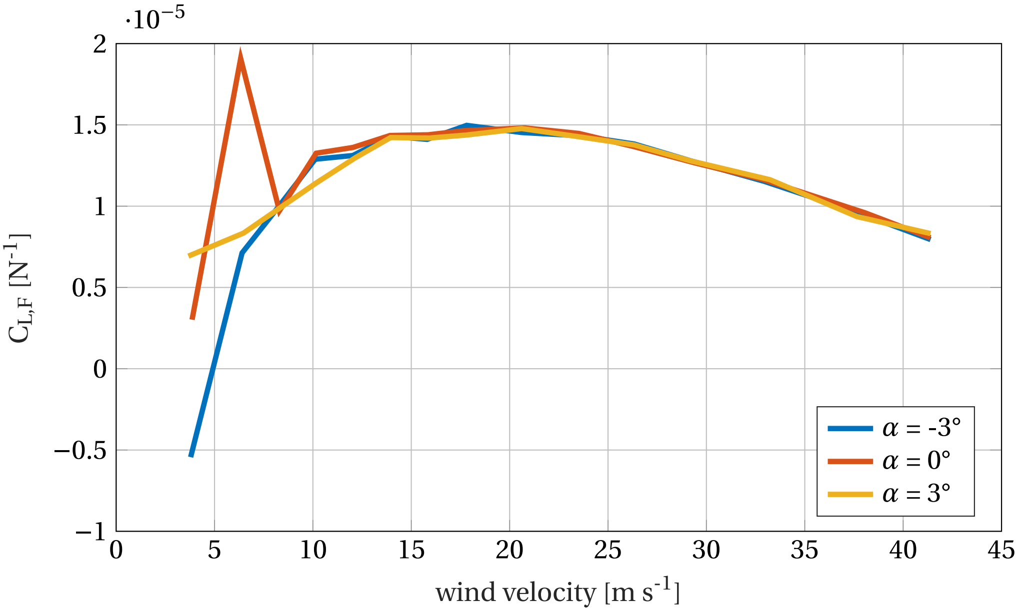

Figure 4.33: Comparison of the wind speed-$C_{L,F}$ curves obtained by the XFoil simulations for the M-2814-P1 actuated setup for 3 different angles of attack.

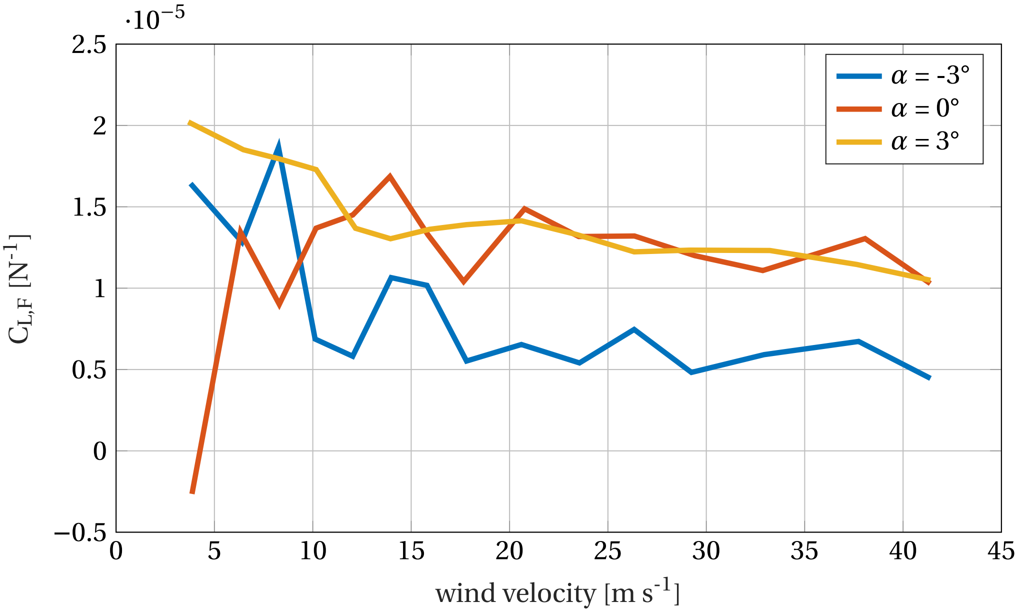

Figure 4.34: Comparison of the wind speed-$C_{L,F}$ curves obtained by experiments for the M-2814-P1 actuated setup for 3 different angles of attack.

the reader about the actual C_L variation. The relative increment of C_L, defined in formula (4.1), is depicted in figure 4.35. At low velocities the increase can be up to the 20%, while for most of the tested velocities the value is around 7% for $\alpha = 0°$ and 3% for $\alpha = 3°$.

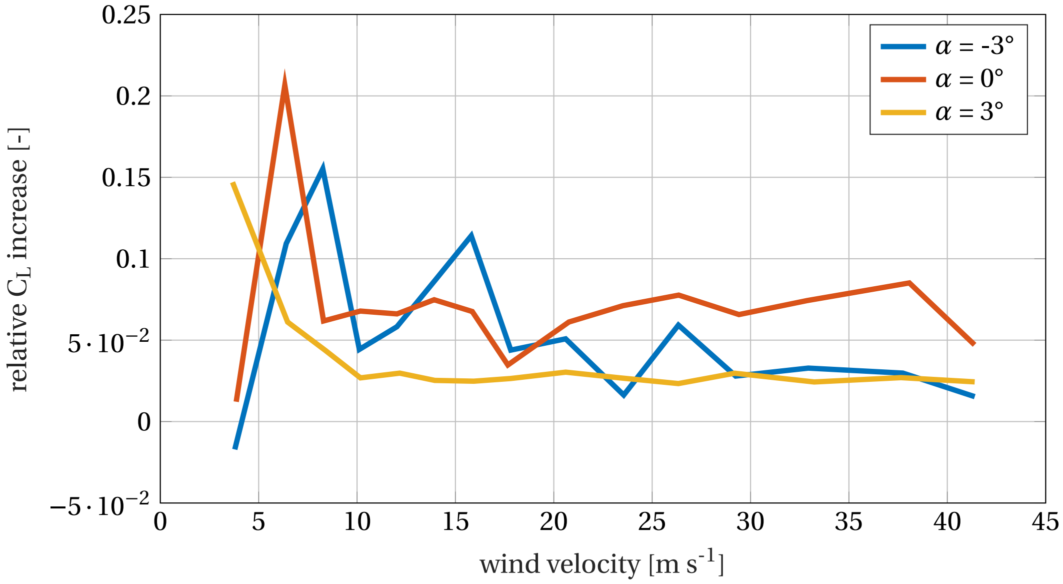

Figure 4.35: Relative C_L increase for the M-2814-P1 actuated setup as a function of wind speed for three different angles of attack.

Chapter five

Conclusion

5.1 Results discussion

This work describes the steady behaviour of compliant MFC-actuated plates mounted on the airfoil trailing edge.
The numerical results show that the actuation behaviour can be modelled with simple laws, providing a good starting point to explore the parameter space when searching for optimal configurations in the preliminary design. When considering the optimum thickness for a given length, the scaling law describing the sensitivity of the lift coefficient to the actuation force in the inviscid case can be summarised as:

$$\tilde{C}_{L,F} = e^{K+(K_t+K_{Et}E)\,t}\, l^{K_l} \cos\alpha\, \tilde{\mathcal{E}}_c\,, \tag{5.1}$$

where

$$\tilde{\mathcal{E}}_c = \begin{cases} Q\, V^{Q_V}\, l^{Q_l} & l > (1+P)\, l_c(V)\,, \\ \dfrac{1}{1+G\, V^{G_V}\, l^{G_l}} & l < (1+P)\, l_c(V)\,, \end{cases} \tag{5.2}$$

and K, K_t, K_{Et}, K_l, Q, Q_V, Q_l, G, G_V, G_l are constant values, t is the actuated plate thickness and l is its length, E is its Young modulus, α is the angle of attack of the airfoil, P a positive value adjusting the application range of the scaling laws, and $l_c(V)$ a particular length defined in section 3.2.
This simple scaling law will be particularly useful in software where the primary goal is a fast evaluation the actuation effects without the use of an aerodynamic solver.
Viscous effects are less predictable and more involved, but some observations are in order:

1. for turbulent boundary layer the $C_{L,F}$ decreases linearly as function of the mean displacement thickness measured on the actuated plate, when varying the angle of attack,
2. an apparent actuator shortening, function of the Reynolds number, appears to be a simple but effective method to take into account the boundary layer effects,
3. high shape factors of the boundary layer velocity profile over the actuated plate cause the $C_{L,F}$ to drop, especially at low Reynolds numbers.

The real case analysis provided very promising results; the C_L increases for the chosen general aviation aircraft, a Piper PA 28 161 Warrior II, reach values up to the 45%. The C_L increases for a regional

airliner, the ATR 42-300, show values up to the 16%.
The experimental campaign highlighted the importance of very flexible trailing edge plates if there are significant constraints on the total actuation force, e.g. a limited number of MFCs. The plate production procedure can be particularly critical, since high flexibility often implies high risk of damage. The wind tunnel tests showed good accordance with the numerical model, and predicted phenomena such as the actuation reversal where actually observed in the experiments. Actuation reversal, as well as the high vibration level at high angles of attack, can be very critical for the safety of this kind of morphing actuators, and deserve a deeper investigation.
The MFC installation is rather simple, since no mechanical system is needed, and their small dimension: this means that they can be easily used in already-produced designs, as section 3.3 suggests.

5.2 Future developments

This work lays the foundations for different future developments.
Since the code allows to easily manipulate the structural parameters of the trailing edge plate and the MFC properties, the most immediate development is an optimization of the structural parameters for a target flight condition, rather than a general analysis of the parameter space. A complete analysis should take also into account the system robustness to off design conditions. A global optimization in the complete parameter space with the appropriate constraints can be useful, especially if the ultimate goal is the development of an actuation system for a real flight machine (e.g. a MAV).

Another future development could be the implementation of an unsteady model. MFC actuators have a very high bandwidth, with a frequency response of 750 kHz; this property makes them very interesting with respect to active control implementations, both to reduce vibrations and to increase performance [32]. This will require a different aerodynamic solver, since XFoil cannot handle unsteady aerodynamics.

Estratto in italiano

In questo scritto si presenta un'analisi di un particolare caso di *shape morphing*: la flessione di una piastra vincolata al bordo d'uscita. Essa è indotta dall'applicazione di attuatori di tipo MFC - *Micro Fiber Composites* - sulla superficie: la forza generata dall'applicazione di una tensione agli elettrodi dell'attuatore MFC induce a sua volta un momento flettente, essendo tale forza eccentrica rispetto all'asse neutro.
L'efficacia del sistema è stimata in termini di $C_{L,F}$, definito come la derivata del coefficiente di portanza rispetto alla forza generata dall'attuatore,

$$C_{L,F} \overset{\text{def}}{=} \frac{\partial C_L}{\partial F} \, . \tag{5.3}$$

Nel capitolo 2 sono stati definiti alcuni modelli adottabili per descrivere il comportamento strutturale del sistema, e si è descritto il funzionamento del solutore aerodinamico scelto, XFoil; i modelli strutturali sono stati sviluppati a partire dall'equilibrio alla rotazione di una trave di Eulero-Bernoulli per grandi rotazioni e piccole deformazioni. Questi risultati non lineari sono stati messi a confronto con quelli lineari, in modo da indagare il campo di applicabilità di quest'ultimi. I risultati mostrano che l'errore del modello lineare risulta molto basso nel campo di applicazione analizzato. La figura 5.1 mostra un esempio di risultati in termini di variazione del C_L al variare della forza applicata, per piastre, che nel modello 2D vengono modellate come travi, di diversa lunghezza.

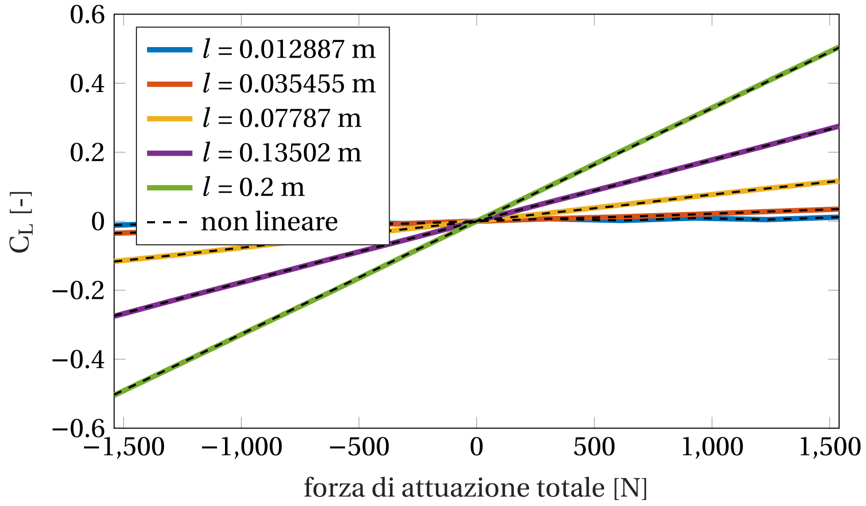

Figura 5.1: Variazione del C_L in funzione della forza di attuazione applicata, per diverse lunghezze della piastra.

Un'analisi parametrica del comportamento dell'attuatore a spostamento imposto, ovvero trascurando l'interazione aeroelastica tra forze di attuazione e forze aerodinamiche, ha mostrato un comportamento, per una modellazione inviscida dell'aerodinamica, descrivibile algebricamente come

$$C_{L,F}(\alpha, l, t, E) \approx e^{K+(K_t+K_{Et}E)t} l^{K_l} \cos\alpha\,, \tag{5.4}$$

dove l è la lunghezza della trave, t è il suo spessore, E è il suo modulo di Young, e α è l'angolo di attacco del profilo. Le costanti K, K_t, K_{Et}, e K_l sono stimate tramite una regressione.
Un'analisi Monte Carlo di questo modello rivela un errore medio di -0.0051, con deviazione standard di 0.0112, dove il primo termine è sintomo di un leggero bias nella stima dei coefficienti. L'errore complessivo è molto basso, soprattutto se si considera che è ottenuto mediante un modello puramente algebrico.

L'analisi viscosa (utilizzando le correzioni di strato limite di XFoil) rivela dei comportamenti più complessi. La viscosità ha tre effetti fondamentali sull'attuazione:

1. quando lo strato limite è turbolento il $C_{L,F}$ descresce linearmente con lo spessore di spostamento medio calcolato sull'attuatore (figura 5.2):

   $$C_{L,F}(\alpha,\ldots) = \left(K_{\mathrm{Re}}(\mathrm{Re}) - \delta^*(\alpha,\ldots)\right) C_{L,F}^{\mathrm{inv}}\,. \tag{5.5}$$

   Lo stesso comportamento del $C_{L,F}$ non si osserva quando lo strato limite è laminare, nel qual caso non è stato identificato un modello semplice;

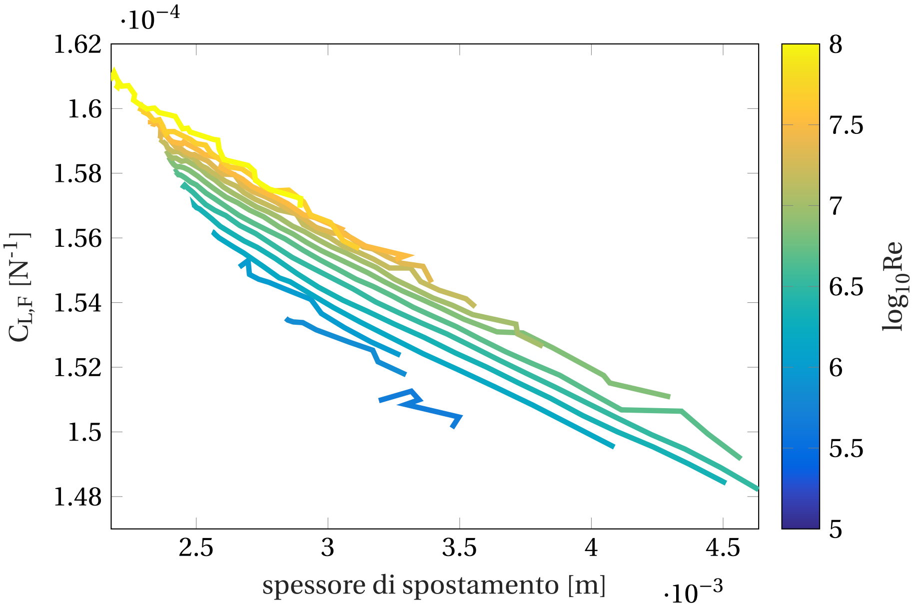

Figura 5.2: $C_{L,F}$ in funzione dello spessore di spostamento medio sull'attuatore, per uno strato limite turbolento, per diversi numeri di Reynolds.

2. vi è un effetto di accorciamento apparente dell'attuatore al variare del numero di Reynolds (figura 5.3), e questo effetto cresce linearmente con lo spessore di spostamento medio sull'attuatore

   $$l_{\mathrm{eff}} = l - l_s(l, \mathrm{Re})\,; \tag{5.6}$$

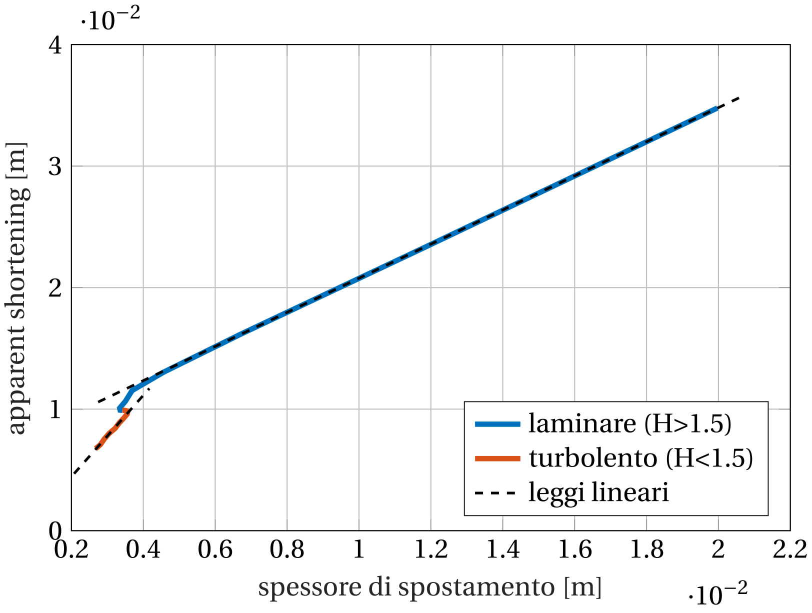

Figura 5.3: Accorciamento apparente dell'attuatore a causa della viscosità, in funzione dello spessore di spostamento medio. Si noti il cambio di pendenza in corrispondenza con la transizione dello strato limite.

la pendenza delle rette in (l_s, δ^*) cambia bruscamente con la transizione;

3. alti fattori di forma fanno calare sensibilmente il $C_{L,F}$ (figura 5.4).

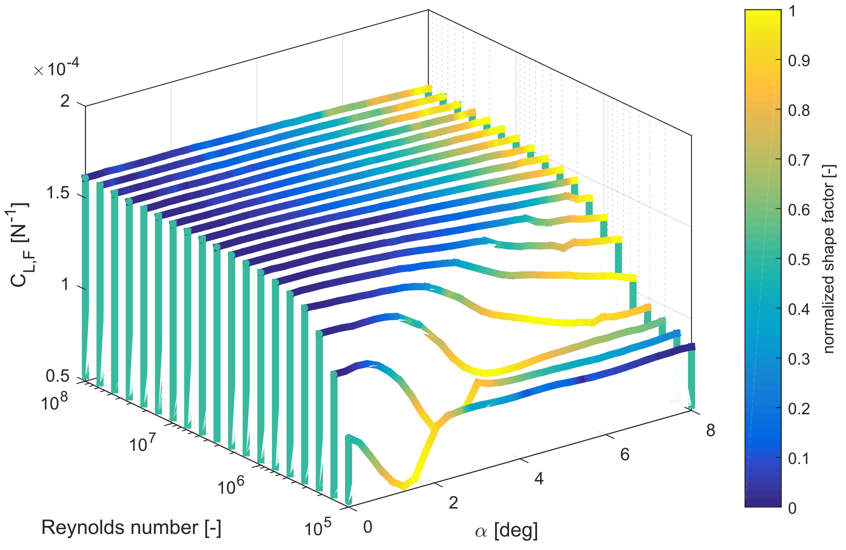

Figura 5.4: Variazione del $C_{L,F}$ in funzione del numero di Reynolds e dell'angolo di attacco. Il fattore di forma dello strato limite è mostrato mediante la mappa di colore.

È possibile analizzare l'interazione fra le forze aerodinamiche e la deformabilità della struttura. Tali effetti sono mostrati nella figura 5.5.

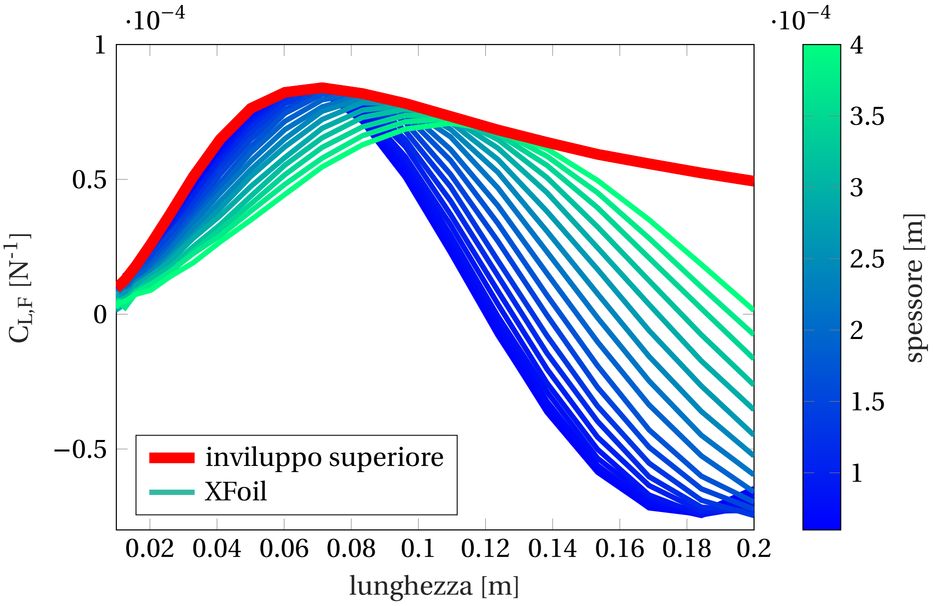

Figura 5.5: $C_{L,F}$ in funzione della lunghezza dell'attuatore, al variare dello spessore, tenendo conto dell'accoppiamento aeroelastico.

Si può notare come il $C_{L,F}$ presenti un massimo, e con un attuatore sufficientemente lungo possa manifestarsi un suo cambio di segno, ovvero un'inversione dei comandi. Si può però anche notare come l'inviluppo dei $C_{L,F}$ corrispondenti a spessori diversi abbia un rateo di decrescita molto inferiore a quello delle curve a spessori imposti, e presenti anch'esso un massimo. Questo significa che, fissata una velocità, esiste una combinazione ottima di lunghezza e spessore.
Un'analisi di questi inviluppi al variare della velocità di volo ha mostrato come l'effetto di accoppiamento fluido-struttura si possa modellare alla stregua di un'efficienza con la seguente forma:

$$\tilde{\mathcal{E}}_c(l,V) = \begin{cases} Q\,V^{Q_V}\,l^{Q_l} & l > (1+P)\,l_c(V)\,, \\ \dfrac{1}{1+G\,V^{G_V}\,l^{G_l}} & l < (1+P)\,l_c(V)\,, \end{cases} \tag{5.7}$$

dove l è la lunghezza della piastra attuante, e $(1+P)l_c(V)$ una funzione della velocità del fluido che definisce il passaggio tra diversi regimi della $\tilde{\mathcal{E}}_c(l,V)$. Ciò significa che l'accoppiamento si manifesta con piastre sufficientemente corte come un polinomio fratto, mentre al crescere della lunghezza diventa una legge di potenza.

Le simulazioni effettuate utilizzando valori realistici dei parametri hanno mostrato buone potenzialità di questa tecnologia in una vasta gamma di applicazioni, che va dai piccoli velivoli di aviazione generale, fino ai velivoli da trasporto regionale come l'ATR 42. Anche l'applicazione a UAV sembra essere potenzialmente interessante [5].

Nel quarto capitolo di questo lavoro è stata svolta una preliminare verifica sperimentale. È stato costruito un sistema di attuazione in fibra di carbonio unidirezionale al fine di ottenere una cedevolezza molto maggiore in corda rispetto a quella in apertura. Un attuatore di esempio è mostrato in figura 5.6.

Figura 5.6: Piastra di carbonio con MFC incollati su un lato, prima di essere montata sul bordo di uscita di un profilo.

Le campagne sperimentali hanno rivelato un buon accordo con le previsioni numeriche, a patto di introdurre due parametri liberi difficilmente misurabili, e di identificarli correttamente tramite i dati sperimentali. Il primo parametro è la rigidezza di una molla apparente posizionata tra la piastra di attuazione e il profilo, il secondo consiste in un'efficienza di attuazione compresa tra 0 ed 1, causata dall'incollaggio degli MFC alla piastra. Un esempio di confronto fra dati sperimentali e risultati numerici è mostrato in figura 5.7, con i parametri liberi indicati nella legenda.

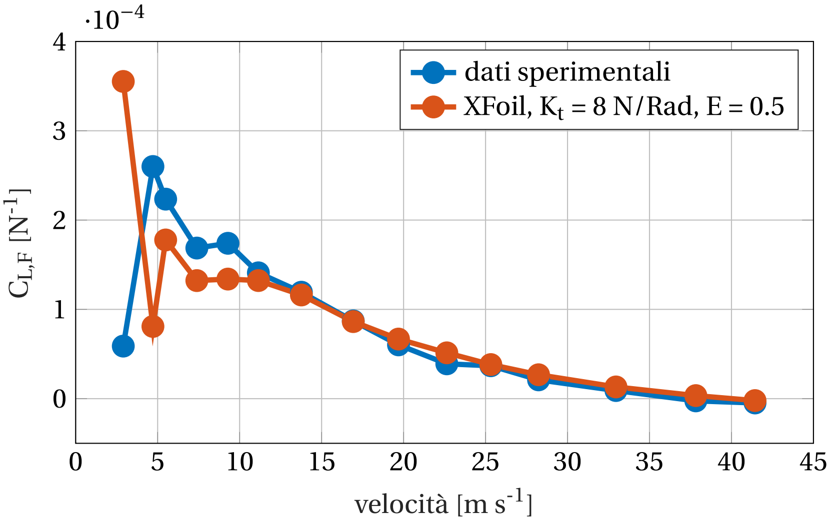

Figura 5.7: Confronto tra il $C_{L,F}$ misurato in galleria del vento e quello predetto numericamente al variare della velocità, per un angolo di attacco di 3°.

Alla luce delle prestazioni promettenti e dei modelli analitici ottenuti, diversi sviluppi futuri sono auspicabili. Innanzitutto è possibile effettuare studi di ottimizzazione della configurazione strutturale allo scopo di dimensionare sistemi di attuazione per applicazioni reali. È anche possibile modellare i fenomeni instazionari, specialmente in vista delle alte frequenze d'attuazione che sono in grado di raggiungere gli MFC, sia nel controllo delle vibrazioni intrinseche degli attuatori osservate ad elevati angoli di incidenza sia nel controllo delle strutture coerenti che vengono rilasciate al bordo d'uscita al fine di ridurre la resistenza e il rumore generato. Ciò richiederebbe un cambio di solutore aerodinamico, in quanto con XFoil non risulta possibile tenere in conto gli effetti instazionari.

Bibliography

[1] J.D. Anderson. *Fundamentals of Aerodynamics*. Aeronautical and Aerospace Engineering Series. McGraw-Hill, 2001. ISBN: 9780072373356.

[2] Chuen-Yen Chow Arnold M. Kuethe. *Foundations of Aerodynamics: Bases of Aerodynamic Design (5th Ed.)* 5th Edition. John Wiley and Sons, Inc., 1998. ISBN: 0471129194,9780471129196.

[3] *ATR FAMILY*. ATR DC/E. 1, allée Pierre Nadot, 31712 Blagnac cedex, France, 2014.

[4] B. Berton. "Shape memory alloys application: trailing edge shape control". In: *NATO OTAN RTO-MP-AVT-141* (2006).

[5] O. Bilgen et al. "A novel unmanned aircraft with solid-state control surfaces: Analysis and flight demonstration". In: cited By 0. 2011. DOI: `10.2514/6.2011-2071`.

[6] D.J. Cleaver et al. "Thrust enhancement due to flexible trailing-edge of plunging foils". In: *Journal of Fluids and Structures* 51 (2014). cited By 3, pp. 401–412. DOI: `10.1016/j.jfluidstructs.2014.09.006`.

[7] F. Côté et al. "Dynamic and static modelling of piezoelectric composite structures using a thermal analogy with MSC/NASTRAN". In: *Composite Structures* 65.3-4 (2004). cited By 49, pp. 471–484. DOI: `10.1016/j.compstruct.2003.12.008`.

[8] Drela, M. and Youngren, H. *AVL*. Version 3.35.

[9] Drela, M. and Youngren, H. *XFoil*. Version 6.99.

[10] Mark Drela. "XFOIL: An analysis and design system for low Reynolds number airfoils". In: *Low Reynolds number aerodynamics*. Springer, 1989, pp. 1–12.

[11] D. Dwarakanathan et al. "Design, development and ground testing of hingeless elevons for MAV using piezoelectric composite actuators". English. In: *ADVANCES IN AIRCRAFT AND SPACECRAFT SCIENCE* 2.3 (JUL 2015), 303–328. ISSN: 2287-528X. DOI: `{10.12989/aas.2015.2.3.303}`.

[12] *First Steps towards Piezoaction*. Piezomechanik GmbH. Berg am Laim Str. 64 D-81673 Munich, 2016.

[13] H. Flanders. "Differentiation under the integral sign". In: *Mathematical Association of America* 80.6 (1973), pp. 615–627. DOI: `10.2307/2319163`.

[14] DN Foster, PR Ashill, and BR Williams. "The nature, development and effect of the viscous flow around an aerofoil with high-lift devices". In: *Aerodynomrcs Dept., R. A E, Farnborough* (1974).

[15] S. Heathcote, Z. Wang, and I. Gursul. "Effect of spanwise flexibility on flapping wing propulsion". In: *Journal of Fluids and Structures* 24.2 (2008). cited By 194, pp. 183–199. DOI: `10.1016/j.jfluidstructs.2007.08.003`.

[16] J.S. Herrington et al. "Development of a twisting wing powered by a shape memory alloy actuator". In: cited By 0. 2015.

[17] J. E. Huber, N. A. Fleck, and M. F. Ashby. “The selection of mechanical actuators based on performance indices”. In: *Proceedings of the Royal Society of London A: Mathematical, Physical and Engineering Sciences* 453.1965 (1997), pp. 2185–2205. ISSN: 1364-5021. DOI: `10.1098/rspa.1997.0117`.

[18] Allen Plotkin Joseph Katz. *Low-Speed Aerodynamics: From Wing Theory to Panel Methods*. MGH. Mcgraw-Hill Series in Aeronautical and Aerospace Engineering. McGraw-Hill Companies, 1991. ISBN: 0070504466,9780070504462.

[19] David Lednicer. *The Incomplete Guide to Airfoil Usage*. 2010. URL: `http://m-selig.ae.illinois.edu/ads/aircraft.html` (visited on 09/10/2017).

[20] Y. Liu et al. “Shape memory polymers and their composites in aerospace applications: A review”. In: *Smart Materials and Structures* 23.2 (2014). cited By 0. DOI: `10.1088/0964-1726/23/2/023001`.

[21] *Macro Fiber Composite - MFC*. Smart Material Corp. 2170 Main Street, Suite 302, FL 34237, U.S.A., 2016.

[22] P.M. Magalhães da Costa Aleixo. “Morphing Aircraft Structures, Design and Testing an Experimental UAV”. MA thesis. Universidade Técnica de Lisboa, 2007.

[23] D.A. Neal et al. “Design and wind-tunnel analysis of a fully adaptive aircraft configuration”. In: vol. 3. cited By 0. 2004, pp. 2387–2395.

[24] O.J. Ohanian et al. “Piezoelectric morphing versus servo-actuated MAV control surfaces”. In: cited By 11. 2012.

[25] D.A. Perkins, J.L. Reed Jr., and E. Havens. “Adaptive wing structures”. In: vol. 5388. cited By 11. 2004, pp. 225–233. DOI: `10.1117/12.541650`.

[26] *Piper Cheerokee Warrior II Pilot’s Operating Handbook*. Approved by Ward Evans. Piper. 1982.

[27] Associate Prof. Huarong Zeng (auth.) Prof. Qingrui Yin Prof. Binghe Zhu. *Microstructure, Property and Processing of Functional Ceramics*. Jointly published with Metallurgical Industry Press2010. Springer Berlin Heidelberg, 2010. ISBN: 978-3-642-01693-6,978-3-642-01694-3.

[28] L. Quartapelle and F. Auteri. *Fluidodinamica Comprimibile*. CEA, 2013. ISBN: 9788808185587.

[29] J. N. Reddy. *An Introduction to Nonlinear Finite Element Analysis*. Oxford Scholarship Online, 2004. ISBN: 9780198525295.

[30] Sala, G. and Di Landro, L. A. *Tecnologie e Materiali Aerospaziali*. 2016.

[31] Johannes Scheller et al. “A combined smart-materials approach for next-generation airfoils”. In: *Solid State Phenomena* 251 (2016), pp. 106–112.

[32] Johannes Scheller et al. “Experimental Investigation of a Hybrid Morphing NACA4412 Airfoil Via Time-Resolved PIV Measurements”. In: *Advances in Fluid-Structure Interaction*. Springer, 2016, pp. 45–57.

[33] Hermann Schlichting. *Boundary-layer theory*. 7th ed. McGraw-Hill series in mechanical engineering. McGraw-Hill, 1979. ISBN: 9780070553347,0070553343.

[34] A.Y.N. Sofla et al. “Shape morphing of aircraft wing: Status and challenges”. In: *Materials and Design* 31.3 (2010). cited By 125, pp. 1284–1292. DOI: `10.1016/j.matdes.2009.09.011`.

[35] S.A. Solovitz and J.K. Eaton. “Experimental aerodynamics of mesoscale trailing-edge actuators”. In: *AIAA Journal* 40.12 (2002). cited By 5, pp. 2538–2540.

[36] D.P. Wang et al. “Development of high-rate, large deflection, hingeless trailing edge control surface for the Smart Wing wind tunnel model”. In: vol. 4332. cited By 15. 2001, pp. 407–418. DOI: `10.1117/12.429682`.

[37] B.K.S. Woods, C.S. Kothera, and N.M. Wereley. “Wind tunnel testing of a helicopter rotor trailing edge flap actuated via Pneumatic Artificial Muscles”. In: *Journal of Intelligent Material Systems and Structures* 22.13 (2011). cited By 24, pp. 1513–1528. DOI: `10.1177/1045389X11424216`.

[38] Y. Yu et al. “Investigation on adaptive wing structure based on shape memory polymer composite hinge”. In: vol. 6423. cited By 5. 2007. DOI: `10.1117/12.779394`.